AN ATOMIC BEAM POLARIZED $^3He^+$ ION SOURCE

by

ROBERT NORMAN VYSE

B.A.Sc., University of British Columbia, 1965

M.A.Sc., University of British Columbia, 1967

A THESIS SUBMITTED IN PARTIAL FULFILMENT OF

THE REQUIREMENTS FOR THE DEGREE OF

DOCTOR OF PHILOSOPHY

in the Department

of

Physics

We accept this thesis as conforming to the

required standard

THE UNIVERSITY OF BRITISH COLUMBIA

January, 1970

In presenting this thesis in partial fulfilment of the requirements for an advanced degree at the University of British Columbia, I agree that the Library shall make it freely available for reference and study. I further agree tha permission for extensive copying of this thesis for scholarly purposes may be granted by the Head of my Department or by his representatives. It is understood that copying or publication of this thesis for financial gain shall not be allowed without my written permission.

Department of Physics

The University of British Columbia
Vancouver 8, Canada

Date Jan 8/70

ABSTRACT

AN ATOMIC BEAM POLARIZED $^3He^+$ ION SOURCE

A beam of polarized $^3He^+$ ions has been produced using atomic beam method techniques. This method has the attraction of being capable of producing an ion beam with polarizations up to 100%. The polarization of ^3He beams presently produced by optical pumping techniques is of the order of 5%. The apparatus is composed of three main sections: the atomic beam source consisting of a supersonic nozzle cooled to liquid helium temperatures to produce a low velocity atomic beam, the tapered hexapole magnet to spatially separate the particles in the two magnetic spin substates, and the electron bombardment ionizer to produce $^3He^+$ ions from the neutral ^3He atomic beam. The low velocity beam is required because the nuclear magnetic moment of ^3He is of the order of $_{1000}$ times smaller than the electronic magnetic moment used to separate beams in conventional Stern-Gerlach magnets and to achieve a high ionization efficiency. The measured intensity of the beam produced by the atomic beam source cooled to liquid helium temperature was 1×10^{18} atoms/sr-sec, the most probable velocity was 310 m/sec, and the velocity full width at half maximum was 50 m/sec. The beam flux through the ionizer increases by a factor of 1.3 when the hexapole field is turned on, in good agreement with the theoretically expected increase.

This increase corresponds to a polarization of 65% of the atomic beam. A 12nA $^3He^+$ ion beam was obtained corresponding to an ionization efficiency of approximately 0.15%.

TABLE OF CONTENTS

			Page
CHAPTER I	-	INTRODUCTION.....	1
CHAPTER II	-	METHODS FOR PRODUCING POLARIZED ^3He BEAMS.....	7
	A.	The Optical Pumping Method.....	7
	B.	The Atomic Beam Method.....	9
CHAPTER III	-	PRODUCTION OF MOLECULAR BEAMS.....	13
	A.	Motivation for Development of Molecular Beams.....	13
	B.	Properties of the Molecular Flow Beam.....	14
	C.	Properties of the Nozzle Beam.....	15
		(1) Gas Flow Through the Nozzle.....	17
		(2) The Free Jet Expansion.....	18
		(3) The Freezing Surface.....	23
		(4) Velocity Distribution of Particles in the Beam.....	26
		(5) Intensity Available from Nozzle Beams.....	30
		(i) Freely Expanding Jet Intensity..	30
		(ii) Beam Intensity Downstream from the Skimmer.....	30
		(6) Deviations from Ideal Behaviour.....	31
		(7) Low Temperature Nozzle Sources and their Uses.....	33
CHAPTER IV	-	THE POLARIZED $^3He^+$ BEAM SOURCE.....	37
	A.	The Low Temperature Atomic Beam Source....	37
		(1) General Description.....	37

Page

(2) Thermal Transpiration Corrections to Pressure Measurements..... 42

(3) Carbon Resistor Temperature Measurements..... 45

B. The Hexapole Magnet..... 49

C. The Electron Bombardment Ionizer..... 52

CHAPTER V - TECHNIQUES FOR MEASUREMENT OF ATOMIC BEAM INTENSITY AND VELOCITY..... 58

A. Measurement of the Atomic Beam Intensity.. 58

B. The Time-of-Flight Measuring Apparatus.... 59

CHAPTER VI - RESULTS OF STUDIES OF THE ATOMIC BEAM..... 66

A. The Atomic Beam Intensity..... 66

B. The Atomic Beam Velocity..... 82

CHAPTER VII - POLARIZATION AND IONIZATION OF THE ^3He BEAM..... 88

A. The Trajectories of Atoms through the Hexapole Magnet..... 88

B. The Calculated Polarization of the Atomic Beam..... 90

C. The Polarization Measurement and Ion Beam Yield..... 95

CHAPTER VIII - CONCLUSIONS..... 99

A. Comparison with Other Sources of Polarized $^3He^+$ Ions..... 99

B. Measurement of the $^3He^+$ Beam by the $D(^3He,P)^4He$ Reaction..... 101

C. Possible Improvements of the Polarized $^3He^+$ Beam Apparatus..... 104

Page

(1) Improvements Increasing the Atomic Beam Intensity..... 104

(2) Improvements Reducing the Atomic Beam Velocity..... 105

(3) Improvements in Ionization Efficiency and Extraction..... 106

(4) Overall System Improvement Possibilities by Changing Geometry... 107

(5) Improvements in Vacuum System Reducing Background Ion Yield..... 109

Page

APPENDIX A. - INTENSITY FROM A FREELY EXPANDING JET..... 111

APPENDIX B. - INTENSITY AND VELOCITY DISTRIBUTION OF PARTICLES IN THE JET AFTER PASSING THROUGH A SKIMMING ORIFICE..... 113

APPENDIX C. - TRAJECTORIES OF PARTICLES PASSING THROUGH A HEXAPOLE MAGNET..... 120

1. Equation of Motion of a Magnetic Dipole in a Axially Symmetric Multipole Field.... 120

2. Trajectories of a Magnetic Dipole in a Parallel Hexapole Magnet..... 124

3. Trajectories of a Magnetic Dipole in a Tapered Hexapole Magnet..... 126

APPENDIX D. - CALCULATION OF THE SIGNAL SHAPE FROM THE TIME-OF-FLIGHT APPARATUS..... 132

APPENDIX E. - A LOW TEMPERATURE NOZZLE BEAM FOR A POLARIZED $^3He^+$ ION SOURCE by R. Vyse, J.C. Heggie and M.K. Craddock reprinted from 6th Int'l Symposium on Rarefied Gas Dynamics, 2, Academic Press Inc. New York (1969)..... 138

APPENDIX F. - LOW TEMPERATURE ATOMIC ^3He BEAM FOR USE IN A POLARIZED $^3He^+$ ION SOURCE by R. Vyse, D. Axen and M.K. Craddock Rev. Sci. Instr. In press..... 143

BIBLIOGRAPHY 144

LIST OF FIGURES

		Page
1.	Energy Levels of ^{3}He Atoms in an External Magnetic Field (not to scale).....	8
2.	General Arrangement of the Components of the Polarized ^{3}He Apparatus showing the differential pumping required to handle the ^{3}He gas flow.....	10
3.	Nuclear Polarization of Singly Ionized ^{3}He Atoms for Equal Fields in the Ionizing and Target Regions.....	12
4.	Schematic Representation of Nozzle Beam Source.....	16
5.	Discharge Coefficient vs. Reynolds Number based on Experimental Flow and Viscosity at Stagnation Conditions.....	19
6.	Schematic Representation of Flow from an Orifice into an Evacuated Region.....	20
7.	Distribution of Mach Number Along the Axis of Symmetry of the Expanding Jet.....	21
8.	Terminal Mach Numbers as a Function of Inverse Knudsen Number based on Stagnation Conditions at the Nozzle.....	25
9.	Schematic Representation of Radially Expanding Flow through a Skimmer to a Detector.....	27
10.	The Low Temperature ^{3}He Atomic Beam Source...	38
11.	The Adjustable Nozzle-Skimmer Assembly.....	43
12.	Conditions for Thermal Transpiration Effect..	44
13.	Thermal Transpiration Corrections to Measurements of Nozzle-Skimmer and Skimmer-Collimator Pressure.....	46
14.	A.C. Bridge Used to Monitor Resistance of Carbon Resistor Thermometer.....	49

		Page
15.	Input Power Induced Heating of Carbon Resistor Thermometer with Resistor at Near Liquid Temperature.....	47
16.	Calibration of Carbon Resistor Thermometer...	48
17.	Dimensions of the Components of the Hexapole Magnet.....	50
18.	Magnetic Field Strength in the Region of the Pole Tips as a Function of the Electrical Current Through the Coils.....	51
19.	Measured Value of the Magnetic Field Strength as a Function of the Radial Distance from Central Axis.....	53
20.	Schematic Representation of Ionizer and Ion Measurement Apparatus (A) D.C. Current Measurement (B) Chopped Current Measurement.....	54
21.	Two Slit Chopper.....	54
22.	Ionizer Ion Yield as a Function of Background Hydrogen Gas Pressure.....	56
23.	Schematic Representation of Time-of-Flight Velocity Measurement Equipment.....	60
24.	Phototransistor Reference Signal Circuit.....	60
25.	Schematic of Ion Gauge Signal Circuit, Reference Signal and Oscilliscope Display....	61
26.	Broadening of Experimental Signal due to Finite Width Shutter Function. Nozzle Beam Curve Includes Correction for a 2.5 cm Detector Length.....	62
27.	Assumed Intensity Profile of Particles Passing through the Chopper Opening (Shutter Function). Tangential Chopper Velocity = 35 m/sec.....	64
28.	Room Temperature Beam Intensity Profiles for a 0.2 cm Diameter Nozzle.....	67
29.	Room Temperature Beam Intensity Profiles as a Function of Nozzle-Skimmer Separation.....	68

Page

30. Continuous Beam Profile Taken with Adjustable Nozzle-Skimmer Assembly..... 70

31. Beam Intensity Profiles for a 0.2 cm Diameter Nozzle Operated at 77°K..... 72

32. Liquid Nitrogen Temperature Beam Intensity Profiles as a Function of Nozzle-Skimmer Separation..... 73

33. Beam Intensity Profiles as a Function of Nozzle-Skimmer Separation with the Nozzle at Liquid Helium Temperature..... 75

34. Beam Intensity Profiles for 0.2 cm Diameter Nozzle Operated at Liquid Helium Temperature. 76

35. ^{4}He Beam Intensities as a Function of Nozzle Stagnation Pressure Po for Three Temperatures To. The dashed lines passing through the origin are fits to the data after correction for scattering..... 78

36. Beam Intensities for ^{3}He and ^{4}He Beams at Liquid Helium Temperature Before and After Correction for Scattering. Only the uncorrected experimental points are shown when the correction is small..... 79

37. The Uncorrected Data of Fig. 36 Divided by the Nozzle Pressure to Verify Existance of Scattering..... 80

38. Normalized Intensity Profile vs. Vertical Displacement from Beam Axis.
Stagnation Pressure Po = 420 Torr
Stagnation Temperature To = 77°K..... 83

39. Typical ^{3}He Time-of-Flight Spectrum for Liquid Helium Cooled Nozzle. Stagnation Pressure is 36 Torr. Horizontal Time Scale is 0.5 m sec/div. The Upper Trace shows the Time Reference Light Pulse..... 85

40. Results of Fig. 39 Converted into a Velocity Spectrum. The curve shown is a fit of Eq. 17 to the experimental spectrum..... 86

Page

41. Typical Trajectories of Focussed and Defocussed ^{3}He Atoms passing through the Hexapole Magnet. The Source-Magnet Separation is 15 cm and the Field at the Magnet Pole Tips is taken as 9000 Gauss..... 91

42. Effect of Source-Magnet Separation on Intensity and Polarization of Atomic Beam. Nozzle at 4.2°K..... 93

43. Effect of Source-Magnet Separation on Intensity and Polarization of Atomic Beam. Nozzle at 7°K..... 94

44. Schematic Diagram Indicating Relative Location of Components Used in Atomic Beam Polarization Measurement. Dimensions in cm.. 95

45. Change in Differential Pirani Detector Signal when Hexapole Magnet is Turned On and Off..... 97

46. Typical Ionizer Signals from Chopped Atomic Beam with Hexapole Magnet Turned On and Off. Horizontal Scale 0.5 ms/div. Vertical Scale 0.5 mv/div..... 85

47. Enhancement Ratio of Ionized Beam as a Function of Magnet Excitation Current..... 98

48. Defining Diagram for Calculation of Flow through Nozzle-Skimmer System..... 114

49. Definition of Certain Variables used in Calculation of Flow through Nozzle-Skimmer System..... 115

50. Schematic Diagram Showing Two Poles of a Radially Symmetric Magnet..... 121

51. Schematic Diagram Showing the Parameters used to describe the Tapered Hexapole Magnet. 127

52. Rectangular Chopper Shutter Function..... 133

53. Rectangular Detector Response Function..... 133

54. Geometry of Time-of-Flight Apparatus..... 133

LIST OF TABLES

Page

1. Detailed Summary of Heat Leaks into the Cryostat of the Low Temperature Atomic Beam Source. Measurements were made after initial construction of source and after extensive modifications necessary to reduce heat leak to the expected design values..... 39

2. Selected Trajectories of Focussed and Defocussed ^3He Atoms Passing Through the Tapered Hexapole Magnet..... 89

3. Comparison of different Methods of Producing Polarized $^3He^+$ Ions..... 100

ACKNOWLEDGEMENTS

I would like to thank my supervisor, Dr. M.K. Craddock, for his continued interest throughout the course of the work described in this thesis.

I would also express my thanks to Dr. D. Axen, who originally built much of the existing polarized helium-3 beam apparatus, for his continuous interest and untiring help with many of the experimental measurements described in this thesis.

I would also thank Drs. White, Erdman and Warren for their interest and encouragement during the course of this work.

I am extremely greatful to the many technicians who have contributed to this work over a period of many years; in particular, Messrs. D. Haines, C. Sedger and D. Stonebridge for their useful suggestions and excellent craftmanship.

I wish to thank the National Research Council for one bursary and three scholarships held during the course of this work.

CHAPTER I

INTRODUCTION

The study of the nature of nuclear forces and the part they play in various reaction mechanisms has been a subject of considerable interest for many years. The spin dependent nature of these forces has been a subject of more recent interest. In essence the spin dependence of the nuclear force implies that the force between two interacting nucleons depends both on the magnitude and orientation of the spin vector characterizing the magnetic moment of the particles. Various expressions for this interaction have been postulated and are often represented in nuclear models by potentials; a common example is the spin-orbit potential $V_{so} \propto \underline{\sigma} \cdot \underline{\ell}$ where $\underline{\sigma}$ is the Pauli spin operator and $\underline{\ell}$ is the orbital angular momentum operator. From an experimentalist's point of view the study of the nature of these forces is only possible because of the availability of spin sensitive detectors, polarized targets or polarized beams.

The spin of a particle is measured relative to some reference axis, sometimes a magnetic field direction. For spin $\frac{1}{2}$ particles such as protons, and ^3He there are two nuclear magnetic spin substates $m_I = +\frac{1}{2}$ or $m_I = -\frac{1}{2}$ depending on whether the nuclear spin lines itself up parallel (spin up) or antiparallel (spin down) to the direction of the magnetic field axis. The polarization P of an ensemble of such particles is given by

$$P = \frac{N(+\frac{1}{2}) - N(-\frac{1}{2})}{N(+\frac{1}{2}) + N(-\frac{1}{2})}$$

where $N(+\frac{1}{2})$ is the fractional number of particles in the beam

or target with their spins aligned parallel to the magnetic field while $N(-\frac{1}{2})$ is the fractional number aligned antiparallel. A beam or target with equal populations of both substates is said to be unpolarized and has zero polarization while a beam or target with all spins oriented in the positive direction would have 100% polarization.

Certain techniques have been developed for the study of spin dependent forces. Because of the strength of the spin-orbit force the reaction products of any reaction involving particles with nonzero spin and angular momentum will be partially polarized. These polarized particles can be collimated into a beam for use in a subsequent reaction. Beams formed in this manner are referred to as secondary beams. (p,p) elastic scattering can be used to produce a beam of polarized protons while the $D(D,^3He)n$ reaction can be used to produce a polarized neutron beam. Unfortunately these secondary beams frequently have inadequate particle fluxes to be of use in many experiments which might be envisaged to study, for example, the spin dependence of a selected reaction mechanism. Certain reactions can also be used to analyze the polarization of desired particles. For example, the elastic scattering of polarized protons off carbon or helium results in a left-right asymetry about the incoming beam axis which can be related to the incoming proton polarization.

The production of more intense beams of polarized particles has become possible through the development of polarized ion sources. These devices prepare beams of polarized

particles for injection into accelerators. By injecting polarized particles into the accelerator much higher beam intensities can be produced than by scattering or reaction techniques. Polarized proton and deuteron ion sources, which allow the preparation of intense beams with polarizations of near 100% for the case of the protons, have been extensively developed and they are now available as commercial items.

After the proton and deuteron one of the next simplest particles that could effectively be used in polarization studies is ^{3}He, an atom with nuclear spin of $\frac{1}{2}$ and a zero electronic spin. Unpolarized ^{3}He has been used extensively as both a target and projectile in nuclear physics studies for many years. Many of the interesting possibilities for research using ^{3}He as a projectile were discussed by Bromley and Almqvist (Br60) in a lengthy review article in 1960. Since that time ^{3}He induced reactions have been widely studied. Because of the strong spin dependence of the nuclear force none of these studies can be considered complete until the detailed effects of spin have been carefully investigated. In an experiment with unpolarized beams and targets and with no observation of the polarization of the outgoing particles the detailed spin dependence of the reaction is lost due to the average over the magnetic quantum numbers of initial and sum over the final states. Knowing the polarization of some combination of incoming projectile, target nucleus, or the outgoing reaction products can result in much more specific information on the detailed behaviour of the spin dependent forces. For this reason many previously studied inelastic, stripping and pickup reactions may be suitable candidates for

renewed study. G. C. Phillips (Ph66) has recently reviewed existing nuclear reaction studies using polarized ^3He targets and beams. Studies at Rice University using a polarized ^3He target in the $^3He(d,p)^4He$ reaction (Ba65) have provided the first indication that optical model theories of stripping processes must include tensor forces. It is clear that further studies with polarized beams and targets need be carried out for other stripping reactions to further define their spin dependence.

Polarized nuclei can also be used to help make assignments of spins and parities of excited states of nuclear systems. Again the Rice group has used a polarized ^3He target in the study of the unstable nucleus ^4Li formed as an intermediate state in the $^3He(p,p)^3He$ reaction (Ba67). They have determined information about the spins and parities of $T = 1$ states of the mass 4 system. In this reaction it is basically impossible to deduce a unique set of phase shifts if only elastic scattering data with unpolarized beams and targets are available along with spin measurements of the scattered proton. However, if spins of the ^3He are also measured the degenerate solutions can be rejected and a unique determination of phase shifts becomes possible.

Polarized ^3He beams are also of interest because it is the neutron that is polarized; thus in a sense one has available a variable energy neutron beam for reactions involving the neutron eg. $(^3He,pp)$, and perhaps $(^3He,n)$.

Another interesting possibility for polarized ^3He as well as all other polarized particles is the testing of

conservation laws. The selection of crucial experiments to test parity and time reversal invariance in specific reactions should be greatly aided by the availibility of control over the polarization of the incoming beam. Selection of these crucial experiments may be aided by the systematic classification by Moravcsik, Csonka and Scadron (Mo66) of all experimental possibilities for reactions involving four nucleons of given spin.

To perform many of these potential experiments a polarized ^3He beam is required. To estimate the possible flux of polarized ^3He attainable as a secondary beam, consider the elastic scattering of ^3He off ^4He. Phillips and Miller (Ph59) show this scattering can result in near 100% polarization of the ^3He under certain conditions. For a ^3He bombarding laboratory energy of 5.2 Mev, the cross section for the production of 100% polarized ^3He scattered at 45° in the center of mass frame is 0.162 b/sr. If a 100 μA ^3He beam bombards a ^4He gas target 300 kev thick (5 atm pressure and 1.2 cm long) and if the solid angle of the resulting beam is restricted to 10^{-2} sr then the flux of the resulting scattered beam is 0.01 nA. It is unlikely all the above conditions could be achieved in practise thus 0.001 nA might be a more reasonable estimate of the possible polarized ^3He ion current. This intensity is too low to be of much use for many nuclear studies and thus we must turn to other techniques to produce more intense beams.

Two methods have been proposed for the production of polarized $^3He^+$ ion beams. An optical pumping technique has been successfully developed at Rice University. At U.B.C. an atomic

beam method for the production of polarized $^3He^+$ proposed by Warren, Axen and Klinger (Wa63) is under development. Initial design, construction and preliminary testing of the U.B.C. ion source has been reported by Axen (Ax65). The development of the ionizer has been reported by Vermette (Ve64) and the differential Pirani detector by Jassby (Ja64). The present thesis will discuss the detailed study of the atomic beam formation and its subsequent polarization and ionization.

The contents of this thesis is divided into the following chapters. In Chapter II a general description of the two techniques used to produce polarized $^3He^+$ ion beams is presented. In Chapter III the theoretical background of the low temperature nozzle source which is essential to the operation of the U.B.C. ion source is reviewed. Chapter IV gives a detailed description of the mechanical operation of U.B.C.'s ion source. Chapter V describes the techniques used to measure the intensity and velocity of the atomic beam. The results of these measurements are presented in Chapter VI. Chapter VII considers the effect the hexapole magnet has on the ^3He trajectories and the resulting beam polarization. Possible improvements to the polarized ion source are considered in Chapter VIII.

CHAPTER II

METHODS FOR PRODUCING POLARIZED $^3He^+$ BEAMS

A. The Optical Pumping Method.

The polarized $^3He^+$ ion source based on optical pumping techniques, succesfully developed at Rice University, delivers 4 μA of ions with a polarization measured by a nuclear double scattering experiment of 0.05 ± 0.01 (Ba68, Fi69). The emittance of the beam was estimated to be 1 cm·rad·$ev^{\frac{1}{2}}$.

The energy levels relevant to the optical pumping scheme are shown on Fig. 1. A weak self-sustaining electric discharge in very pure ^3He gas, produced by a 50 MH_zrf field around an optical pumping cell, excites some of the $^1S_0$ ground state ^3He atoms to the 2^3S_1 metastable state. Right-hand circularly polarized resonance light directed into the cell along the axis of the applied magnetic field produces $\Delta m_F = +1$ transitions from the lower ($m_F = -3/2, -\frac{1}{2}$)2^3S_1 hyperfine sublevels to the 2^3P_0 levels. Atoms in the 2^3P levels de-excite to the various 2^3S_1 levels with nearly equal probabilities. As this process is repeated over many cycles atoms are removed from the negative m_F hyperfine levels of the metastable atoms and are placed in the positive m_F levels, producing a polarization of the metastable atoms. The negative m_F levels can be populated in the same way using left-hand circularly polarized light; a polarization of the opposite sign results.

The polarization is transferred from the metastable atoms to the much more numerous 1^1S_0 ground state atoms by means

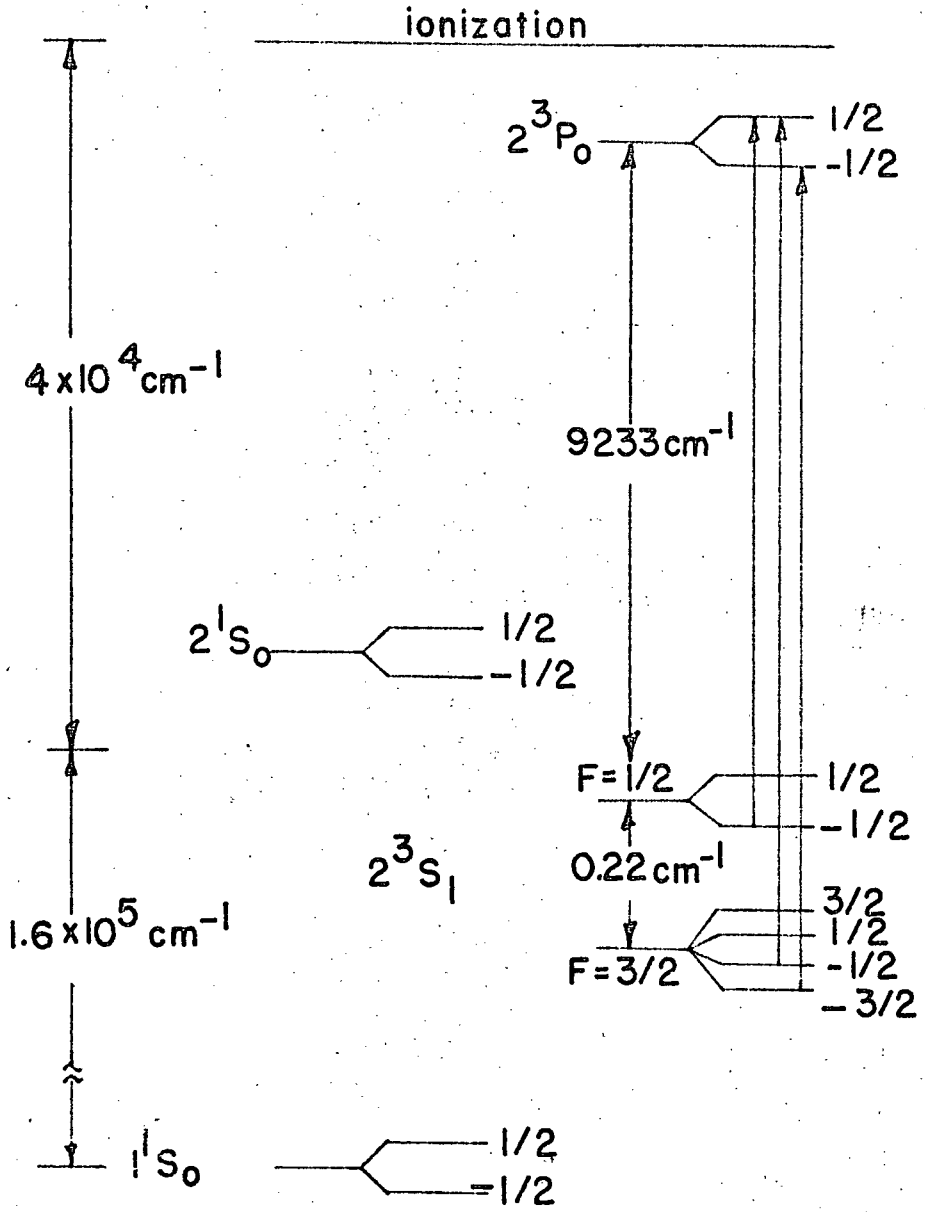

Fig. 1

Energy Levels of ^{3}He Atoms in an External Magnetic Field (not to scale).

of spin exchange collisions, and, under continuous illumination from the pumping light, the ground state polarization reaches an equilibrium value equal to that of the metastable atoms. The rf discharge produces both atoms in the metastable state as well as the ions. The ion polarization comes into equilibrium with the atomic ground state polarization because of a very large ($\sim 10^{-15}$ cm^2) cross section for electron exchange via He^+-He collisions. The ions are extracted from the optical pumping cell by standard rf ion source techniques.

The gas polarization in the optical pumping cell was measured to be 0.05 ± 0.01, which, within experimental error, is the measured value of the ion polarization. Thus it appears possible to extract an ion beam with the same polarization as the gas in the pumping cell. As polarizations of approximately 60% (Ga65) have been achieved in gas samples under optimum conditions, further improvements in the polarization of the ion beam can be expected. The present polarization appears to be limited by the short dwell time in the optical pumping cell. This may be overcome by increasing the dimensions of the pumping cell, hence allowing the ^{3}He atoms to remain under the influence of the pumping radiation for a longer time.

B. The Atomic Beam Method.

The particles in each of the two possible nuclear spin substates in an atomic beam of ^{3}He can be separated by passing the neutral beam through an inhomogeneous magnetic field. This technique was suggested by Warren, Axen and Klinger (Wa63)

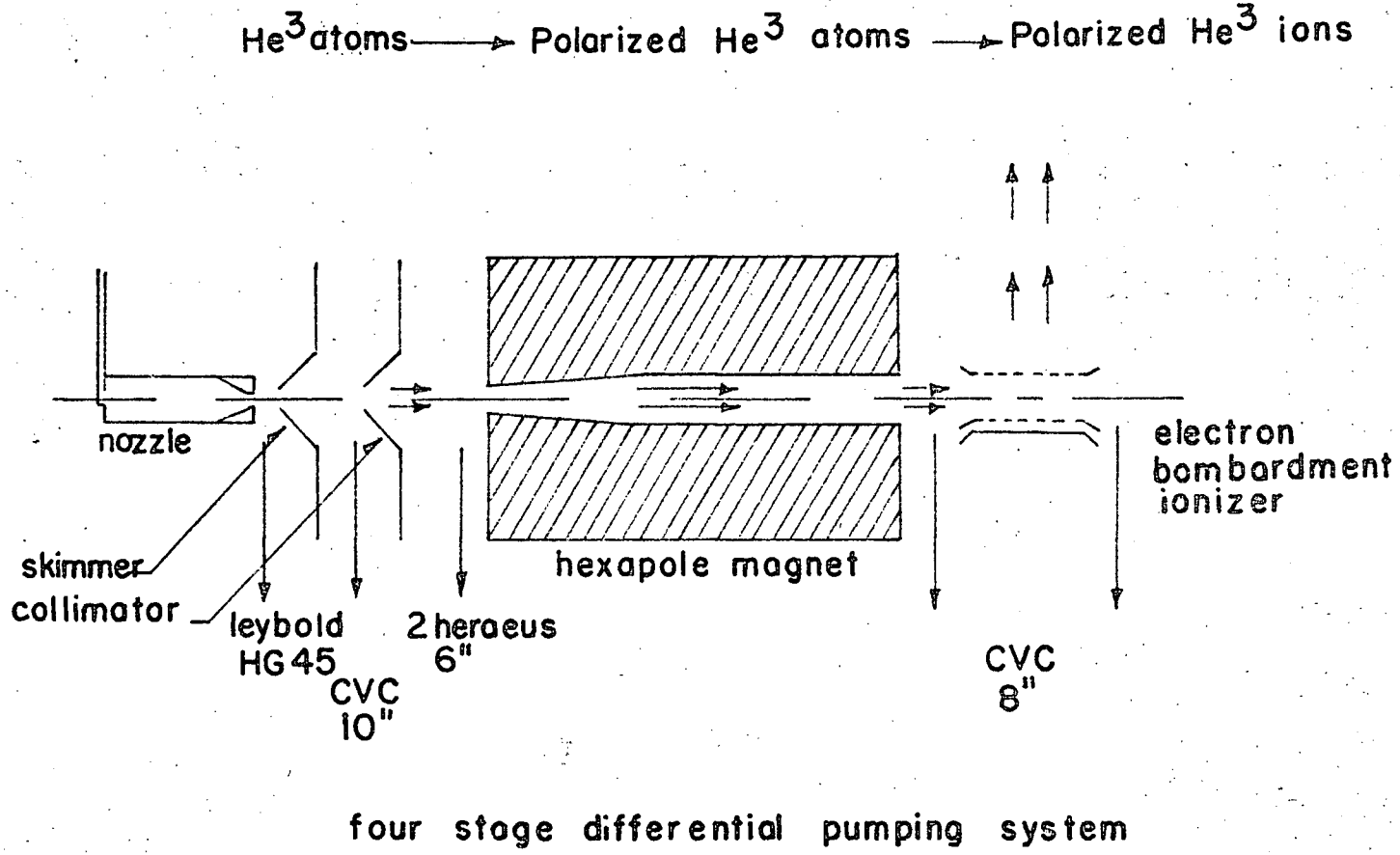

Fig. 2 General Arrangement of the Components of the Polarized ^3He Apparatus showing the differential pumping required to handle the ^3He gas flow.

as a method for producing a polarized $^3He^+$ ion beam. Fig. 2 shows a schematic view of this scheme. An atomic beam produced using a supersonic nozzle cooled to liquid helium temperatures is passed through the inhomogeneous magnetic field of a hexapole magnet. As atomic ^3He has no electronic magnetic moment, those particles with nuclear spin projection $+\frac{1}{2}$ in the direction of the applied field are deflected towards the magnet pole pieces and subsequently removed from the beam while those of nuclear spin projection $-\frac{1}{2}$ are deflected toward the central axis and focussed into the ionizer. The very small size of the ^3He nuclear moment and the need for a magnet of reasonable length producing conventional magnetic field strengths requires that the velocity of the particles entering the magnet be very low. In the original proposal an atomic beam with a most probable velocity of 180 m/sec was to pass through a tapered hexapole magnet 50 cm in length. Under these conditions it was calculated that an atomic beam could be prepared with near 100% polarization, that is, all the particles passing into the ionizer would be in the $-\frac{1}{2}$ nuclear spin projection state. Ionization of the beam would be achieved with an electron bombardment type ionizer. The positive ions so produced would be focussed and accelerated to produce a beam of polarized $^3He^+$ ions suitable for nuclear reaction studies. The percentage polarization of the ionized beam depends on the magnetic field strength present at the ionizer and the target. Axen (Ax65) has calculated the ^3He nuclear polarization expected of singly ionized ^3He atoms for equal fields in the ionizing and target

regions. His results are shown in Fig. 3.

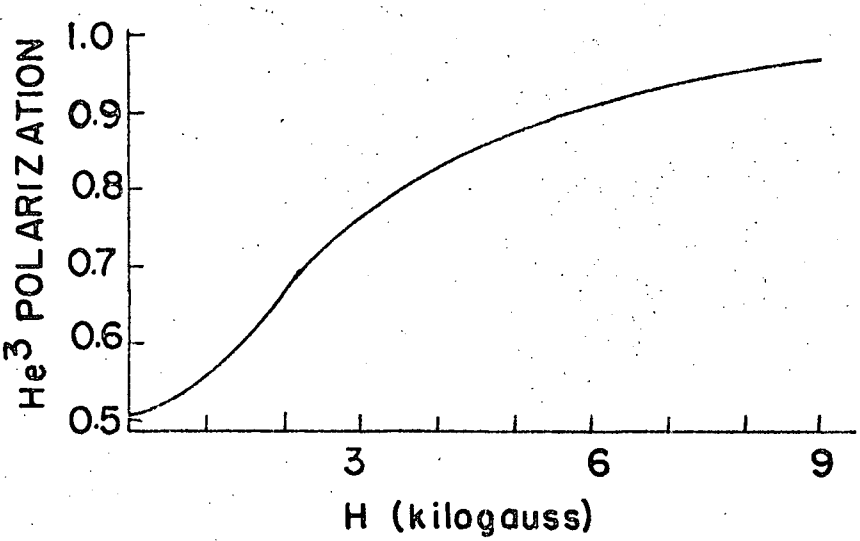

Fig. 3 Nuclear Polarization of Singly Ionized ^3He Atoms for Equal Fields in the Ionizing and Target Regions.

For zero field in the two regions a polarization of 50% is achieved and the polarization increases until it reaches almost 100% with a field of about 9 KG in both regions. Thus by ionizing and placing the target in a region of high but not technically excessive magnetic field it is possible to obtain a beam of near 100% nuclear polarization. It is this very high polarization which makes the atomic beam method of producing polarized $^3He^+$ ions so potentially attractive in nuclear physics experiments.

CHAPTER III

THE PRODUCTION OF MOLECULAR BEAMS

A. Motivation for Development of Molecular Beams.

Atomic beams have been instrumental in the advancement of many fields of physics. Early experiments verifying the Maxwellian velocity distribution helped establish the Kinetic theory of gases. The classic splitting of a silver beam into two beams as it passed through an inhomogeneous magnetic field was an early result explainable by spatial quantization, a result of quantum theory.

Molecular flow beams, beams where flow through the opening is collisionless, can be finely collimated but the intensity available is very low. For experiments requiring higher intensity Kantrowitz and Grey (Ka51) in 1951 proposed a system which hopefully would result in considerable improvements of beam intensities and velocity spread.

Their proposal employing a supersonic Laval nozzle appeared to provide a means of increasing beam intensities by at least one order of magnitude and to allow significant reductions in the velocity spread of the beam. Although originally proposed as a technique for the study of other physical phenomena, the nozzle beams rapidly became the subject of intense study. This study came about due to the failure of most prototype sources to perform in the predicted fashion. Subsequent investigations have revealed much of the true behaviour of these nozzle sources and now the expected

behaviour of a given nozzle system can be predicted with reasonable confidence. The discussion of theory and results to be presented will be directed towards a better understanding of the operation of the nozzle source used in the production of a polarized $^3He^+$ ion beam. The production of this polarized ion beam has been the main motivating force for the development work which has gone into the design of a low velocity atomic beam source. The last section in this chapter will summarize existing work on liquid helium cooled nozzle sources and discuss possible uses for low temperature nozzle sources.

B. Properties of the Molecular Flow Beam.

Before discussing the nozzle source the basic properties of the molecular flow beam i.e. a beam formed by free molecular flow through an orifice will be described. Molecular flow implies that the mean free path λ of the gas particles in the source is considerably larger than the diameter d and length of the orifice that is, the Knudsen number $Kn = \lambda/d$ is much greater than unity. The operation of a molecular flow beam has been discussed (Sm55, Ra56) but will be summarized below for completeness.

The rate N at which molecules pass through an aperture of area A is equal to the number of molecules hitting that area of the wall per second, and is given by

$$N = \tfrac{1}{4} n \bar{v} A \quad \text{molecules/sec} \qquad (1)$$

where n is the number of molecules per unit volume in the source and $\bar{v} = \sqrt{\frac{8kT}{\pi m}}$ is the average speed, k is Boltzman's constant,

T the oven temperature (^{o}K), and m the mass of the gas molecule. The intensity I at a distance r from the oven source is given by

$$I = \frac{1}{4} n \bar{v} A \frac{\cos\theta}{\pi r^2} \quad \text{molecules/cm}^2\text{-sec} \qquad (2)$$

where θ is the angle between the radius vector r and the normal to the aperture. Eq. 2 can be rewritten for the case of centerline intensity ie. $\theta = 0$ in terms of the total particle gas flow through the orifice N as

$$I = N/\pi \quad \text{atoms/sr-sec} \qquad (3)$$

The number of particles passing through the opening with a given velocity V follows from Maxwells law and is given by

$$I(v)\,dv = 2I_o\left(\frac{v}{\alpha}\right)^3 e^{-v^2/\alpha^2} \frac{dv}{\alpha} \quad \text{atoms/cm}^2\text{-sec} \qquad (4)$$

where $\alpha = \sqrt{\frac{2kT}{m}}$ is the most probable velocity.

The above equations represent the physical situation providing $\lambda >> d$ holds; however, as the oven pressure is raised there is a gradual transition from free molecular to viscous flow. In this transition region the intensity is limited by lack of collimation due to collisions between molecules in the beam which results in a low I/N ratio and consequently requires excessive pumping capacity to remove the background gas for the useful intensity obtained.

C. Properties of the Nozzle Beam.

Kantrowitz and Grey (Ka51) proposed a supersonic nozzle source for the production of molecular beams as shown in Fig. 4.

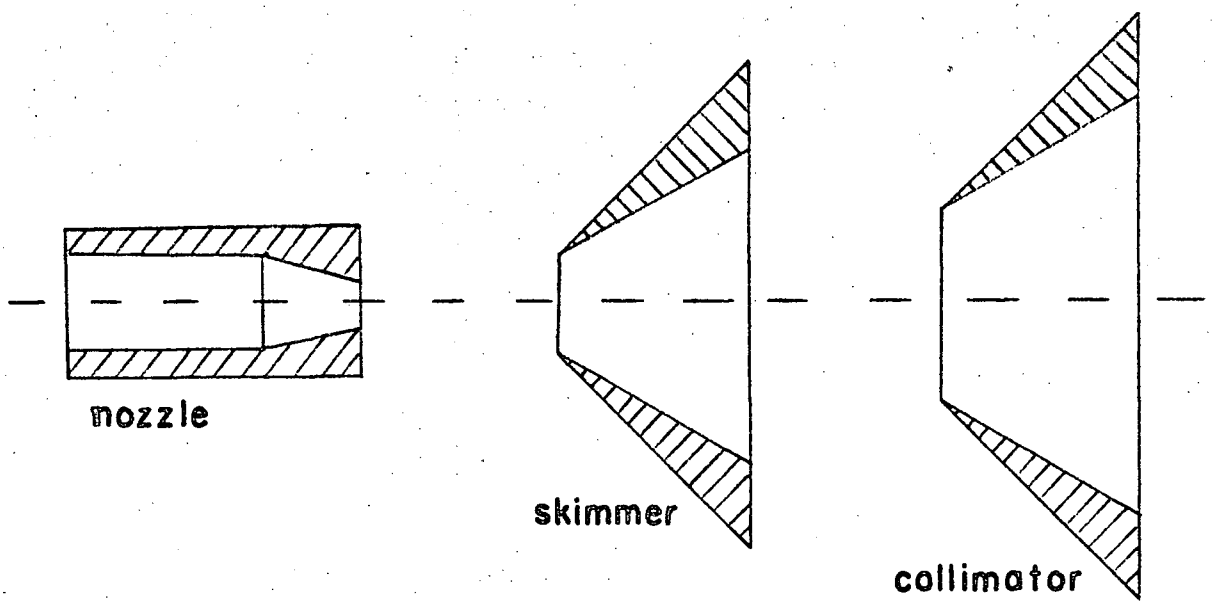

Fig. 4 Schematic Representation of Nozzle Beam Source.

The cross section of their nozzle was shaped to produce a flow with a predetermined Mach number M, equal to the ratio of the velocity of mass motion W to the local velocity of sound a. The core of the beam so produced would be extracted with a suitably shaped skimmer and collimator system with no anticipated interaction between the skimming apertures and the beam. The obvious advantages of such a system were the large increase in intensity and considerable reduction in velocity spread of the beam produced when compared to an oven beam. The large intensity increase arises because of the high gas densities in nozzle flows compared to the low gas densities in molecular beam flows. The attainment of beams with a velocity of mass motion in excess of the local sonic velocity results in a velocity distribution considerably narrower than that achieved with oven beams. It was soon discovered, however, that it was not possible

to produce a beam of controlled properties, that is a gas flow characterized by a predetermined Mach number using the theoretically shaped nozzle nor was it possible to extract the beam produced without interference between the skimming elements and the background gas. The nature of the beam actually produced is discussed in the following sections.

(1) Gas Flow Through a Nozzle.

The mass gas flow, G, through a nozzle for one-dimensional, frictionless adiabatic flow is given by (Sh53):

$$G = Nm = A^* \left(\frac{2}{\gamma+1}\right)^{\frac{1}{\gamma-1}} \sqrt{\frac{2m}{k}\frac{\gamma}{\gamma+1}} \quad \frac{P_o}{\sqrt{T_o}} \qquad (5)$$

where A^* = effective cross sectional area of the nozzle.

γ = ratio of specific heats.

po and To are the stagnation pressure and temperatures upstream of the nozzle entrance, that is the pressure and temperature of the gas in the region where the flow is essentially completely random. "One dimensional flow" means that the flow properties are assumed to be constant in any plane perpendicular to the direction of flow and hence applies to the case of a gas flowing through a nozzle of varying cross-sectional area.

The effective cross sectional area of the nozzle is under certain conditions less than the actual geometrical area because of viscous effects. The ratio of effective area to actual geometrical area is known as the discharge coefficient. Govers, Le Roy and Deckers (Go69) give experimental values of

this coefficient for helium gas passing through a nozzle of diameter d as a function of nozzle Reynolds number, $R_e = \frac{4mN}{\pi d \eta}$, based on experimental flow N and viscosity η at stagnation conditions. Their results for Helium are shown in Fig. 5 at stagnation temperatures between 295°K and 1204°K using a nozzle with d = 0.266 mm. Although the results do not collapse onto a single line they do show what fraction of the theoretically calculated flow will be achieved under experimental conditions characterized by a given Reynolds number at temperatures of 295°K and 1204°K. Unfortunately no results are available for temperatures near 7°K where our nozzle will operate. In spite of the fact our nozzle will operate at Reynolds numbers in excess of 600 it appears possible that the discharge coefficient may be considerably below unity. This however presents no problems.

(2) The Free Jet Expansion.

Consider an orifice of diameter d as shown in Fig. 6 with a near vacuum on one side and a pressure sufficiently high on the other side that slows can be treated by continuum gas dynamics techniques, that is $\lambda \ll d$, on that side. The flow through such an opening (As66) forms a jet as shown in Fig. 6 defined by a barrel shock and the Mach disk. The Mach disk and barrel shock form the boundary between continuum and free molecular flow. In this "zone of silence" the flow expands isentropically unaffected by the presence of background gas outside the jet boundary and can be treated by methods of continuum gas dynamics. This expansion has been described

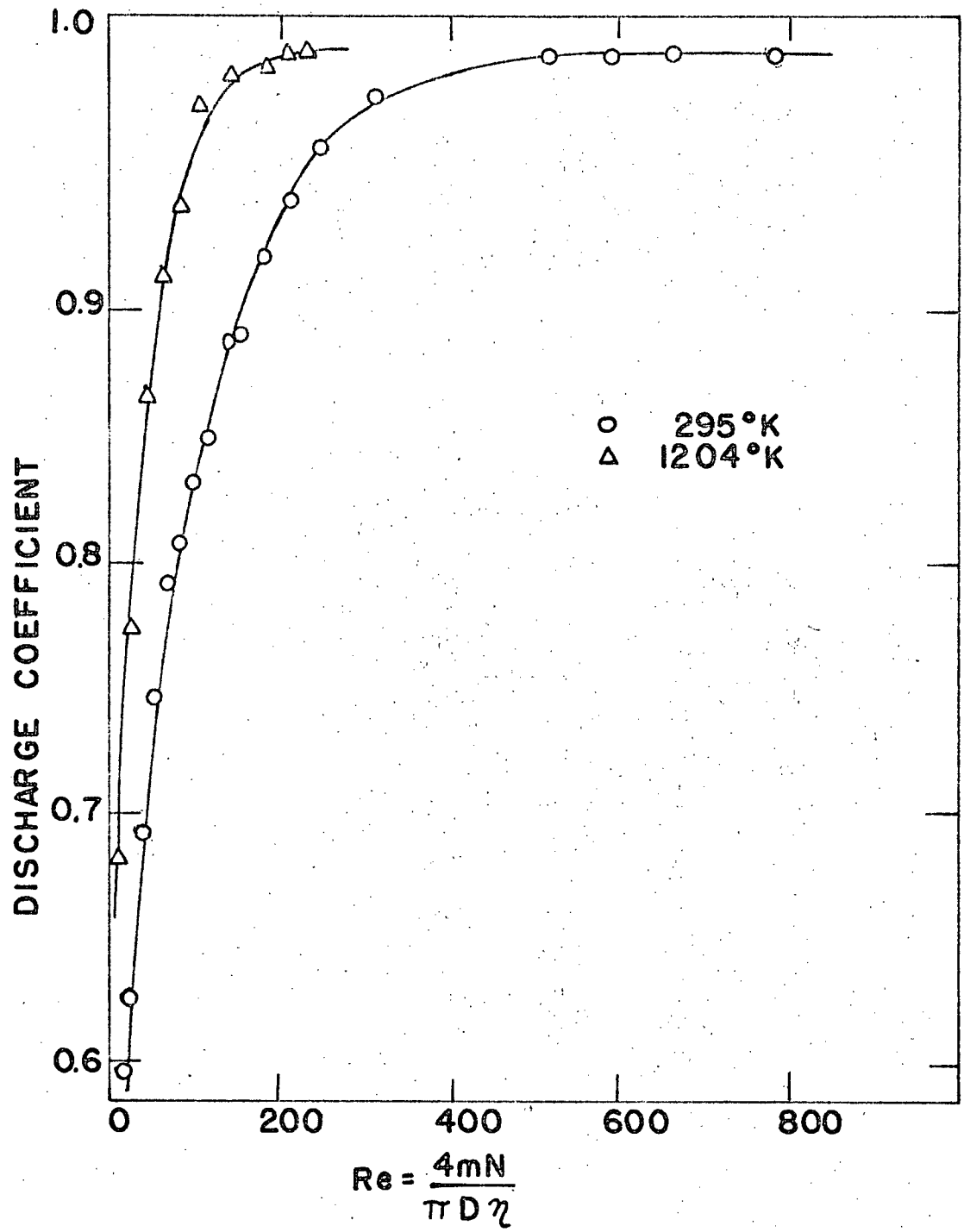

Fig. 5 Discharge Coefficient vs. Reynolds Number based on Experimental Flow and Viscosity at Stagnation Conditions

theoretically for $\gamma = 1.4$ by Owen and Thornhill (Ow52) using the method of characteristics and confirmed experimentally by Reiss (Fe63) and Sherman (Sh63).

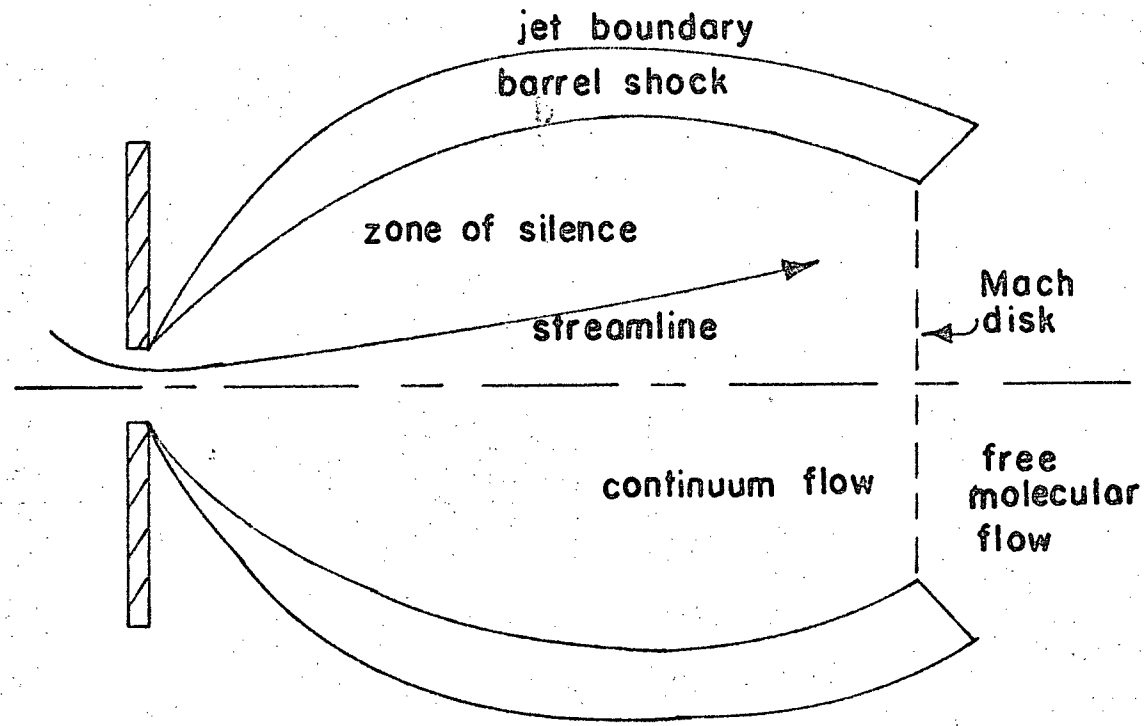

Fig. 6 Schematic Representation of Flow from an Orifice into an Evacuated Region.

Their solution is applicable to any jet flowing into any external pressure in that region bounded by the orifice and the first wavefront which registers the existance of an external pressure outside the jet. Askenas and Sherman (As66) extended Owen and Thornhills' solution to gases with $\gamma = 1.67$ (eg. Helium). They suggest the following formula for the centerline Mach number of a free jet:

$$M = B\left(\frac{x-x_o}{d}\right)^{\gamma-1} - \left(\frac{\frac{1}{2}\left(\frac{\gamma+1}{\gamma-1}\right)}{B\left(\frac{x-x_o}{d}\right)^{\gamma-1}}\right) + C\left(\frac{x-x_o}{d}\right)^{-3(\gamma-1)} \qquad (6)$$

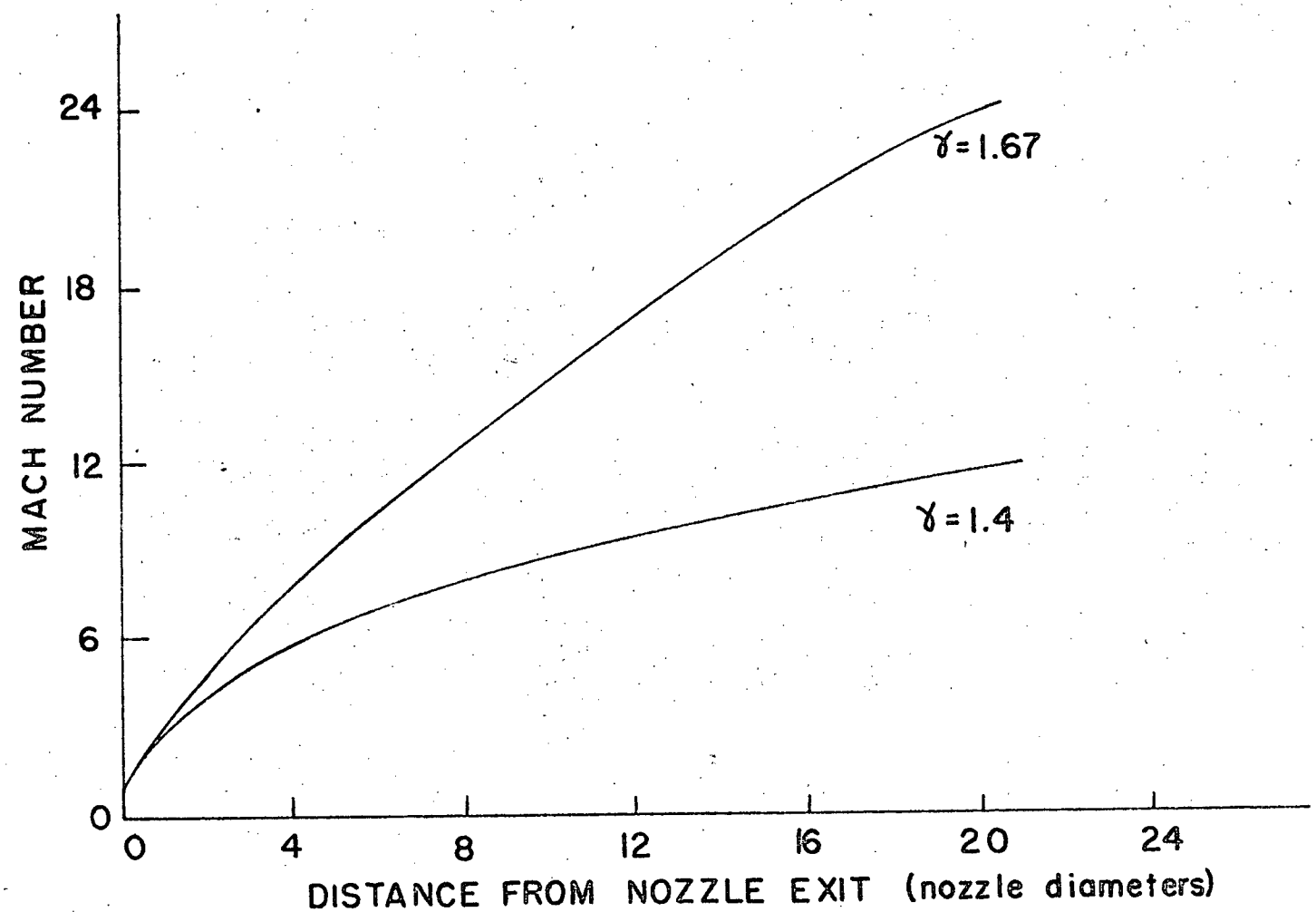

Fig. 7 Distribution of Mach Number Along the Axis of Symmetry of the Expanding Jet.

where x = distance from orifice along the centerline; B, C and X_o are constants such that for $\gamma = 1.67$; B = 3.26, C = 0.31 and $\frac{X_o}{d} = 0.075$. This three term formula is accurate for $X \geq d$ with maximum deviations from the characteristic data of $\sim \frac{1}{2}\%$ of M. The calculated values are shown graphically in Fig. 7. It is interesting to note that these results are independent of the nozzle temperature and pressure.

For adiabatic flow with densities sufficiently high that methods of continuum gas dynamics may be applied, the local pressure and temperature p_1 and T_1 of a beam, that is the pressure and temperature measured in a reference frame moving with the velocity of mass motion W as the beam expands through a nozzle, may be expressed in terms of the nozzle stagnation conditions and the local Mach number (Em58). This treatment gives

$$\frac{T_1}{T_o} = \frac{1}{1+\left(\frac{\gamma-1}{2}\right)M^2} \qquad (7)$$

and

$$\frac{P_1}{P_o} = \left(\frac{1}{1+\left(\frac{\gamma-1}{2}\right)M^2}\right)^{\frac{\gamma}{\gamma-1}} \qquad (8)$$

The local sound velocity $a = \sqrt{\frac{\gamma k T_1}{m}}$ (9)

and the velocity of mass motion $W = M\sqrt{\frac{\gamma k T_1}{m}}$ (10)

In the inertia dominated region of the free jet expansion Askenas and Sherman (As66) have shown that the density decreases along each streamline in proportion to the inverse square of distance from an apparent source a distance x_o downstream from the actual orifice. They also show that the calculated angular dependence of the density field can be

represented by the simple formula

$$\frac{n(r,\theta)}{n(r,0)} = \cos^2\left(\frac{\pi\theta}{2\phi}\right) \qquad (11)$$

with an accuracy of about 3% of n(r,o). That is, their data from a method of characteristics solution differs less than 3% from the results obtained using Eq. 11. The constant ϕ depends on the specific heat ratio for the gas used; thus for $\gamma = 1.67$, $\phi = 1.365$. The distance from the orifice to the Mach disk X_m is given by Askenas and Sherman (As66), as a function of the pressure ratio Po/Pbg across the orifice, by:

$$\frac{X_m}{d} = 0.67 \left(\frac{P_o}{P_{bg}}\right)^{1/2} \qquad (12)$$

where Pbg is the background pressure in the nozzle exhaust region. This formula gives reasonable agreement to experimental results independent of the value of γ, in the region $15 \leq P_o/P_{bg} \leq 17{,}000$.

(3) The Freezing Surface.

The free expansion discussed earlier essentially transfers energy from the internal degrees of freedom of the molecules to directed mass motion. Thus we may consider the beam molecules to be characterized by some local temperature T, in a local reference frame moving with the velocity of mass motion. A certain collision frequency between the molecules of the beam is required to support this continuous reduction in the randomness of the motion of the molecules with respect to the local reference frame. When the gas density gets sufficiently low and this minimum collision frequency is not maintained, the

expansion to higher Mach number ceases and the system "freezes" at a given temperature. Once this freezing region is reached the gas continues to expand radially, the intensity decreasing as $1/r^2$ but with no further change in temperature. It should be noted that the location of this freezing surface is not coincident with the Mach disk location.

Empirical determination of the terminal Mach number M_t at which translational freezing occurs based on nozzle stagnation conditions, has yielded the result (An65).

$$M_t = 1.18\ (Kn_o)^{\left(\frac{1-\gamma}{\gamma}\right)} \qquad (13)$$

This result was obtained for Argon beams at room temperature; subsequent investigation has shown that it also holds for other gases. However, Abuaf et al (Ab66) have shown that experimental values for helium fall below the results predicted using this equation; his results are shown in Fig. 8. Knuth (Kn64) calculated the location of the freezing planes using the relaxation times for the collision processes involved. He found for a monatomic gas, $\gamma = 5/3$ that

$$M_t = 0.66\ \left(\frac{0.99}{Kn_o}\right)^{6/11} \qquad (14)$$

where Kn_o = the Knudsen number based on stagnation conditions. Knuth's results are also shown on Fig. 8. The agreement with experimental results for Argon is poor for low Knudsen numbers but improves for larger Kn_o. Naturally the transition between the continuum to transition and then free molecular flow is not a sudden process so that the above formula and the model on which they are based only represents a first approximation to the real situation which is properly described only by a

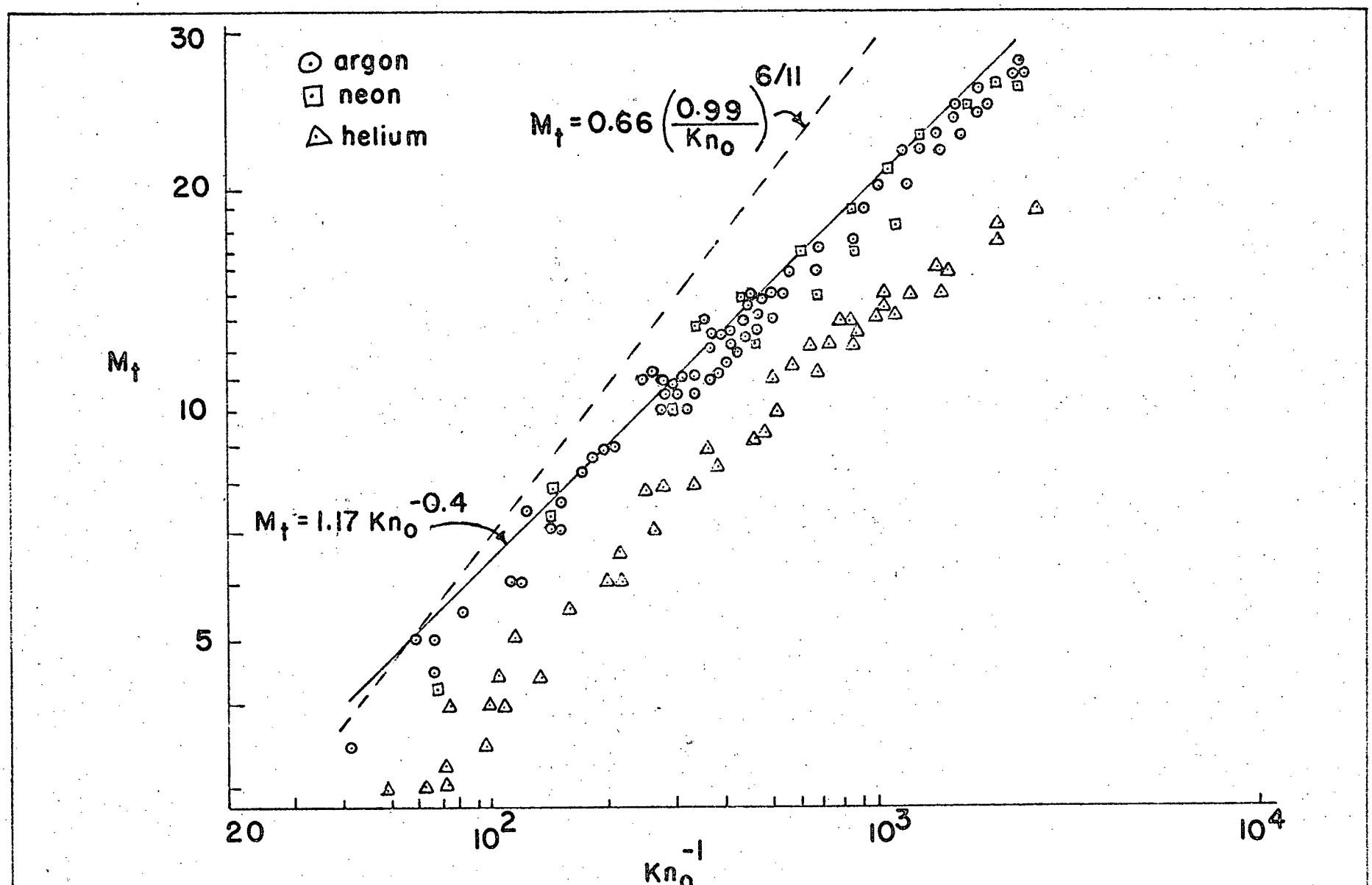

Fig. 8 Terminal Mach Numbers as a Function of Inverse Knudsen Number based on Stagnation Conditions at the Nozzle.

complete solution of the kinetic equations.

(4) Velocity Distribution of Particles in the Beam.

Particles in an expanding jet from a miniature supersonic nozzle can be considered to move with respect to a local reference frame which is moving radially outwards from the nozzle with the velocity of mass motion. This behaviour illustrated in Fig. 9 includes the presence of the freezing surface. For simplicity the results presented in this and the next section will assume the freezing surface is coincident with the skimmer opening. Because the radial density variation is the same on both sides of the freezing surface, the inclusion of the freezing surface upstream of the skimmer will have no effect on the results obtained. The particles as seen in the moving frame have a Maxwellian velocity distribution characterized by some local temperature. In fact, careful studies of the velocity distribution of nozzle beams that consider both the radial and angular dependence of the velocity distribution find that the Maxwellian distribution is characterized by one temperature $T_{\parallel}$ in the radial direction u_1 and another $T_{\perp}$ in the u_2 and u_3 directions (Fi67). At the orifice $T_{\parallel} = T_{\perp}$ but due to differences in the rates for translational relaxation the two temperatures progress to the different terminal values achieved when the expansion stops. Thus the velocity distribution function can be written

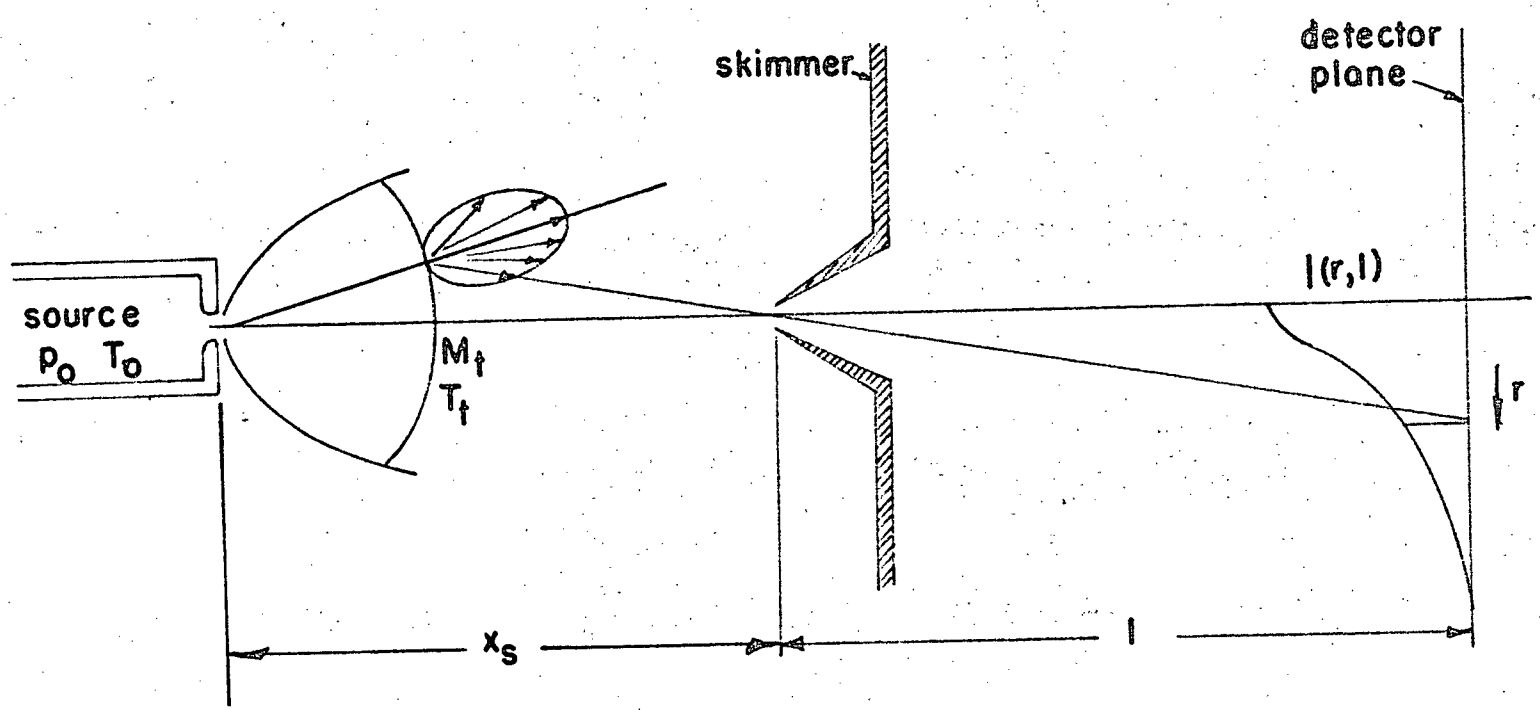

Fig. 9 Schematic Representation of Radially Expanding Flow through a Skimmer to a Detector.

$$f(u_1)\,f(u_2)\,f(u_3)\,du_1\,du_2\,du_3$$

$$= \left(\frac{m}{2\pi kT_{\parallel}}\right)^{\frac{1}{2}}\left(\frac{m}{2\pi kT_{\perp}}\right) \exp\left[-\frac{m}{2kT_{\parallel}}(u_1-w)^2\right] \exp\left[-\frac{m}{2kT_{\perp}}u_2^2\right] \qquad (15)$$

$$\times \exp\left[-\frac{m}{2kT_{\perp}}u_3^2\right] du_1\,du_2\,du_3$$

This function represents the fractional number of particles in the beam with velocities u_1, u_2, u_3 in some range du_1, du_2, du_3. If velocity distribution measurements are made only along the beam axis it is not possible to determine both $T_{\parallel}$ and $T_{\perp}$ and it is common to set $T_{\parallel} = T_{\perp} = T_1$, thus resulting in the simplified velocity distribution

$$f(u_1)\,f(u_2)\,f(u_3)\,du_1\,du_2\,du_3$$

$$= \left(\frac{m}{2\pi kT_1}\right)^{3/2} \exp\left[\frac{-m}{2kT_1}\left\{(u_1-w)^2 + u_2^2 + u_3^2\right\}\right] du_1\,du_2\,du_3 \qquad (16)$$

The above equations give the velocity distribution of particles at some point in the beam. The fractional intensity or differential intensity distribution function, $I(u) = \frac{dI}{du}$, of particles with a given velocity arriving at a detector depends on the restraints imposed by the geometry of the complete nozzle system in summing over all possible velocities to obtain the total intensity of particles at the detector. If parallel flow at the entrance to the skimmer is assumed (one of Kantrowitz and Grey's original assumption) Eq.B8 of Appendix B gives

$$\frac{dI}{du} = \frac{I_{is}\,\pi\,\sin^2\alpha_s}{w}\left(\frac{m}{2\pi kT_1}\right)^{3/2} g(u) \qquad (B18)$$

where $$g(u) = u^3 e^{-\frac{m}{2kT_1}(u-w)^2} \qquad \text{(B19)}$$

and Iis is the centerline isentropic beam intensity expected from a free jet expansion unaffected by the presence of a skimmer as discussed in Section 3C and α_s is the half angle subtended by the skimmer with respect to the nozzle exit as shown in Fig. 48. Now if the radial flow divergence of the beam at the skimmer is included in calculating the intensity at the detector Eq. B8 of Appendix B gives

$$\frac{dI}{du} = \frac{I_{is}}{w^2}\left(\frac{m}{2\pi kT_1}\right)^{1/2} g(u)\ G(u) \qquad \text{(B20)}$$

where g(u) is as before and

$$G(u) = \frac{1}{u}\left\{1 - \exp\left[-\left(\frac{2uwm}{2kT_1}\right)(1-\cos\alpha_s)\right]\right\} \qquad \text{(B21)}$$

now $\frac{2uwm}{2kT_1} \approx \gamma M^2$ thus

when the skimmer subtends a very small half angle

$2\gamma M^2 \sin^2\left(\frac{\alpha_s}{2}\right) << 1$ and $G(u) \propto \frac{u}{u} = \text{constant}$

Then $\frac{dI}{du} \propto g(u)$ as in Eq. B18 where the flow at skimmer is assumed parallel. When the skimmer subtends a large half angle

$2\gamma M^2 \sin^2\left(\frac{\alpha_s}{2}\right) >> 1$ and

$\exp\left[-2\gamma M^2\right] \sin^2\left(\frac{\alpha_s}{2}\right) \approx 0$ and

$G(u) \approx \frac{1}{u}$

thus modifing the velocity dependence of Eq. B8 to

$$\frac{dI}{du} \propto g(u)\, G(u) = u^2 \exp\left[-\frac{m}{2kT_1}(u-w)^2\right] \qquad (17)$$

when the radial dependence of the flow is considered for flows with appropriate Mach number and skimmer radius. This is the form of the differential intensity distribution function recommended

by Hagena and Morton (Ha67)

(5) Intensity Available From Nozzle Beams.

(i) Freely Expanding Jet.

The case of the freely expanding jet without a skimmer or collimator using Eq. 11 to represent the density field about the beam axis has been considered. As shown in a simple calculation given in Appendix A the expected flux density I on the beam axis is

$$I = 0.6N \text{ atoms/steradian - sec} \qquad (A5)$$

where N = G/m = particle flow through the nozzle given from Eq. 5. The equivalent expression for molecular flow beam is

$$I = N/\pi \text{ atoms/steradian - sec} \qquad (3)$$

(ii) Beam Intensity Downstream from the Skimmer.

The theoretically expected beam intensity after the gas has passed through a skimmer is discussed in Appendix B. Two cases are considered: One assumes the conditions of the Kantrowitz and Grey model (Ka51), namely:

(1) isentropic flow upstream of the skimmer

(2) parallel flow at the skimmer

and (3) collisionless flow downstream of the skimmer.

while the other considers the case as suggested by Hagena and Morton (Ha67) where criterion (2) in the Kantrowitz and Grey model is modified to take into account the divergent nature of the flow at the skimmer.

The result of this analysis is

(1) Parallel flow at skimmer entrance.

$$I = I_{is} \sin^2\alpha_s \left(\frac{3}{2} + \frac{\gamma M^2}{2}\right) \qquad \text{(B17)}$$

(2) Radially diverging flow at skimmer entrance.

$$I = I_{is}\left(1 - \cos^2\alpha_s\, e^{-\frac{\gamma M^2}{2}\sin^2\alpha_s}\right) \qquad \text{(B12)}$$

Both Eqs. B12 and B17 are for the case of the detector-skimmer separation $\ell > 7 X_s$, the nozzle-skimmer separation, and make use of the simplifications afforded by assuming $M > 3$.

Eq. B17 based on the Kantrowitz-Grey model predicts an intensity proportional to the skimmer area but it is clear that it predicts unreasonably high intensities $I > I_{is}$ if the skimmer is so large that $\left(\frac{3}{2} + \frac{\gamma M^2}{2}\right)\sin^2\alpha_s > 1$. This unphysically high intensity is due to the neglect of the divergent nature of the flow approaching the skimmer. Including the divergent nature of the flow in the calculation results in Eq. B12. This second equation no longer shows an unlimited increase of I with either M or $\sin\alpha_s$ but predicts an intensity approaching I_{is}, the intensity one would expect if no skimmer had been present at all.

(6) Deviations From Ideal Behaviour.

Experimental investigations have shown that the intensities predicted in the previous section are not always achieved in practice. This discrepancy between theory and experiment is caused at least in part by the assumption in the theoretical calculation that

(1) the beam in unaffected by the presence of the skimmer

and (2) the beam is unaffected by the presence of background gas

The effect of these idealizations is often a severe reduction of beam intensity below that expected from the previous analysis.

The presence of a shock wave at the skimmer entrance was expected to cause a reduction of the beam intensity due to the presence of the skimmer but the electron-beam flow-visualization photographs of McMichael and French (McM66) failed to detect any local build up of gas molecules upstream of the skimmer. The skimmer interference is now postulated to occur downstream of the skimmer entrance ie. inside the skimmer, and to be caused by a cloud of low velocity molecules whose creation is caused by molecules reflected off the inside of the skimmer. The skimmer degradation of the beam can be avoided by placing the skimmer in a region where $\frac{Kn_s}{M} > 1$ (An66). This criteria generally results in large nozzle-skimmer separations.

Scattering of the beam by background gas occurs in all regions of the apparatus if the pressures are sufficiently high. The beam intensity at a distance ℓ from the source can be calculated using

$$I = I_o \, e^{-\int n\sigma \, d\ell} \qquad (18)$$

where I and I_o are the attenuated and unattenuated beam intensities, n the local gas density and σ the scattering cross section. Scattering of the beam in the nozzle-skimmer region is

a special case, as the presence of the barrel shock partially prevents the beam from scattering in the region between the nozzle and the Mach disk location. Scattering of the beam occurs downstream of the Mach disk and occurs under certain conditions to a lesser extent upstream as well (Br66, An65b). Thus to reduce scattering in the nozzle-skimmer region to a minimum the skimmer should be upstream of the Mach disk location which can be predicted using Eq. 12. This condition usually conflicts with the separation for minimum skimmer interference and hence a compromise situation develops.

Typical experimental intensity profiles obtained as a function of nozzle-skimmer separation are shown in Fig. 30. The intensity maximum is the physical realization of this compromise between background gas scattering and skimmer interference. Downstream of the maximum, background scattering dominates while upstream, skimmer interference dominates. At small nozzle skimmer separations the relatively high beam intensity is caused by the free jet "popping" through the skimmer and expanding towards the collimator which now acts as a skimmer. With increased separation the jet slowly returns to its normal location and skimmer interference is at its maximum hence the minimum in beam intensity at $L/D \sim 5$.

(7) Low Temperature Nozzle Sources and their uses.

Few experimental results exist describing the nature of helium beams formed by nozzles cooled to liquid helium temperatures. Becker, Klingelhofer and Lohse (Be61, Be62) report observing a condensed helium beam with an intensity of

1.2×10^{19} atoms/sr-sec, a velocity of 165 m/sec and a velocity FWHM corresponding to a Mach number of about 80. These results were obtained with a 0.15 mm diameter nozzle operated at 740 Torr. They report no observations of an uncondensed beam at liquid helium intensities. Zapata, Ballard and Cabrera (Za69) have recently made some measurements of intensity and velocity distribution of ^{4}He beams produced by a cryogenically cooled nozzle source. They report a peak intensity of 6×10^{17} atoms/ sr-sec and a beam velocity of 320 m/sec. This corresponds to a nozzle temperature of 10°K. These results obtained with a 0.11 mm diameter nozzle operated at pressures up to 200 Torr are in reasonable agreement with corresponding results presented later in this work. No work has apparently been done with ^{3}He nozzle beams cooled to liquid helium temperature.

The study of condensation fragments in low temperature Argon beams has been carried out by Milne and Greene (Mi67) using mass spectrometer techniques and Audit and Rouault (Au69) using electron diffraction techniques. Both these experimenters were interested in studying the intermolecular potential acting between groups of Argon atoms. Milne used these experimental measurements to test theoretical calculations for the concentration of dimers, trimers etc. in a partially condensed beam. Hopefully studies with helium beams similar to those made with argon beams will show results attributal to quantum effects which would be present with helium at low temperatures but which would not have played a noticeable role in the case of Argon. The use of both ^{3}He and ^{4}He may result in interesting

differences because of the Fermi-Dirac and Bose Enstein Statistics obeyed by the two gases.

Becker et al (Be54, Be56, Be61, Be62) in their original work with low temperature nozzle beams were interested in studying condensation phenomena. Partially condensed beams formed from a mixture of the isotopes, ^3He and ^4He, might be used to preferentially enrich the resulting beam with one of the isotopes. Such a technique at higher temperatures could possible be used in the separation of light and heavy water vapour, a process of considerable commercial interest. Isotopes can be enriched in the free jet expansion without condensation because of the dependence of the velocity components on the mass of the particles.

Knuth and Fisher (Kn68) have used Argon beams expanded from room temperature to measure viscosity cross sections at temperatures as low as 10°K. Similar studies could be carried out with helium beams starting from room, liquid nitrogen or liquid helium temperatures. Again the availability of beams of both ^3He and ^4He allows comparison between the effects due to their different statistics. As will be mentioned later in this work, the difference in scattering cross section for ^3He and ^4He has been observed for jets expanded from a liquid helium cooled nozzle.

The availability of a low energy helium beam is of interest in the study of gas-surface interaction. Zapata, Ballard and Cabrera (Za69) have constructed a liquid helium cooled nozzle source to allow the study of the surface phonon

spectrum of a crystal by scattering an aerodynamic beam of particles off a pure, isotropic crystal.

A low temperature helium beam may be of use in the study of the free jet expansion itself, in particular in the nature of the translational relaxation effects which even for helium beams expanded from room temperature show a behaviour different from that of most other gases.

CHAPTER IV

THE POLARIZED $^3He^+$ BEAM SOURCE

A. The Low Temperature Atomic Beam Source.

(1) General description of Atomic Beam Source.

Fig. 10 shows the full atomic beam apparatus. ^3He gas precooled to liquid nitrogen temperature passes through a cryostat filled with liquid helium and subsequently flows through a nozzle, skimmer and collimator system thus forming the atomic beam.

The copper cryostat weighing 10 kg is supported at the top by a single stainless steel tube. The liquid helium entering the cryostat passes through a transfer line inserted through the center of this tube; the evaporating gas passes up inside the support tube through a heat exchanger used to precool the incoming ^3He gas and then back to the helium recovery system. The bottom of the cryostat is connected to the liquid nitrogen cooled shield by a thin stainless steel bellows, acting as a differential pumping bulkhead.

The design of the cryostat, its supports and connections along with the quality of the vacuum surrounding the chamber, determines the heat leak to the liquid helium and hence the evaporation rate. The calculated and measured heat leaks of the various components of the cryogenic system in different stages of assembly are summarized in Table 1. The heat leak was determined by measuring the rate of helium gas boiloff from the cryostat. The reduction of the radiation heat load from

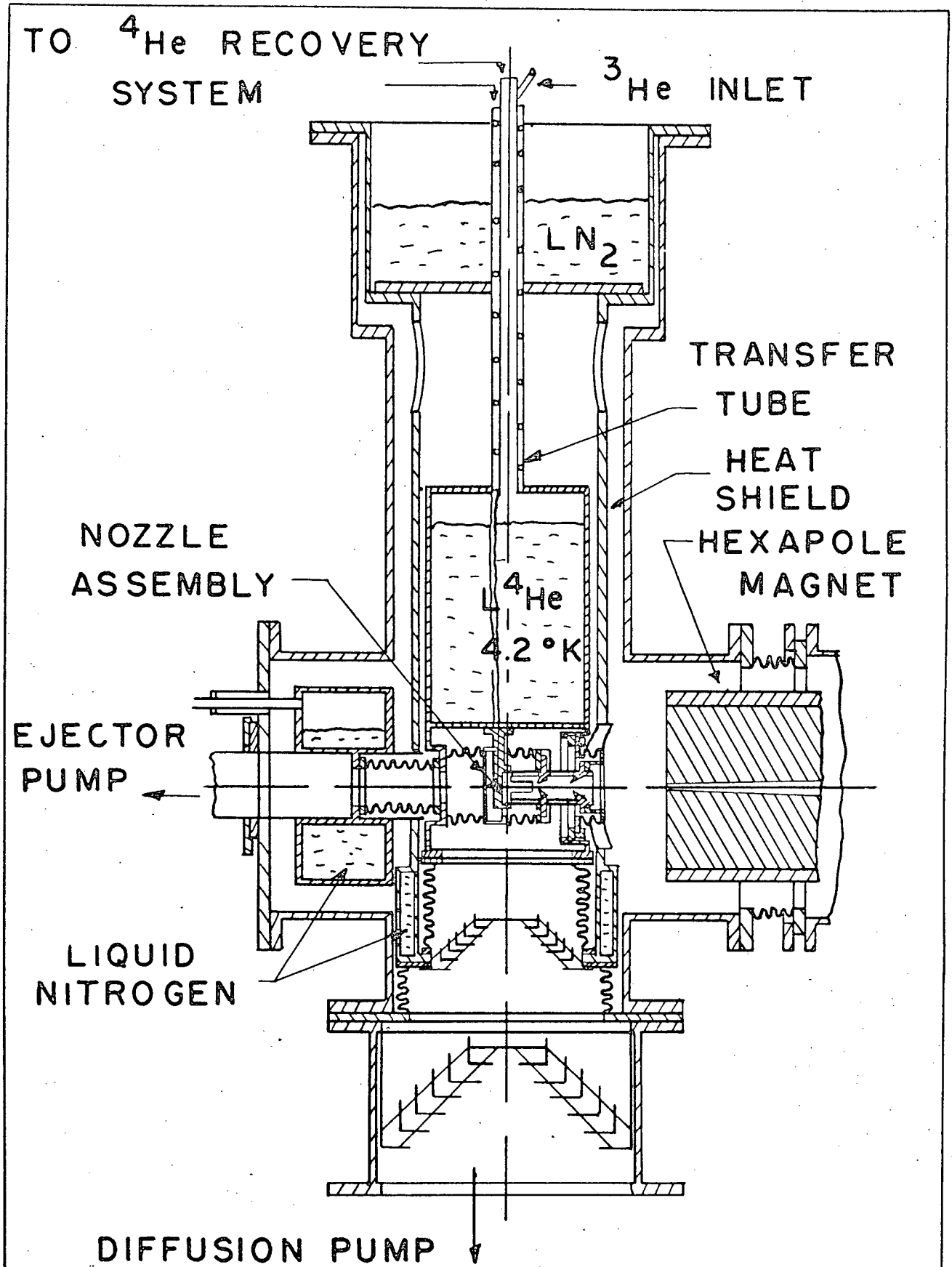

Fig. 10 The Low Temperature ^{3}He Atomic Beam Source.

Table 1

Detailed Summary of Heat Leaks into the Cryostat of the Low Temperature Atomic Beam Source.

System Condition	Measured heat leak (watts)	Expected heat leak (watts)	Finally reduced to (watts)
Stripped cryostat (no bellow; solid plates over all openings)	0.25	0.34	0.2
Bellows between 4°K cryostat and copper heat shield	0.16	0.16	0.16
Radiation over 10" diffusion pump (pump not operating)	0.3	0.0	0
Radiation baffle on Cu heat shield	0.76	0.0	0.16
Pumping to Leybold pump	0.63	0.06	0.009
Operation of large diff pump	0.2	0.0	0.06
Pumping ports on Cu heat shield	0.25	0.0	0
Total	2.55	0.56	0.67

300°K surfaces by painting 77°K baffles with high emissivity aqua dag was essential to the succesful operation of the cryostat. The heat load on the system was actually reduced by about 10% when gas flow through the nozzle was introduced. This confirms the expected high efficiency in excess of 98% of the heat exchanger system and also indicates that the cold gas flowing in the channel to the Leybold Ejector pump acted as a sink for a fraction of the heat leak coming through the metal bellows there. The total measured heat leak for the system was 0.6 watts. With a cryostat capable of holding 6 liters of liquid helium this allowed 7 hours operation between fillings. Typical cool down and initial filling of the cryostat required 19 liters of liquid helium. Precooling of the system to 77°K for 8 hours required about 80 liters of liquid nitrogen while the continued operation of the system required 8 liters/hour.

The vacuum pumping system was separated into four parts. One section was used to pump the nozzle-skimmer region; one to pump the skimmer-collimator region; one to pump the region surrounding the cryostat and magnet, and a fourth to pump the ionizer chamber. The pumping system for the nozzle-skimmer region consisted of a Leybold Hg 45 mercury ejector pump with a pumping speed of 45 liters/sec at a pressure of 10^{-1} Torr and 20 liters/sec at 10^{-3} Torr. This pump was capable of operating into a backpressure of 30 Torr for a closed recirculating ^{3}He gas system but was normally provided with a Welch 1402 pump. The skimmer-collimator region was pumped

with a CVC 10" oil diffusion pump having a pumping speed of 4000 liters/sec at pressures below 10^{-3} Torr. The surrounding region was pumped with 2 Heraeus 6" diffusion pumps each having pumping speeds of 1500 liters/sec. The ionizer chamber was pumped with a CVC 6" diffusion pump having a pumping speed of 1400 liters/sec. The 10" and three - 6" diffusion pumps were backed with a Stokes 40 cfm rotary backing pump to maintain the necessary forepressure. The 10" and two Heraeus 6" pumps were provided with water cooled baffles, the Leybold pump was provided with a liquid nitrogen cooled trap and the CVC 6" pump was provided with a freon cooled baffle.

Pressure measurements in the nozzle-skimmer and skimmer-collimator regions were made by means of Pirani gauges attached to the end of long stainless steel tubes with inside diameters of 2.54 mm and 2.4 mm respectively. These tubes passed from the appropriate region through the required thermal and vacuum bulkheads to the outside of the main vacuum chamber. Since one end of the tube was normally at room temperature and the other at either 77°K or 4.2°K corrections for thermal transpiration effects were necessary. These corrections will be discussed in detail in the next section of this chapter.

The pressure in the main system was monitored with an ionization gauge. It was possible to interlock the ion gauge control box trip out circuit to a relay controlling the diffusion pump power to prevent damage to the diffusion pumps should the pressure in the system become excessive. The oil diffusion pumps used Dow Corning 705 Silicone fluid which proved to be a very reliable and robust pump fluid withstanding,

without damage, many accidental exposures to atmospheric pressure.

Nozzle input and nozzle stagnation pressures were measured with 2 Wallace-Tiernan gauges; one 0-760 Torr and the other 0-400 Torr range. For nozzle pressures in excess of 1 Torr the thermal transpiration corrections required were less than 3% and were hence ignored.

Details of the nozzle, skimmer, and collimator system is shown in Fig. 11. The nozzle-skimmer distance could be adjusted by revolving the skimmer-collimator carriage on a screw thread (26 threads per inch) cut on the main nozzle assembly. The gear on the end of the skimmer-collimator carriage could be connected by a gear chain system to a rod passing through the vacuum chamber wall. An O-ring seal allowed the rod to be rotated from outside the vacuum system. One complete revolution of this rod correcponded to 1/8 of a revolution of the skimmer-collimator carriage which increased or decreased the nozzle-skimmer separation by 0.0048 inches. This externally adjustable system functioned only with the nozzle at room temperature as the O-rings freeze at liquid nitrogen temperature and below. Nozzles, skimmers, and collimators of appropriate size and shape could be installed on this framework. Precise alignment was achieved by mounting the framework in a lathe and observing the various apertures with a telescope as the nozzle system was rotated.

(2) Thermal Transpiration Corrections to Pressure Measurements.

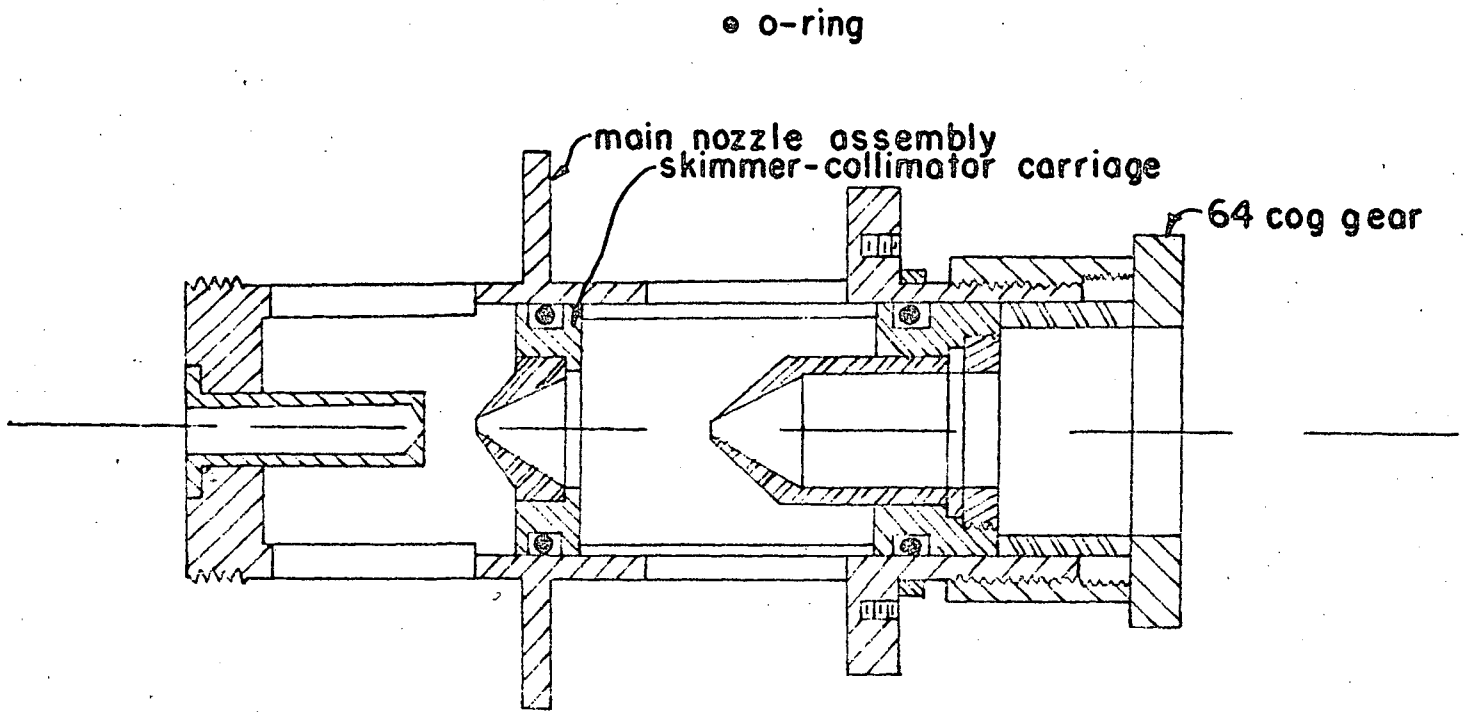

Fig. 11 The Ajustable Nozzle-Skimmer Assembly.

When one end of a pressure sensing device is at a temperature different from the other end it is necessary to correct the measured pressure for thermal transpiration effects.

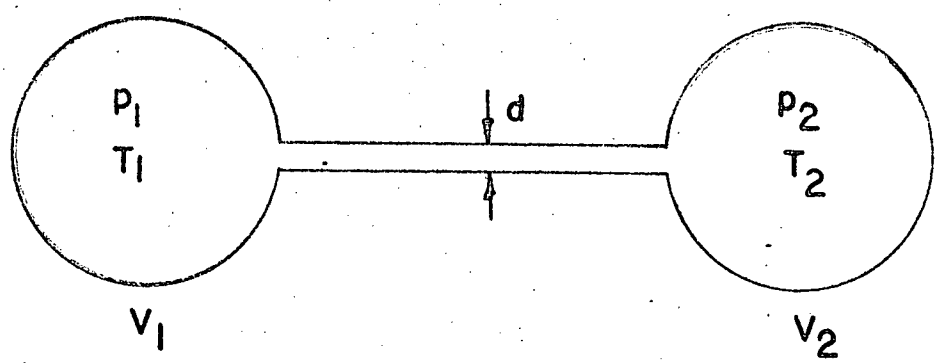

Fig. 12 Conditions for Thermal Transpiration Effect.

A typical situation is shown in Fig. 12 in which two volumes V_1 and V_2 at temperatures T_1 and T_2 are connected by a tube of diameter d. If the density in the volume is such that $\lambda >> d$ then the gas flow through any opening according to Eq. 1 is proportional to $nT^{\frac{1}{2}}$. The steady state is established when

$$n_1 T_1^{1/2} = n_2 T_2^{1/2} \tag{19}$$

now

$$n \propto P/T$$

$$\therefore \frac{P_1}{P_2} = \left(\frac{T_1}{T_2}\right)^{1/2}$$

When collisions between molecules predominate over collisions against the walls, ie. $\lambda << d$, then the condition for equilibrium is $p_1 = p_2$. Numerical values for the ratio p_1/p_2 where $T_1 < T_2$ are presented by Roberts and Sydoriak (Ro56) for ^3He and ^4He. Their results are given as a function of the product $p_2 d$ which allows the necessary correction for tubes of varying sizes to

be easily determined. The length of the tube does not enter into these considerations. The appropriate results from their work relating to the measurement of pressure in the nozzle-skimmer and skimmer-collimator regions are shown in Fig. 13. At the low pressure end the dependence approaches the $\frac{p_1}{p_2} = \left(\frac{T_1}{T_2}\right)^{\frac{1}{2}}$ relationship expected from free molecular flow considerations while at the higher pressure end the dependence approaches the $p_1 = p_2$ dependence expected from continuum considerations.

(3) Carbon Resistor Temperature Measurement.

The temperature of the nozzle in the atomic beam apparatus was measured with a 33 Ω Allen Bradley resistor in one arm of a A.C. Wheatstone bridge operated at 1 K cycle as shown schematically in Fig. 14. It was possible to null the bridge to $\pm 1\ \Omega$ at liquid helium temperatures. The null resistance at near liquid helium temperature as a function of oscillator input voltage is shown in Fig. 15. Normal operation of the bridge was in the plateau region of this curve where the power disipated in the resistor was so small that it did not influence the resistance of the carbon resistor. The calibration of this resistor at room 295°K, liquid nitrogen 77°K, and liquid helium 4.2°K temperature is shown in Fig. 16. The resistance R of such a resistor as a function of temperature T normally can be expressed by the relationship (C152)

$$\left(\frac{\ln R}{T}\right)^{\frac{1}{2}} = a \ln R + b \qquad (20)$$

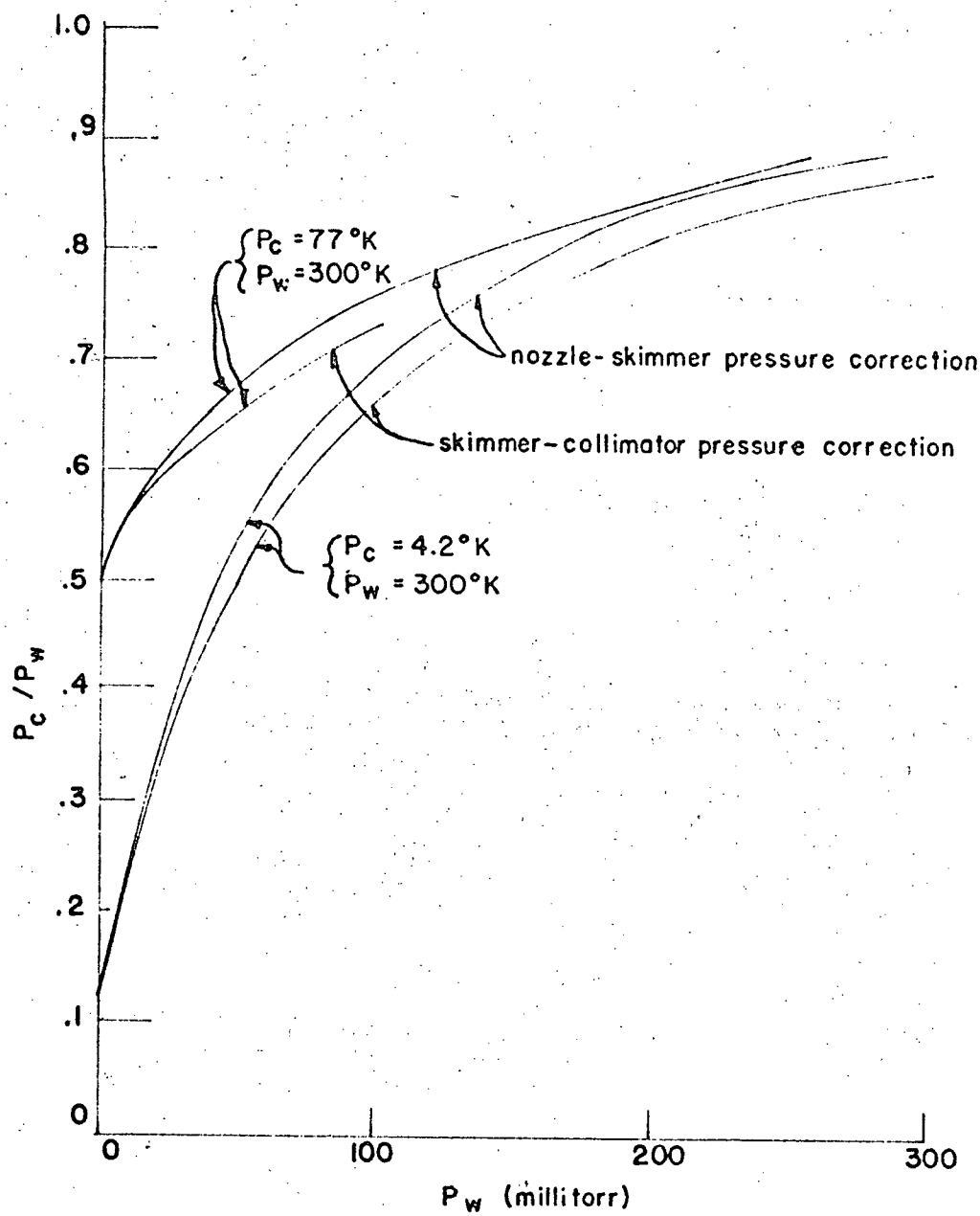

Fig. 13 Thermal Transpiration Corrections to Measurements of Nozzle-Skimmer and Skimmer-Collimator Pressure.

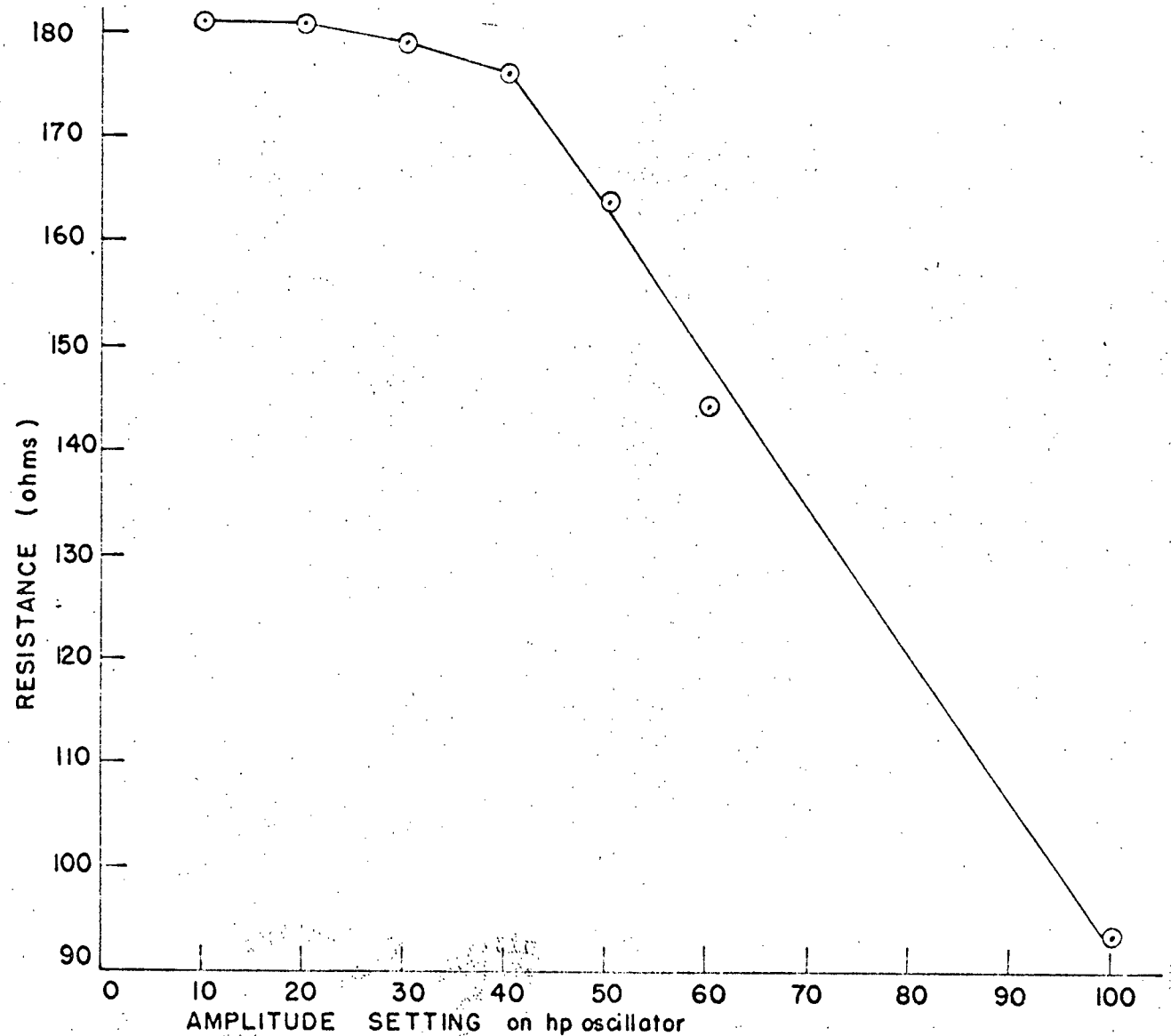

Fig. 15 Input Power Induced Heating of Carbon Resistor Thermometer with Resistor at Near Liquid Temperature.

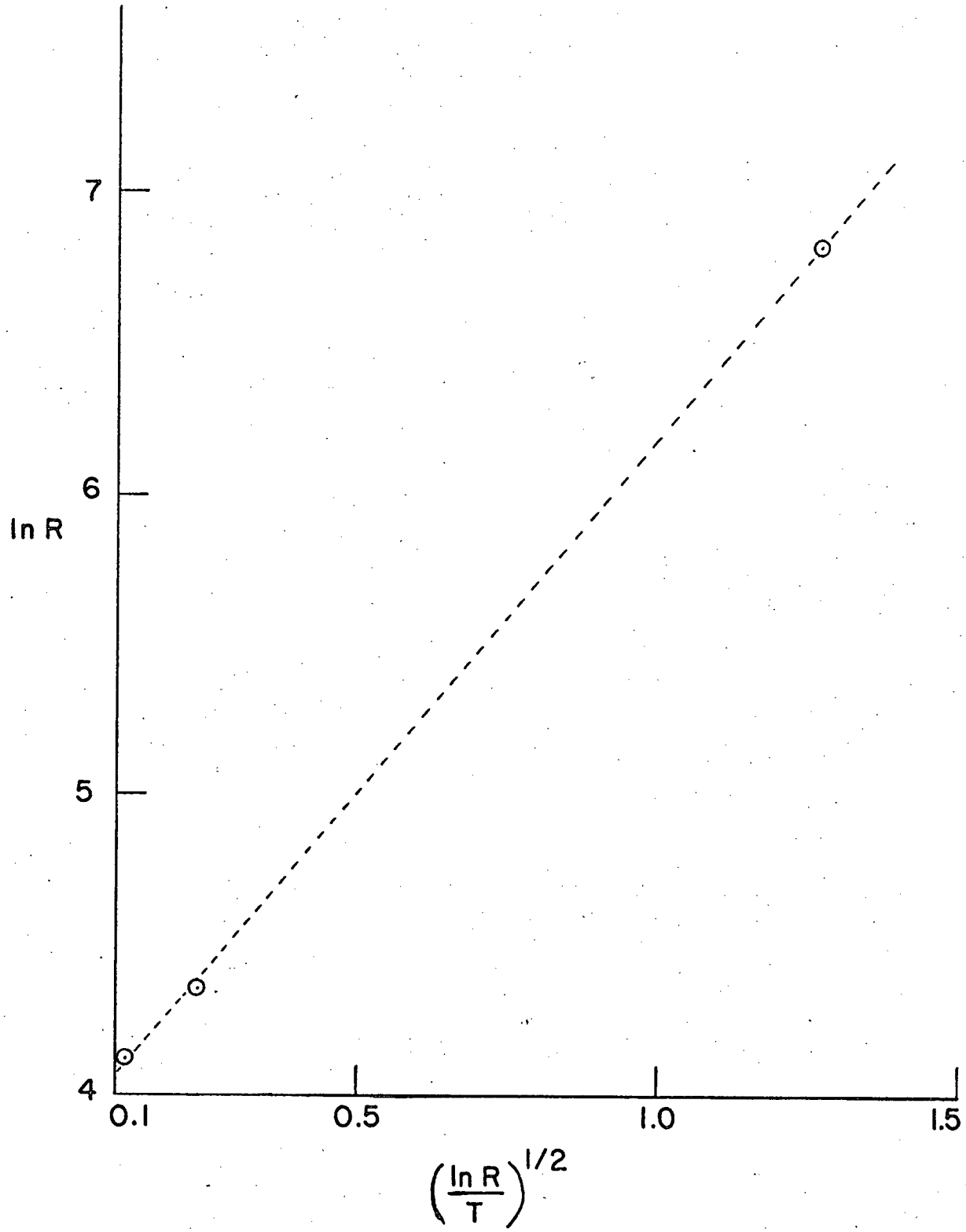

Fig. 16 Calibration of Carbon Resistor Thermometer.

where a and b are suitable fitting constants. The straight dotted line in Fig. 16 is a least squares fit to the experimental points with a = 0.45 and b = -2.17.

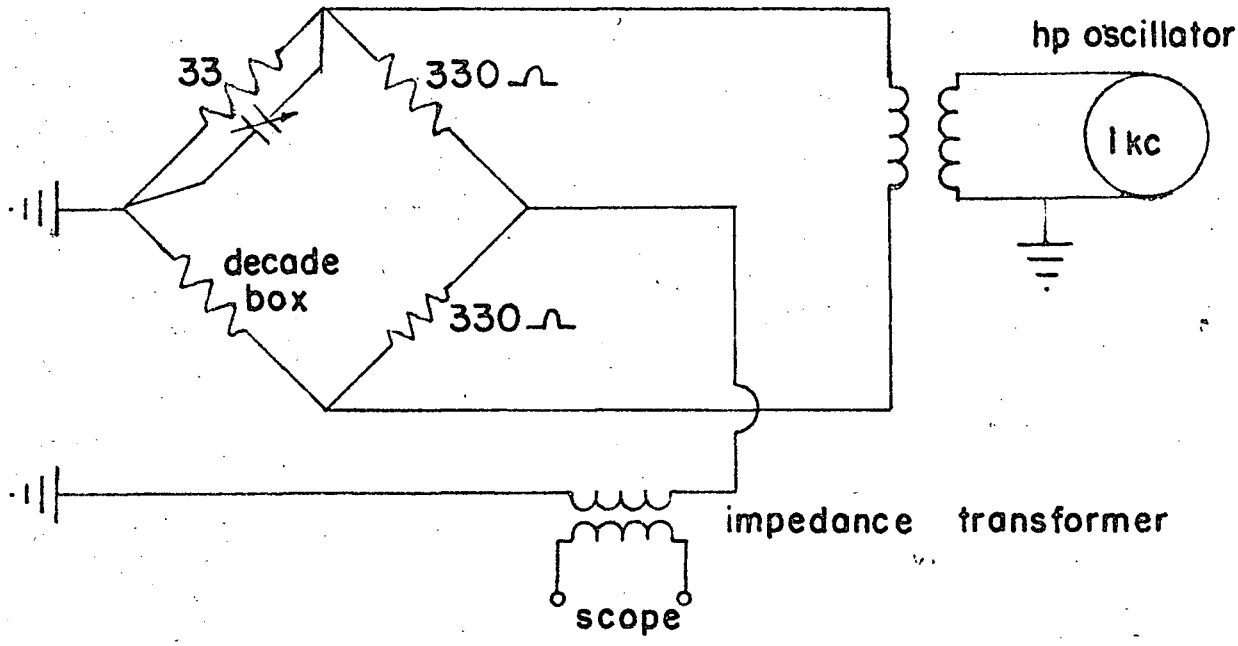

Fig. 14 A.C. Bridge Used to Monitor Resistance of Carbon Resistor Thermometer.

B. The Hexapole Magnet.

The tapered hexapole magnet, 50 cm long, used to separate the particles in the two possible nuclear spin substates of ^{3}He is shown in Fig. 17. This magnet was originally designed by Axen (Ax65) to produce a near 100% separation of nuclear spin states for a Mach 4 nozzle source operating at 2.2°K. The measured field strength in the region of the pole tips as a function of the electrical current through the coils, and the measured value of the magnetic field strength as a function of the radial distance from the central axis are shown in Figs. 18

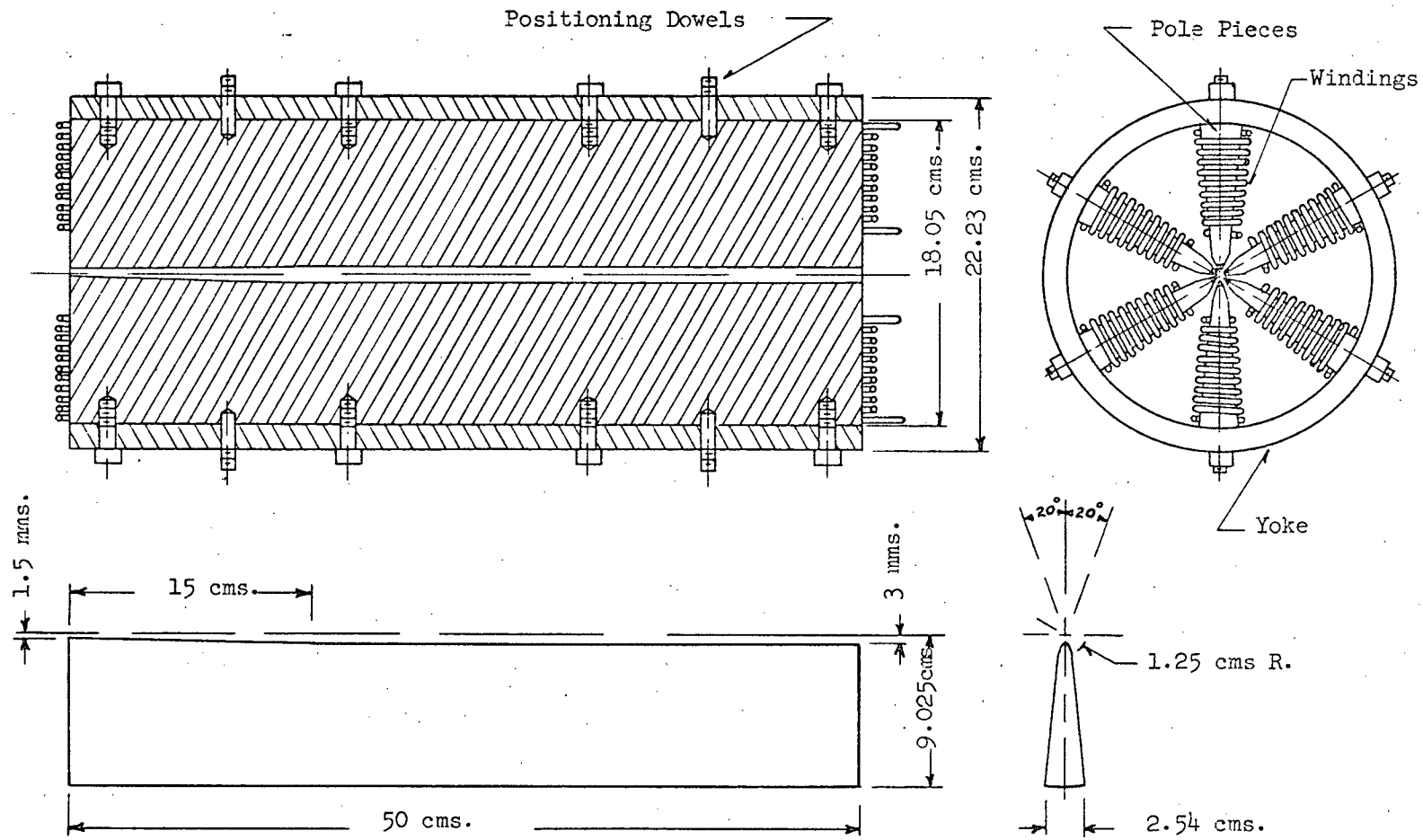

Figure 17. Dimension of the Components of the Hexapole Magnet

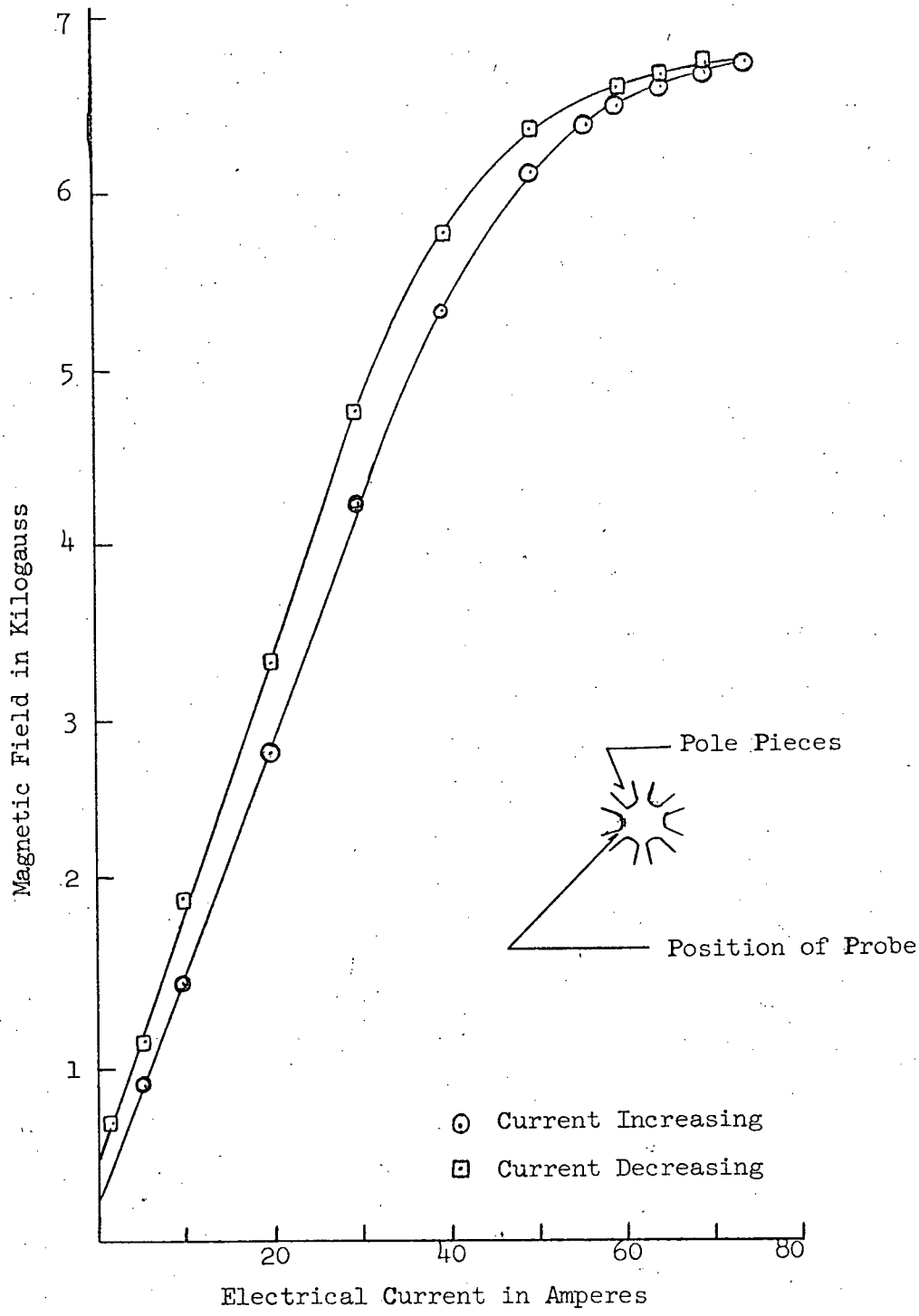

Figure 18. Magnetic Field Strength in the Region of the Pole Tips as a Function of the Electrical Current Through Coils.

and 19 respectively. The average field gradient in the region r = 2.5 to r = 3 mm is 70,000 gauss/cm while the measured field at the pole tips Ho is 9000 gauss.

C. The Electron Bombardment Ionizer.

The ionizer used in this experiment was an electron bombardment type ionizer similar to one built by Weiss (We61) but employing side instead of axial extraction. The development of the prototype ionizer is described by Vermette (Ve64). Vermette used filaments with rectangular cross section while the present ionizer's filaments are circular in cross section. A schematic end view of the ionizer used in this experiment is shown in Fig. 20. The filaments consist of 5 lengths of 0.010" diameter tungsten wire. The active ionization volume has a rectangular cross section 0.25" wide by 0.22" high and a length of 4.75". The ion current is collected on a plate (negatively biased) immediately at the side of the ionizer and was measured using a Hewlett Packard Model 425A DC microvolt-ammeter. The electronics used are shown in Fig. 20A. The above technique was suitable for measuring ion current yields by introducing calibration gases at known pressures into the ionizer chamber. Measurement of ion yields from the actual atomic beam was complicated by the necessity to separate the ion beam yield from the residual background gas ion yield. The lack of a bulkhead separating the ionizer region from the magnet vacuum chamber and also excessive outgassing of the ionizer during operation was mainly responsible for this condition. These two difficulties were overcome by the installation of a beam chopper between the

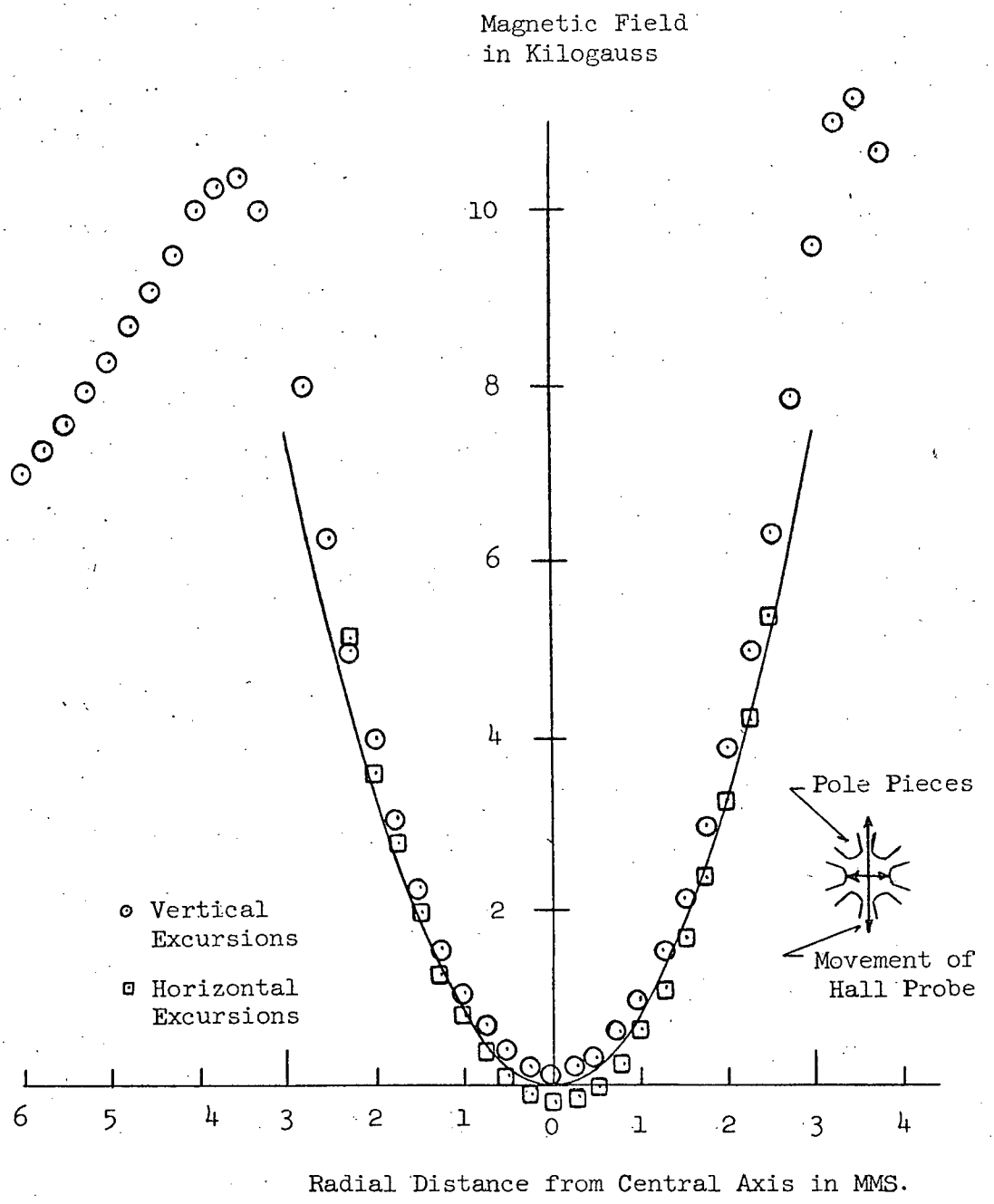

Figure 19 Measured Value of Magnetic Field Strength as a Function of the Radial Distance from Central Axis.

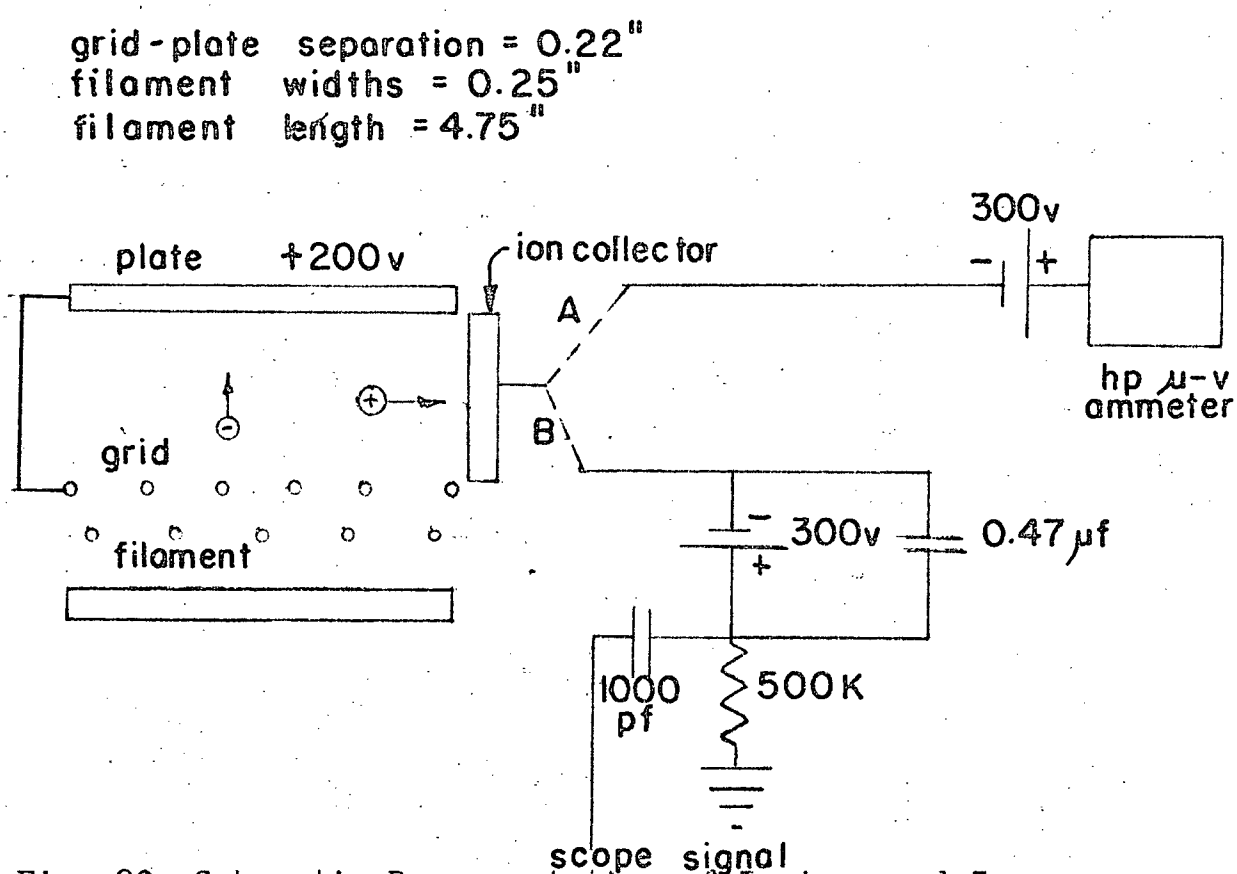

Fig. 20 Schematic Representation of Ionizer and Ion Measurement Apparatus. (A) D.C. Current Measurement (B) Chopped Current Measurement

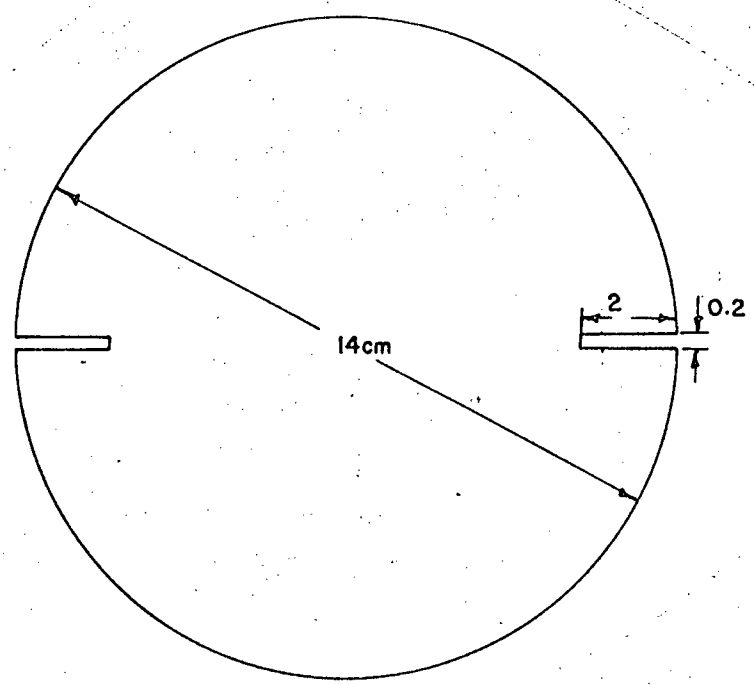

Fig. 21 Two Slit Chopper

end of the magnet and the entrance to the ionizer. The motor and reference signal circuit used are identical to those described in chapter 5 for the time-of-flight velocity measuring apparatus. The chopper used in the ion yield measurement was essentially the same as that shown in Fig. 21 except that the two slots have been widened to 0.8 cm and lengthened to 4 cm. The electronics used in making the ion beam current measurement employing the chopper system is shown in Fig. 20B.

The ionization efficiency of the ionizer for hydrogen gas was determined by slowly raising the background pressure in the ionizer chamber and measuring the resulting ion yield. The results are shown in Fig. 22. The pressure measurements were made with a Bayard-Alpert type ionization gauge and were increased by a factor of 2.2 to allow for the relative sensitivity of the gauge to hydrogen and nitrogen, the gas for which the gauge is calibrated. The operating conditions of the ionizer during this measurement are summarized below.

Plate and grid voltage	260 V
Plate + grid current	600 mA

The resulting ionization efficiency of the ionizer for hydrogen gas at room temperature is 6.5 A/Torr. This yield shown as a dashed line on Fig. 22 compares favourably with the 6 A/Torr reported by Glavish (Gl68) of Auckland University for a strong field axial ionizer. The University of British Columbia ionizer has an ionization volume of 4.2 cm^3 while the Auckland ionizer has an effective volume of 3.5 cm^3. These volumes are relevant in comparing ionization yields of the

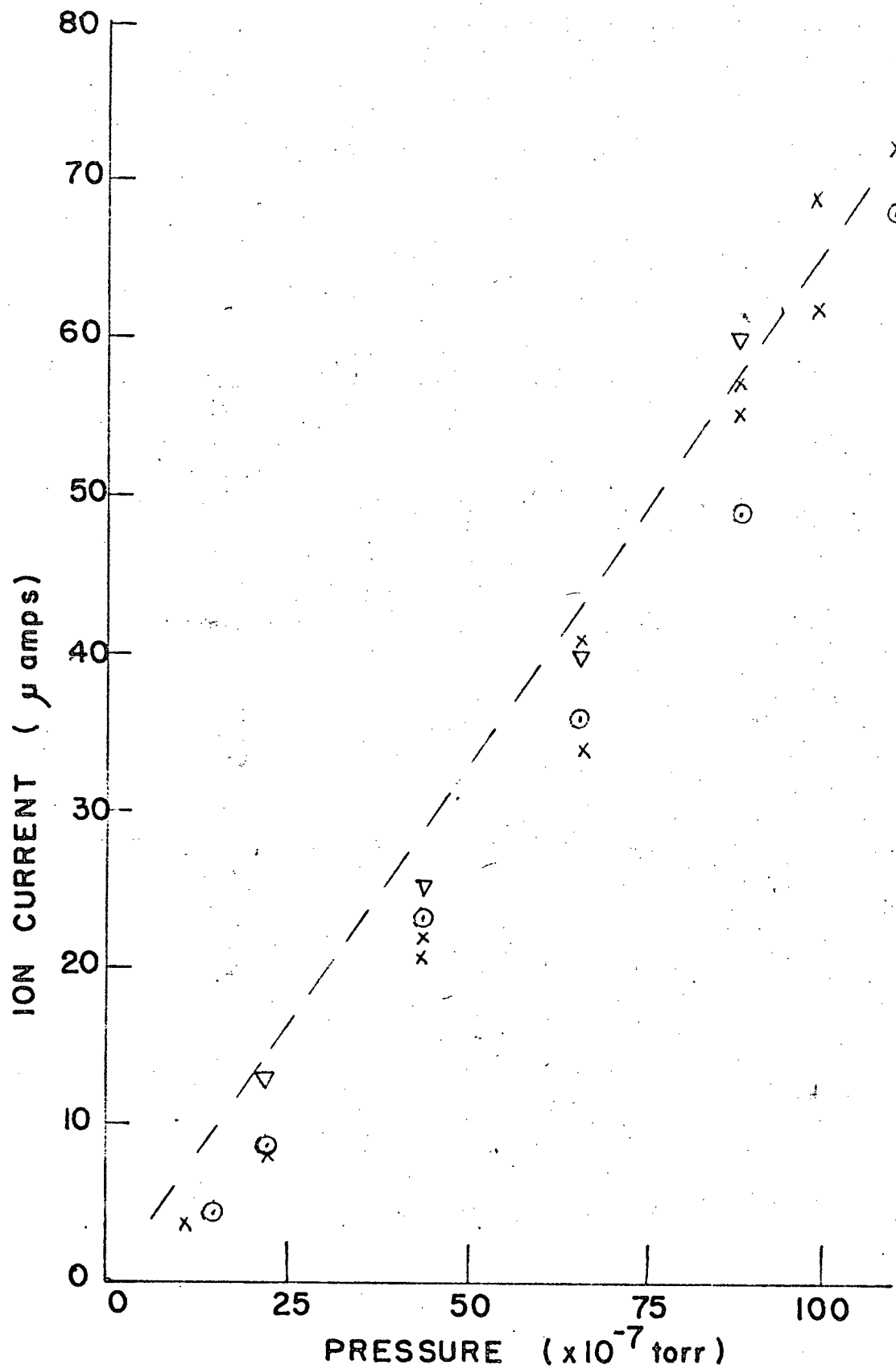

Fig. 22 Ionizer Ion Yield as a Function of Background Hydrogen Gas Pressure.

background gas but are not the relevant volume when considering actual beam ionization efficiencies. The latter efficiency depends more on the active volume through which the atomic beam passes. The length of the ionization zone, 14 cm for the Auckland ionizer and 12 cm for the U.B.C. ionizer, gives a better indication of the ionizing ability. On the surface, the two ionizers appear roughly comparable but the Auckland ionizer is much superior in at least two respects, first it is a strong field rather then weak field ionizer thus allowing substantially higher polarization values and second its axial design results in beam emittances much superior to the side extraction ionizer.

CHAPTER V

TECHNIQUES FOR MEASUREMENT OF ATOMIC BEAM INTENSITY AND VELOCITY

A. Measurement of Atomic Beam Intensity.

Measurements of atomic beam intensity were achieved using a differential Pirani detector. This detector, described by Jassby (Ja64), has a sensitivity of $1.0 \pm 0.1 \times 10^{15}$ atoms/sr - sec - μvolt signal measured with a ^{4}He oven source beam. Jassby shows that the relative sensitivity S of the detector for ^{4}He and ^{3}He depends on the ratio of specific heats C_v and accomodation coefficients α of the two gases according to the following relation

$$\frac{S_{^4He}}{S_{^3He}} = \frac{C_{v\,^4He}\ \alpha_{^4He}}{C_{v\,^3He}\ \alpha_{^3He}} \qquad (21)$$

At room temperature the specific heats of the two gases are identical; thus the ratio reduces to

$$\frac{S_{^4He}}{S_{^3He}} = \frac{\alpha_{^4He}}{\alpha_{^3He}} \qquad (22)$$

Thomas, Krueger and Harris (Th69) give an experimental value for the ratio $\alpha_{^4He} / \alpha_{^3He}$ of accomodation coefficients on clean tungsten at 308°K as $1.088 \pm .029$. It is unlikely that the tungsten filaments used in our detector operating at 560°K will be particularly clean; nevertheless this number indicates the approximate difference in sensitivity of the gauge for ^{3}He and ^{4}He that should be expected.

B. The Time-of-Flight Measuring Apparatus.

The velocity of the atomic beam was measured using a time-of-flight system. Fig. 23 shows the main components of this system.

The chopper used in this system is shown in Fig. 21 and consists of a 14 cm diameter disk 0.8 mm thick with 2 slots each 2 mm wide and 2 cm long. The reversible motor located inside the vacuum chamber is capable of revolving the disk at 30,000 rpm. A trigger reference signal is provided by the phototransistor in the circuit shown in Fig. 24. The length of the flight path from the chopper to the center of the ionization gauge 2.5 cm in diameter and 2.5 cm long was 57.4 cm. The low frequency electronic noise on the signal was removed by the high pass filter shown in Fig. 25. The high frequency signal was displayed on a Tektronix 564 oscilliscope screen. The reference signal from the phototransistor was used to trigger the oscilliscope; the time separation of the trigger and signal pulse was measured with the chopper rotating in both clockwise and counterclockwise directions. Measurements in both directions were required to eliminate errors due to inaccurate mechanical alignment which resulted in the phototransistor being triggered slightly before or after the atomic beam was chopped. The average of the two times and the measured flight path are then used to calculate the most probable velocity of the beam.

In Appendix D the shape of the time-of-flight signal S(t) is shown to be related to the differential intensity distribution function I(v) for the case of an infinitely short

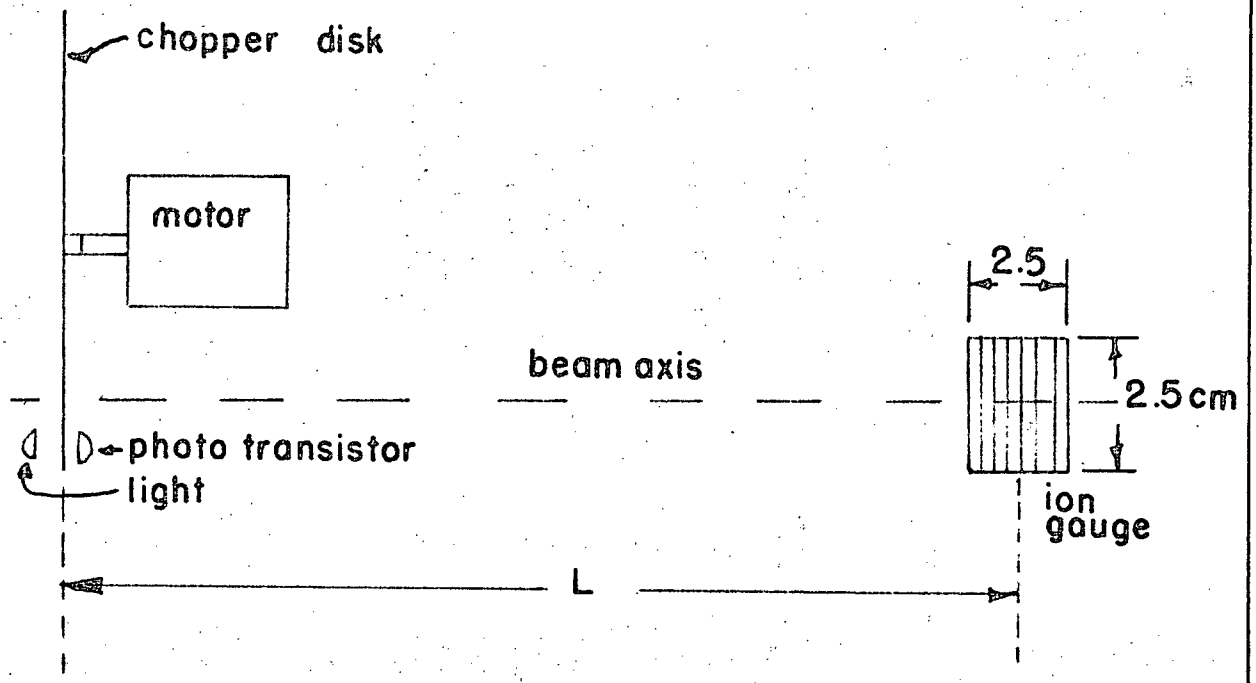

Fig. 23 Schematic Representation of Time-of-Flight Velocity Measurement Equipment.

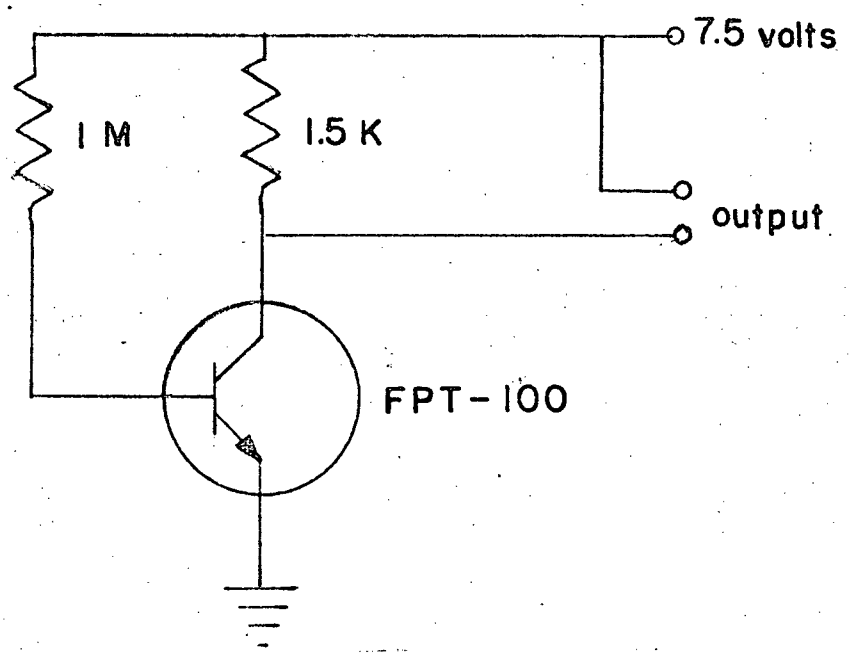

Fig. 24 Phototransistor Reference Signal Circuit.

shutter function and detector length by the relationship

$$S(t) = \text{constant} \quad \frac{1}{V} \quad I(V) \tag{D1}$$

where $V = \frac{L}{t}$

For a given I(v) the full width at half maximum FWHM of the signal S(t) is used to obtain the Mach number M of the beam.

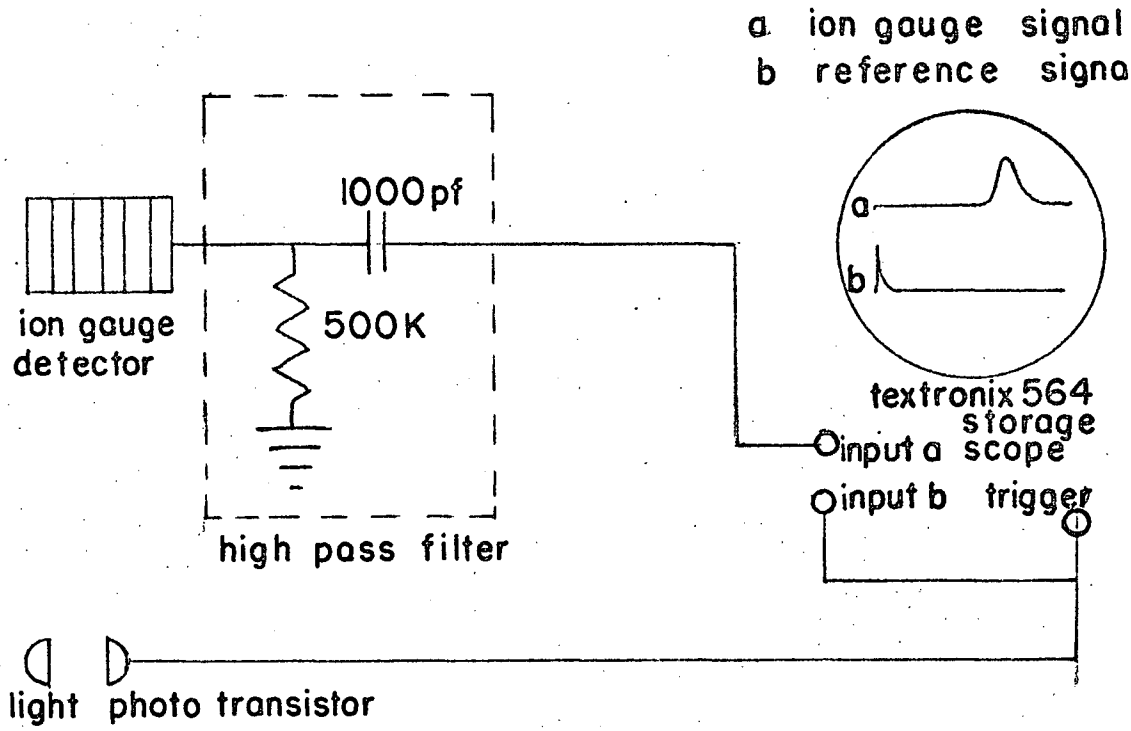

Fig. 25 Schematic of Ion Gauge Signal Circuit, Reference Signal and Oscilliscope Display.

The effect a finite width rectangular shutter function and detector length has on the signal shape S(t) are also considered in Appendix D. The relationship between the FWHM Δt_o of the signal S(t) with an infinitely thin shutter function and the FWHM Δt for a rectangular shutter function of finite width T is shown in Fig. 26. The calculation of Δt

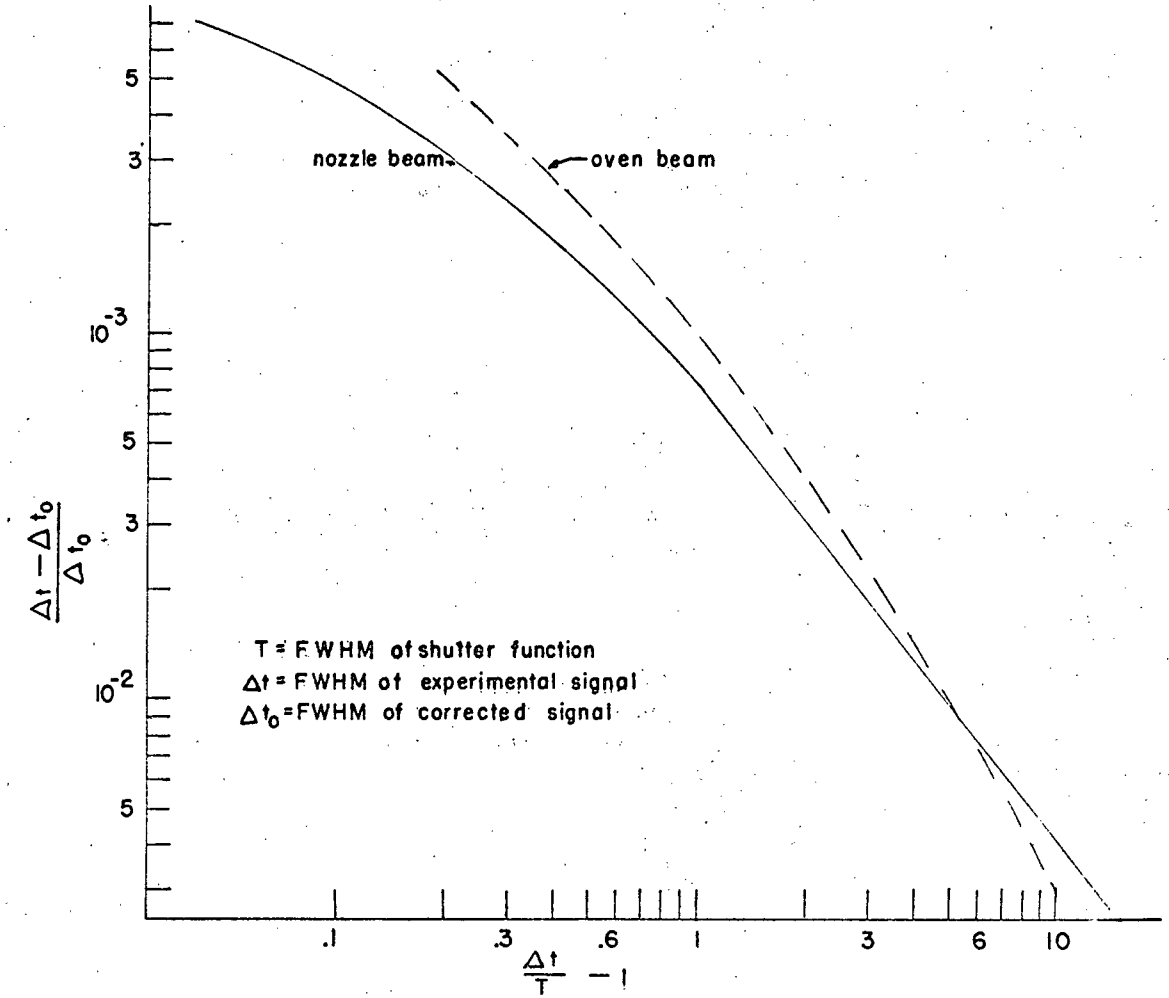

Fig. 26 Broadening of Experimental Signal due to Finite Width Shutter Function. Nozzle Beam Curve Includes Correction for a 2.5 cm Detector Length.

was done for a detector length of 2.54 cm. Thus with the aid of Fig. 26 the FWHM of the experimental signal Δt was related to the theoretical signal Δt_o and hence to a Mach number M of the differential intensity distribution function I(v). Also shown on this figure are some similar results obtained by Becker and Henkes (Be56b) for a differential intensity distribution function arising from an oven beam with a Maxwellian velocity distribution. In the calculation given in Appendix D the shutter function is assumed rectangular. Although the real shutter function is considerably more complicated, the consequence of the approximations resulting in the assumption of a rectangular shutter function are shown to be small. With the time of flight geometry shown in Fig. 23 the intensity distribution as a function of time of a group of particles passing through the chopper slit depends mainly on the intensity profile of the atomic beam at the chopper and the solid angle subtended by the ion gauge. The speed of rotation of the chopper, the chopper slit width and other geometrical parameters are also considered in determining the real shutter function.

From the geometry of the experimental arrangement only particles eminating from the nozzle within a cone subtended by the extremities of the ion gauge detector enter the detector. Hence, at the chopper location, the beam has at most an effective diameter of 5.3 mm. As is shown in Fig. 38 the actual measured beam profile at the chopper location had a FWHM of 7 mm. The intensity in the centre 5.3 mm wide strip varied about $\pm$ 15% from the average of its value at the side

of this region and the peak value at the centre. Thus the beam intensity profile can be assumed to be rectangular. This assumption implies that the beam cross section is not circular but is in fact square. Hagena, Scott, and Varma (Ha67b) have shown for the case of a shutter width equal to the width of the beam that this approximation had little effect on the shape of the shutter function. With these assumptions and an average tangential chopper velocity of 35 m/sec, corresponding to our experimental conditions, the calculated intensity distribution of particles passing through the chopper as a function of time is shown in Fig. 27.

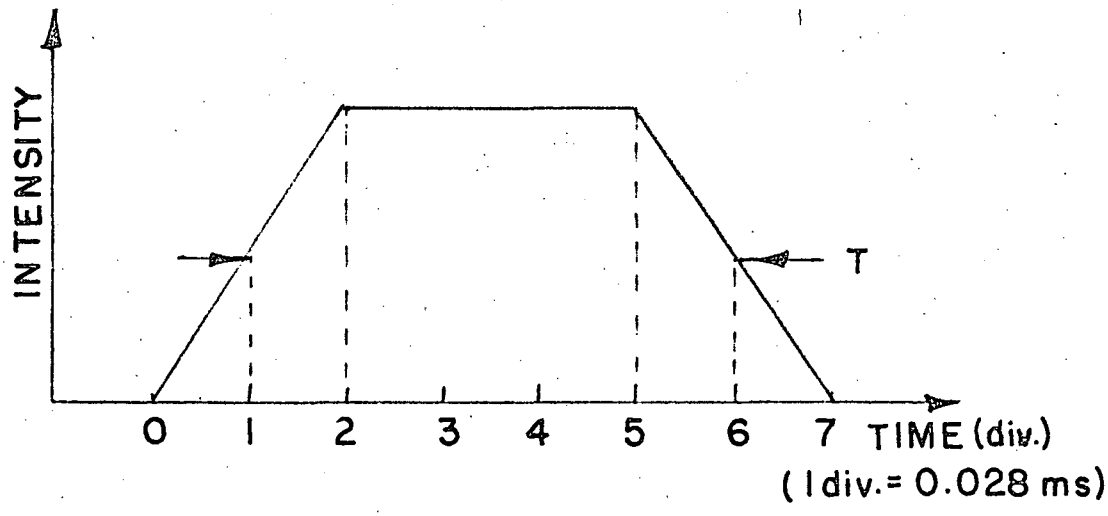

Fig. 27 Assumed Intensity Profile of Particles Passing through the Chopper Opening (Shutter Function). Trangential Chopper Velocity = 35 m/sec.

To apply properly the results of Appendix D this intensity distribution must also be assumed approximately rectangular in shape. As will be described in section 6B, the correction to the experimental signal as a result of the finite chopper width is sufficiently small, less than 5%, that the

approximations made in deriving the correction formula do not produce any significant errors.

CHAPTER VI

RESULTS OF STUDIES OF THE ATOMIC BEAM

A. The Atomic Beam Intensity.

The atomic beam source previously described has been tested under many varying conditions. Parameters such as the nozzle diameter d, skimmer diameter, nozzle-skimmer separation Xs, stagnation pressure p_o and stagnation temperature T_o have been varied and the resulting beam intensity I measured. Typical data are presented for 0.2 mm and 0.025 mm diameter nozzles.

Beam intensities for a 0.2 mm diameter nozzle as a function of nozzle pressure for particular nozzle-skimmer separations and the nozzle at room temperature are shown in Fig. 28. The skimmer and collimator were 0.6 mm and 1 mm in diameter respectively while the skimmer-detector separation was 15 cm. The interpretation of these contours in the manner described in Chapter III is most clearly seen by considering cross sections obtained at fixed stagnation pressures and varying the nozzle-skimmer separation. Such a set of curves is presented in Fig. 29 for the room temperature data of Fig. 28. With the exception of one or two points the data points were fitted with a smooth curve. The difficulty in producing completely consistent data can be attributed to the lack of profiles at a sufficient number of nozzle-skimmer separations, the difficulty of keeping the detector alignment exactly the same between runs when the system was disassembled

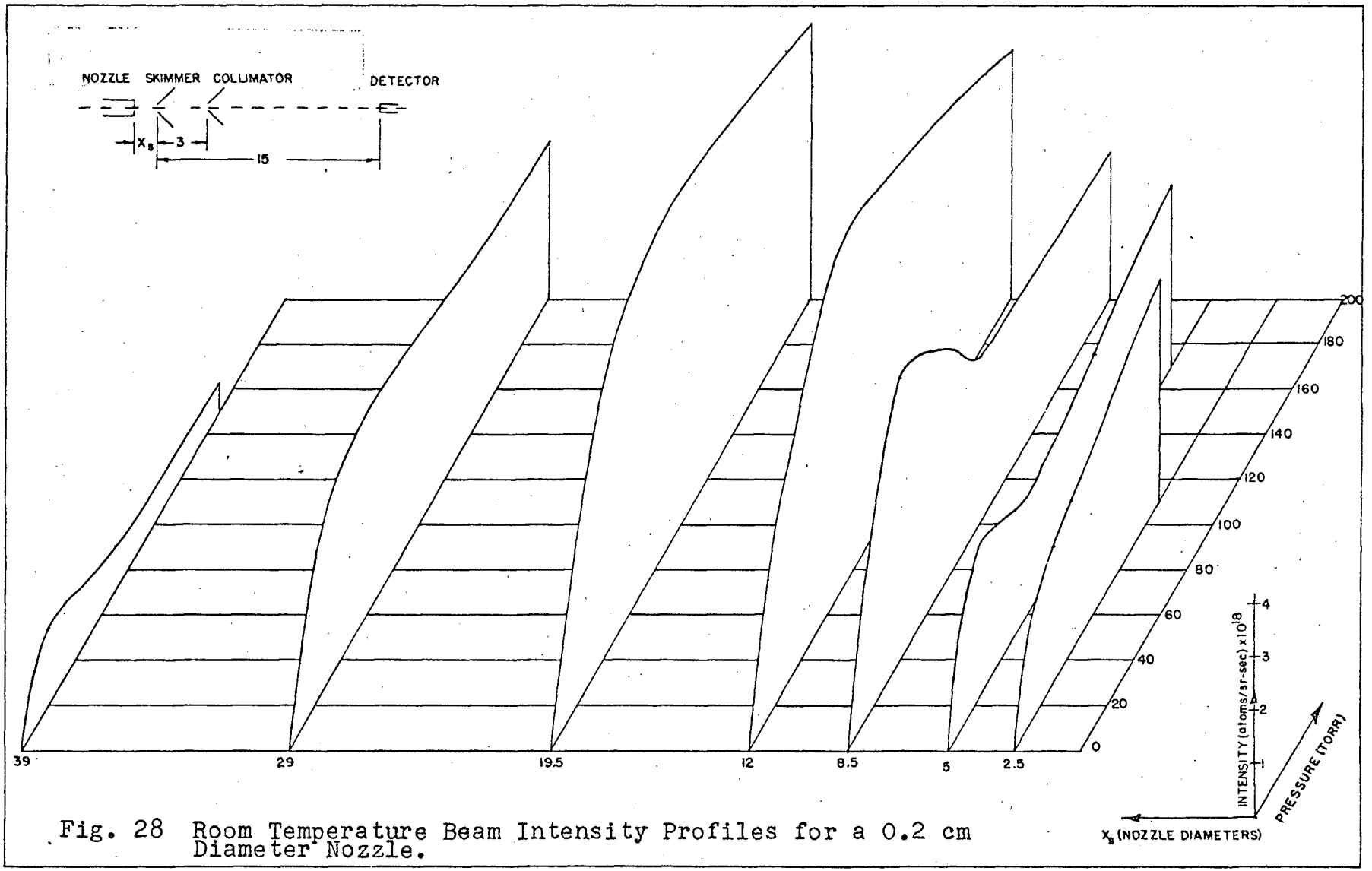

Fig. 28 Room Temperature Beam Intensity Profiles for a 0.2 cm Diameter Nozzle.

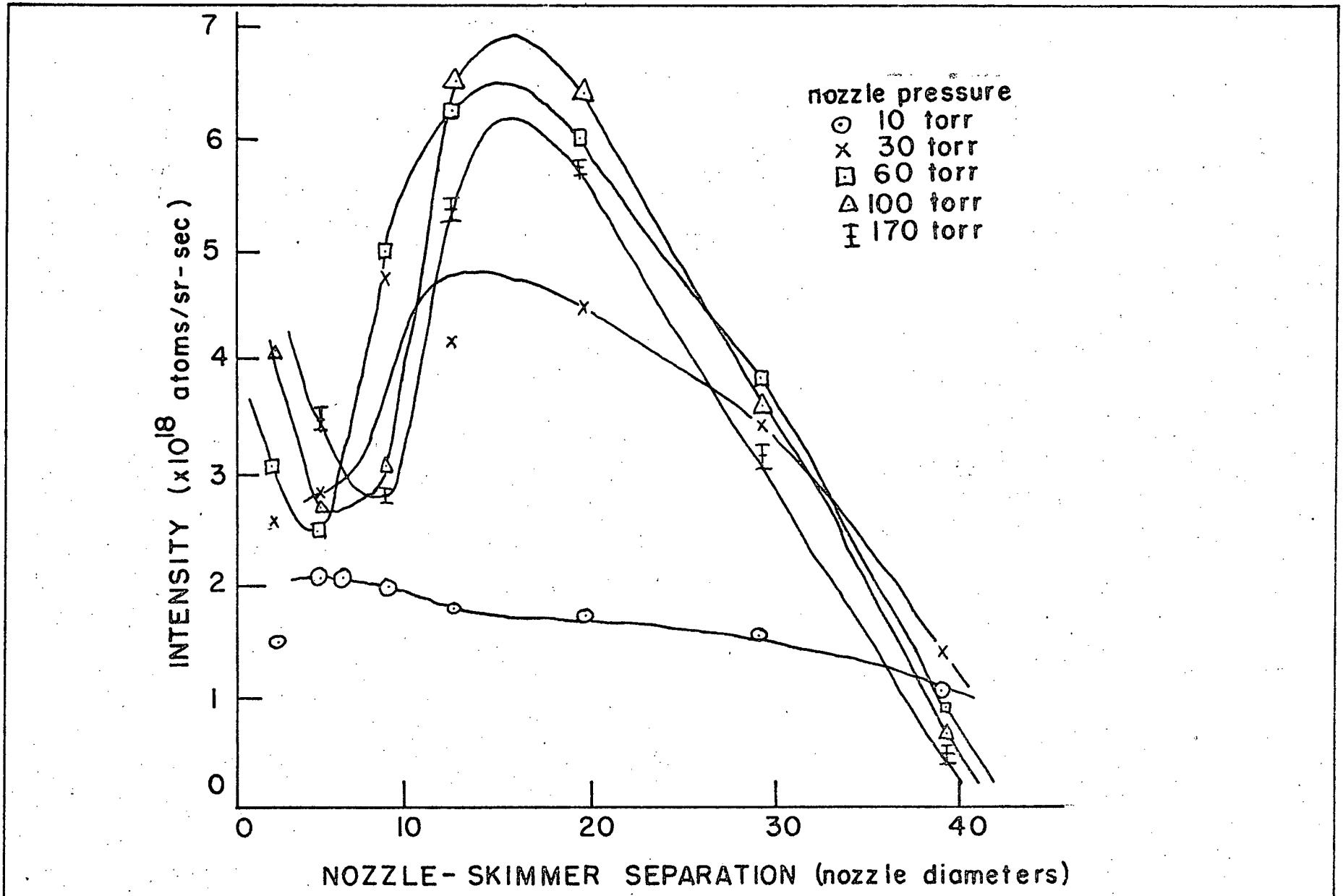

Fig. 29 Room Temperature Beam Intensity Profiles as a Function of Nozzle-Skimmer Separation.

and reassembled to vary the nozzle-skimmer separation, and the accidentally enforced use of a different nozzle for the measurements at a separation of 5 nozzle diameters. The room temperature data shown in Fig. 30 was obtained with the adjustable nozzle-skimmer apparatus. The physical alignment of the detector remained fixed throughout the measurement and the nozzle-skimmer separation was adjusted from outside the vacuum system. The large number of data points can be fitted with very smooth curves. Although the nozzle and skimmer used in obtaining the data of Fig. 30 were approximately the same diameter as those used in obtaining the data of Fig. 29, they are not the same nozzle and skimmer. This accounts for the differences in absolute intensities and nozzle-skimmer separations reported for the peaks and valleys, however, the general shape of the profiles remains the same.

The results shown in these two figures illustrate the typical dependence of beam intensity on nozzle-skimmer separation obtained with supersonic nozzle systems, namely, the large beam intensity at very short nozzle-skimmer separations followed by a reduction in intensity to a minimum followed by a further increase in intensity to a maximum and subsequent attenuation. This behaviour is due to the effects described in Chapter III. For very small nozzle-skimmer separations the beam passes through the skimmer with no interaction and then expands as a free jet downstream of the skimmer. As the separation is increased the beam is influenced by the skimmer and eventually the "skimmer interaction" described previously takes its maximum effect. Further separation of the nozzle and skimmer

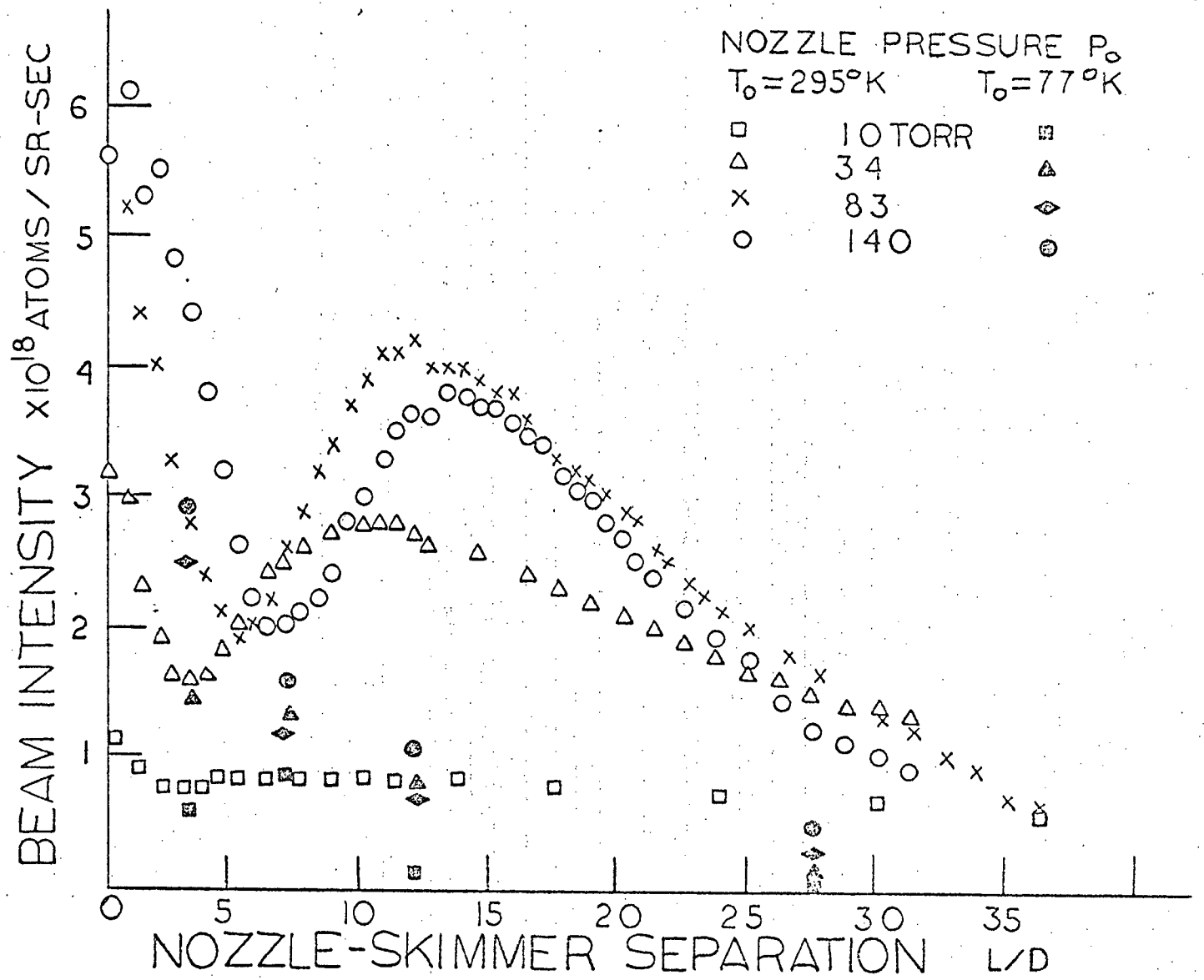

Fig. 30 Continuous Beam Profile Taken with Adjustable Nozzle-Skimmer Assembly.

results in a reduction of the gas density at the skimmer entrance. Reduced gas density at the skimmer implies reduced skimmer interaction so that the beam intensity increases. As the separation gets even larger the skimmer becomes downstream of the Mach disk and background gas scattering becomes more and more significant, eventually overwhelming any increase in beam intensity due to reduced skimmer interaction.

The appearance of the 'maximum maximorum' described by Campargue (Ca66) is seen in both Figs. 29 and 30 where for increasing nozzle pressures the peak intensity grows slowly then reaches a maximum and thereafter falls off.

A similar treatment of the liquid nitrogen temperature data shown in Fig. 31 gives the profiles shown in Fig. 32. An examination of the data shows a behaviour similar to the room temperature data, though with much less prominent maxima, for a set of nozzle stagnation pressures considerably lower than in the room temperature case. This "compression of contours" is caused by the higher gas densities, hence much smaller mean free paths and greater scattering for a given nozzle pressure at the lower temperature. Also the higher gas densities at the skimmer increase the skimmer interaction. Another effect which starts to become evident at higher pressures and lower temperatures is beam formation from the skimmer or collimator openings. This effect causes increased beam intensity for increased stagnation pressures at large nozzle-skimmer separations. More will be said about this while discussing the liquid helium cooled beams in the next paragraph.

A similar plot of intensity as a function of nozzle-

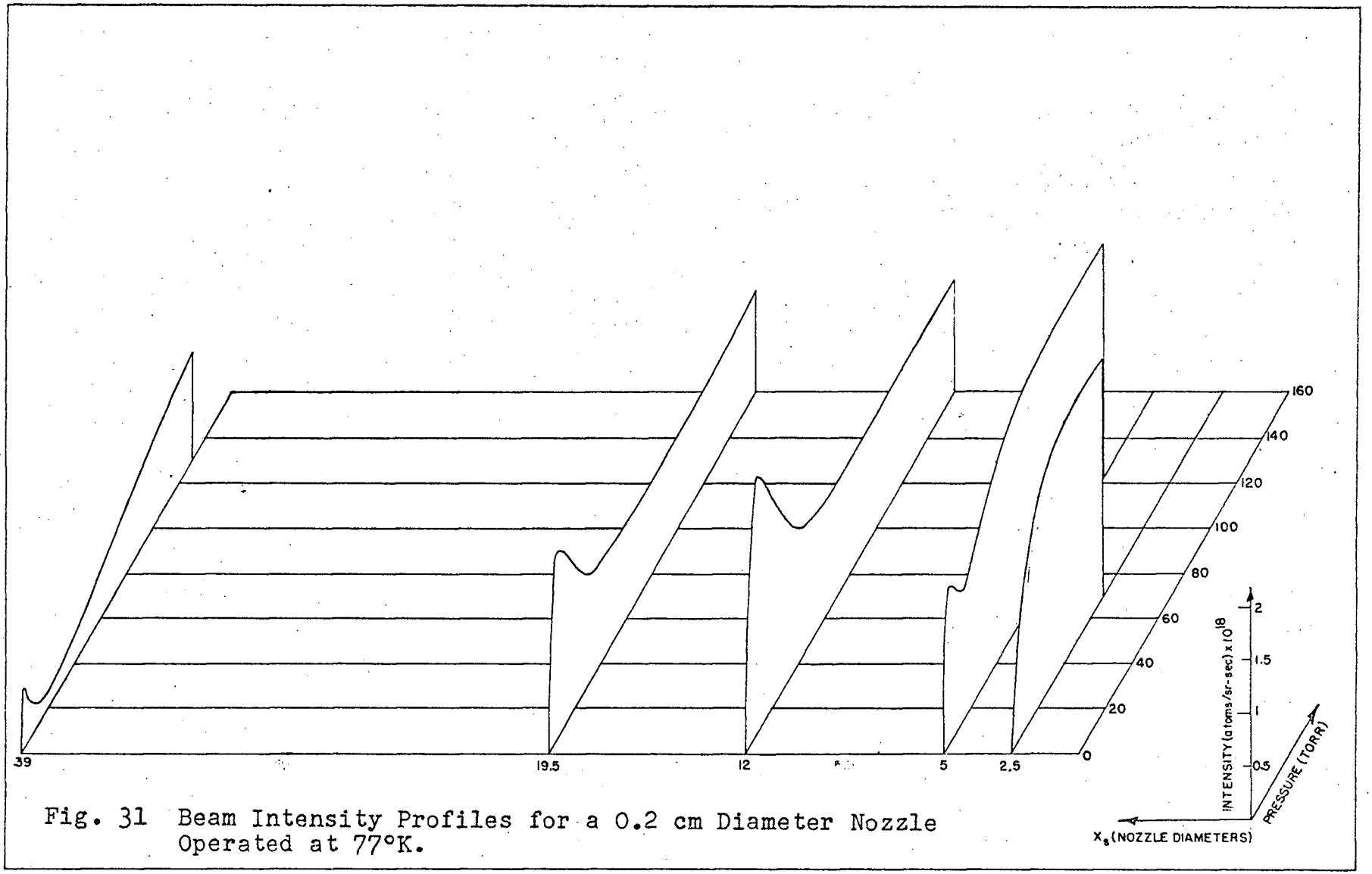

Fig. 31 Beam Intensity Profiles for a 0.2 cm Diameter Nozzle Operated at 77°K.

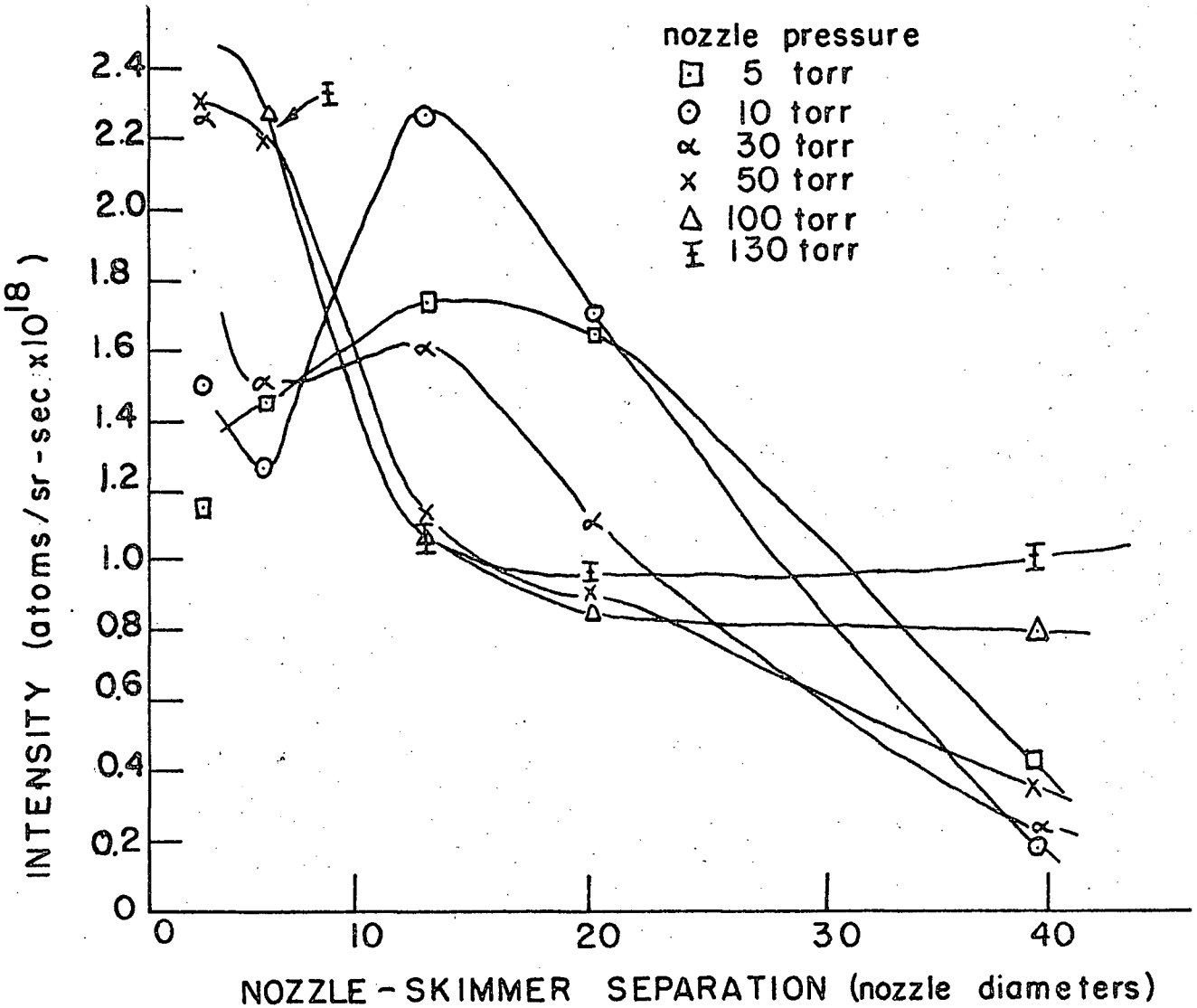

Fig. 32 Liquid Nitrogen Temperature Beam Intensity Profiles as a Function of Nozzle-Skimmer Separation.

skimmer separation using the nozzle stagnation pressure as a parameter is shown in Fig. 33 for the data displayed in Fig. 34. This data was obtained with the nozzle cooled to liquid helium temperature. The large scatter of points is due to the great compression of the peaks and valleys into a nozzle pressure range of only a few Torr and the dominant role played by the formation of subsidiary beams from the skimmer and collimator. With experimental results for so few nozzle-skimmer separations and because of the scatter of the observed points the consistent trends do not appear as in the data points obtained at higher nozzle temperatures. The gradual rise in intensity at large nozzle-skimmer separations is consistent with a reduction of the gas flow past the skimmer and hence a resulting reduction of pressure in the skimmer-collimator region and downstream of the collimator. The improved background pressure results in improved transmission of subsidiary beams from the skimmer and collimator and the residual nozzle beam. The actual beam intensity versus nozzle pressure profiles measured at a fixed nozzle-skimmer separation are of considerably more interest in this case. For the profile at a separation of 19.5 nozzle diameters shown in Fig. 34 the beam intensity in the region up to the first maximum which occurs at a nozzle pressure of 1 Torr is attributed to a true nozzle beam. The reduction of beam intensity for higher nozzle pressures is attributed to the dominance of background gas scattering in the nozzle-skimmer region. The subsequent increase in beam intensity is caused by the combined effect of a small residual nozzle beam along

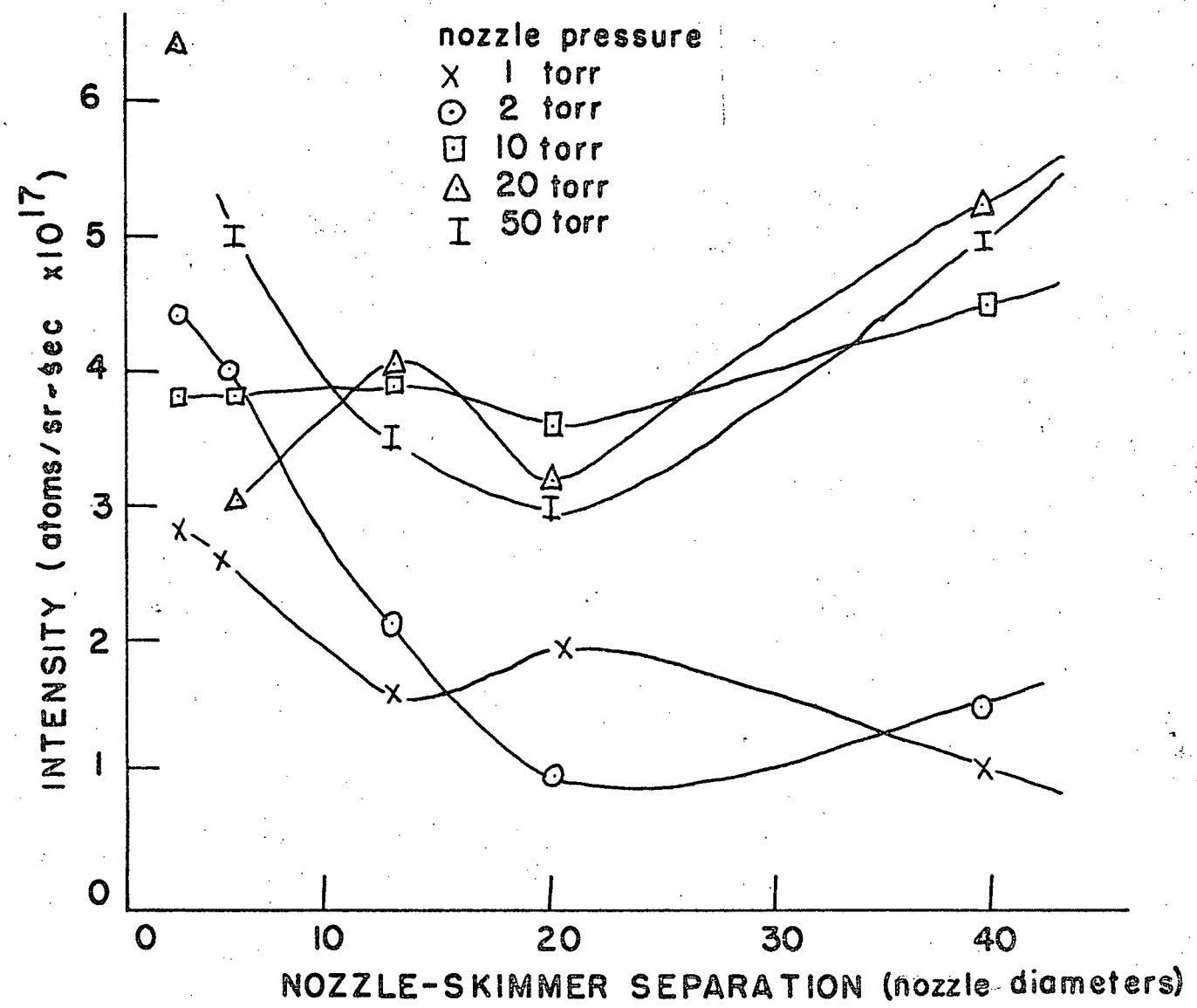

Fig. 33 Beam Intensity Profiles as a Function of Nozzle-Skimmer Separation with the Nozzle at Liquid Helium Temperature.

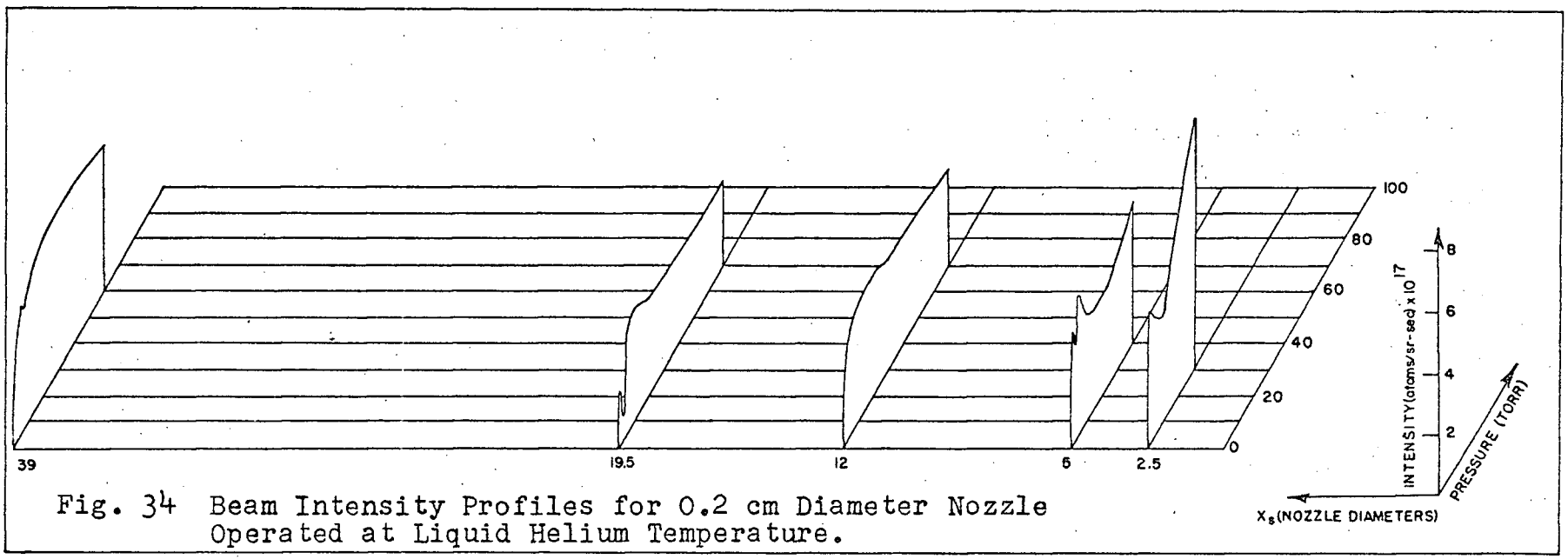

Fig. 34 Beam Intensity Profiles for 0.2 cm Diameter Nozzle Operated at Liquid Helium Temperature.

with a subsidiary beam from the skimmer and collimator openings. In data obtained with a smaller nozzle, described in the next paragraph, the pressure range over which the first peak occurs is expanded considerably and the actual behaviour of the nozzle beam is much easily determined. Comparison with theoretical predictions will be described in detail in that section.

Fig. 35 shows results obtained with a 0.025 mm diameter nozzle at room, liquid nitrogen, and liquid helium temperatures. A 0.57 mm diameter skimmer and a 1 mm diameter collimator were used for these measurements. The nozzle-skimmer separation was set at 0.28 cm and the skimmer detector distance at 16 cm. Fig. 36 shows in greater detail the results using both ^{3}He and ^{4}He beams with the nozzle cooled to liquid helium temperature. In both figures the deviation from a linear relation with pressure is due to background gas scattering in the nozzle-skimmer region. This can be checked by assuming the beam intensity I should be linearly proportional to the nozzle pressure p_o and the scattering pressure should be linearly proportional to p_o also. Fig. 37 shows a plot of $\log\left(\frac{I_o}{p_o}\right)$ vs p_o. The observed linear decrease of intensity with p_o is consistent with scattering of the beam according to $I = I_o e^{-\int n\sigma\, dl}$ (18) where I_o, the beam intensity with no scattering, and n, the gas density in the nozzle-skimmer region, are both assumed to be proportional to the nozzle pressure p_o, σ is the effective scattering cross section and l the distance along the beam axis. The difference in the slopes for ^{3}He and ^{4}He in Fig. 37 indicates that the effective scattering cross

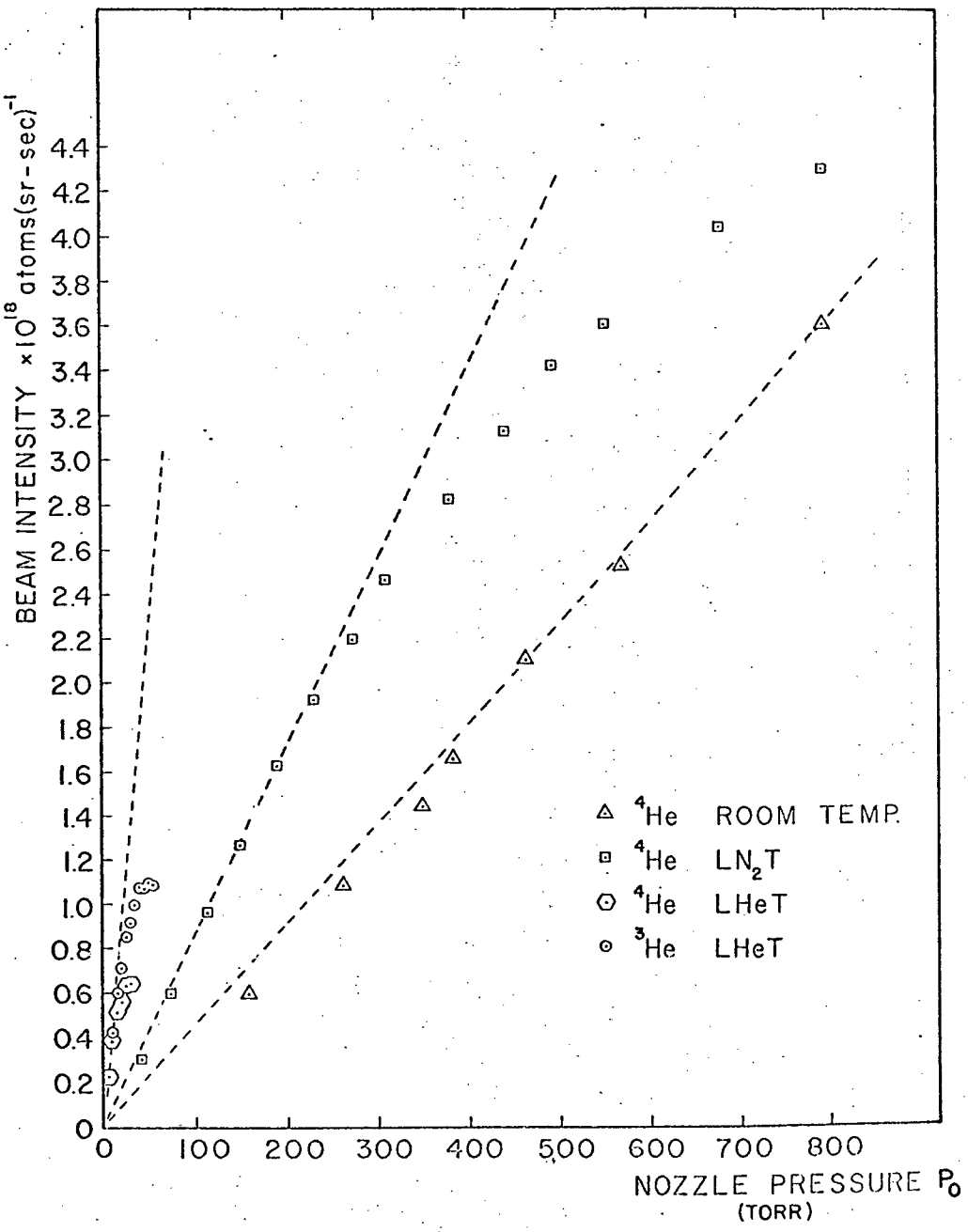

Fig. 35 ^{4}He Beam Intensities as a Function of Nozzle Stagnation Pressure Po for Three Temperatures To. The dashed lines passing through the origin are fits to the data after correction for scattering.

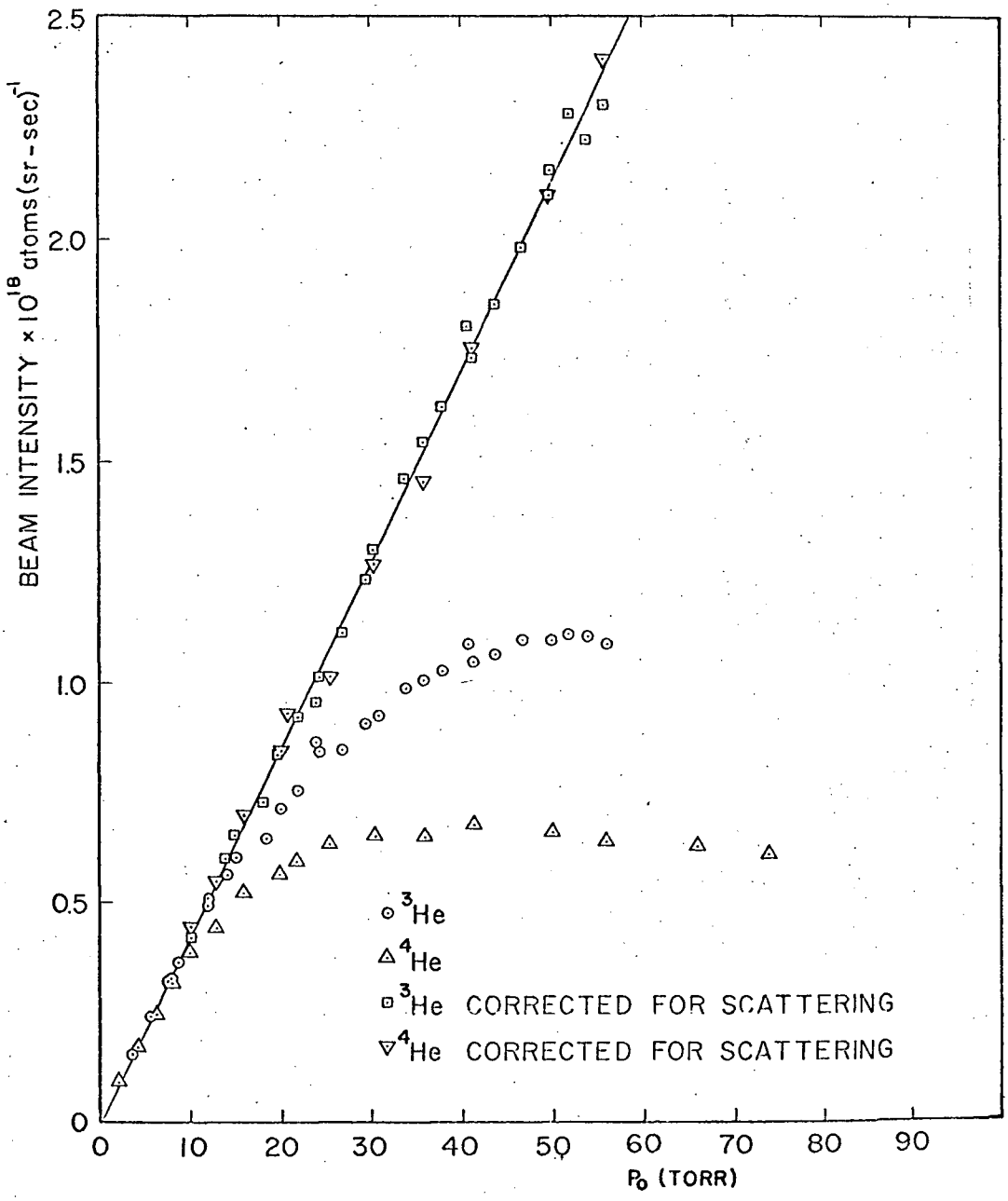

Fig. 36 Beam Intensities for ^3He and ^4He Beams at Liquid Helium Temperature Before and After Correction for Scattering. Only the uncorrected experimental points are shown when the correction is small.

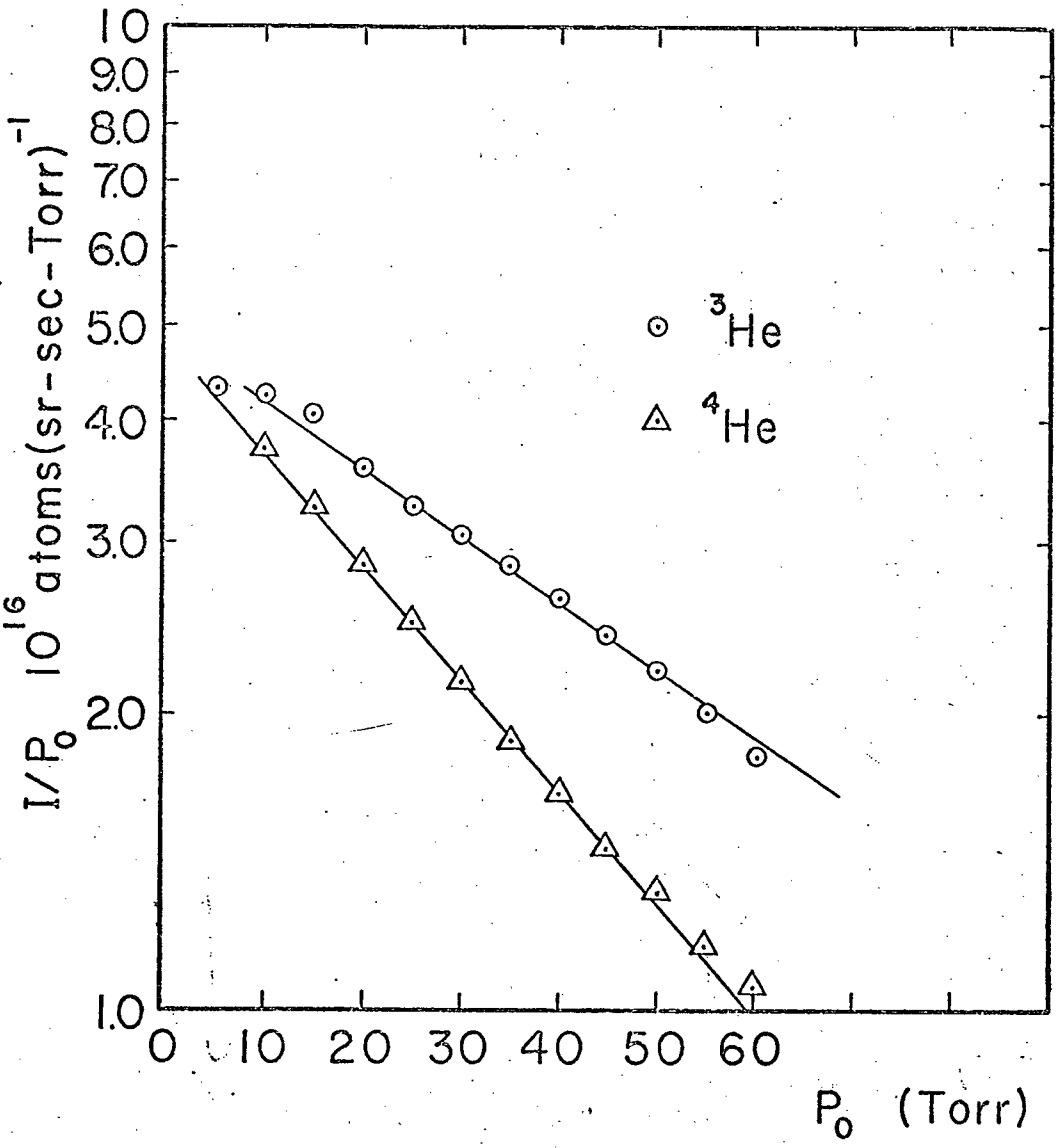

Fig. 37 The Uncorrected Data of Fig. 36 Divided by the Nozzle Pressure to Verify Existance of Scattering.

section for ^4He is 1.7 times larger than that of ^3He. Both experimental viscosity measurements and quantum mechanical calculations also indicate a larger cross section for ^4He. The difference in cross section is attributed to the different statistics followed by ^3He and the absence of a near stationary state in the $^3He_2$ system (Bo51).

The straight line in Fig. 36 was predicted using Eq. A5 assuming $T_o = 6.7°K$, $D = 0.025$ mm and a ^3He beam. The dashed lines shown in Fig. 35 are the ^4He data, similarly corrected for scattering at room, liquid nitrogen and liquid helium temperatures. The dashed lines are required to pass through the origin. The slopes of these lines are in the ratio 1 : 1.9 : 9.5. Eqs. 5 and A5 predict the intensity should be directly proportional to the nozzle stagnation pressure p_o and inversely proportional to the square root of the nozzle stagnation temperature T_o. The straight lines confirm the linear p_o dependence; their slopes would correspond to temperatures 295, 82 and 3.3°K. However, velocity measurements, discussed later, indicate temperatures of 295, 77 and 7°K so that the theoretical $T_o^{\frac{1}{2}}$ dependence would appear to break down at very low temperatures.

Eqs. 5 and A5 predict that the beam intensity should be inversely proportional to the square root of the atomic mass, so that the ^3He intensity should be a factor $\sqrt{\frac{4}{3}}$ larger than the ^4He intensity. The equality of the slopes for ^3He and ^4He in Fig. 36 is partially attributable to the 9% lower detector sensitivity expected for ^3He, as discussed

in Section 5A. There remains, however, a 6% discrepancy which could be due either to a still larger difference in sensitivity for ^3He and ^4He, or to an effect in the nozzle system not taken account of in the simple theory.

A ^4He beam vertical profile taken 16 cm from the skimmer is shown in Fig. 38. It has a full width at half maximum (FWHM) of 7 mm (2.5°) and a full width of 14 mm. The profile was taken with a nozzle stagnation temperature and pressure of 77°K and 420 Torr respectively.

Gas flow through the 0.025 mm diameter nozzle is estimated at 0.17 cc/sec (STP) for ^3He gas at p_o = 50 Torr and liquid helium temperatures.

B. The Beam Velocity.

A time-of-flight measuring apparatus was used to measure the most probable velocity and velocity distribution of ^3He and ^4He beams produced using the cryostat at room, liquid nitrogen and liquid helium temperatures. For ^4He at these temperatures the measured most probable velocities were 1660, 850 and 270 m/sec respectively, using the 0.025 mm diameter nozzle and the time-of-flight geometry discussed in section 5B. Using the form of the differential intensity distribution given by Eq. 17, fits to the most probable velocity determined the temperature of the nozzle to be 295, 77 and 7°K while still allowing a wide range of Mach numbers. At liquid helium temperatures the ^3He beam had a measured most probable velocity of 310 meters/sec. The ^3He and ^4He

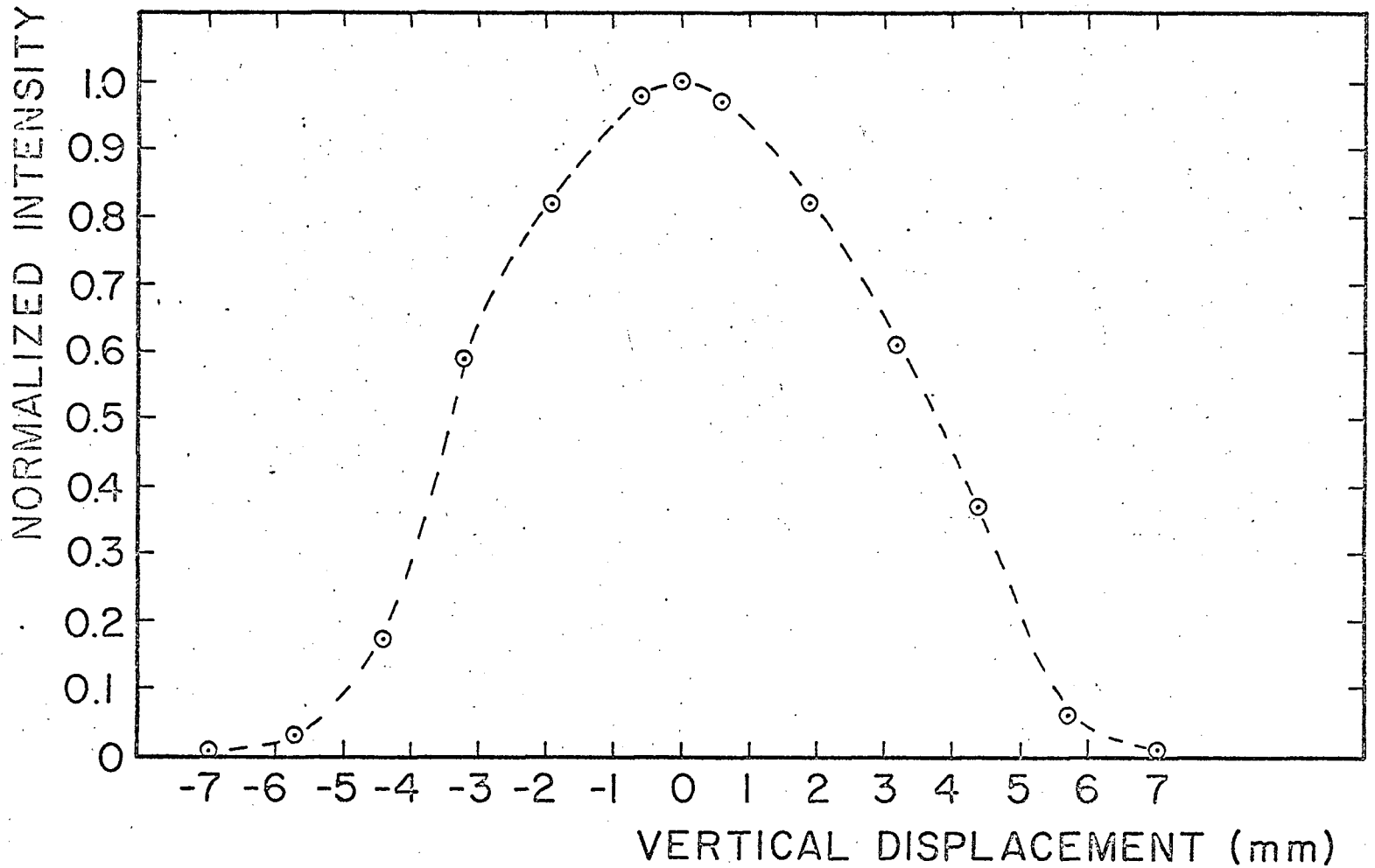

Fig. 38 Normalized Intensity Profile vs. Vertical Displacement from Beam Axis.
Stagnation Pressure Po = 420 Torr
Stagnation Temperature To = 77°K

velocities should differ only be a factor proportional to the square root of their masses eg. $\sqrt{\frac{m_{^3He}}{m_{^4He}}} = \sqrt{\frac{3}{4}} = 0.865$. Experimentally a ratio of 270/310 = 0.87 was obtained in good agreement with the expected dependence.

The difference between 7°K and 4.2°K, the temperature of the liquid helium, is attributed to poor thermal contact between the nozzle and the cryostat and a thermal gradient due to the heat leak to the nozzle assembly. A temperature of 7°K is consistent with carbon resistor measurements of the nozzle temperature which indicated a temperature on the outside of the nozzle of 8.5°K. The measurement of the temperature using a carbon resistor is discussed in Section 4A3.

A typical ^3He time-of-flight spectrum obtained with a chopper speed of 11,000 rpm is shown in Fig. 39. In this measurement the nozzle temperature was reduced slightly by pumping on the helium reservoir. A velocity spectrum derived from the time spectrum is shown in Fig. 40. The experimental signal with a FWHM of 53 m/sec is fitted quite well by the dashed theoretical curve obtained from Eq. 17 with the same FWHM and most probable velocity using a stagnation temperature T_o = 5.9°K and a Mach number M = 10. The chopper distribution function shown in Fig. 27 has a FWHM T = 0.143 ms and the FWHM of the experimental signal is Δt = 0.37 ms; thus the resolution $R = \frac{\Delta t}{T} = 2.6$. From Fig. 26 this corresponds to a broadening of $\frac{\Delta t - \Delta t_o}{\Delta t_o} = 4\%$ where Δt_o is the width of the ideal distribution which would have been obtained had the shutter slit and the detector width been infinitely thin. The

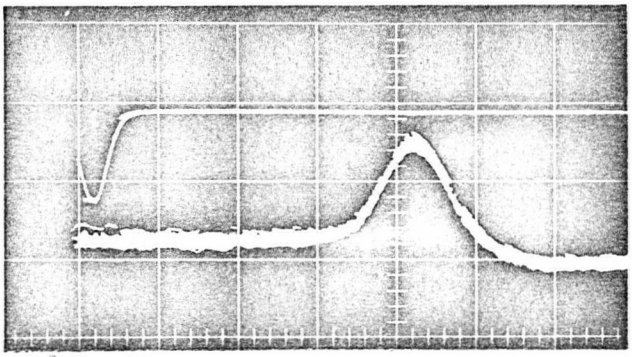

Fig. 39 Typical ^3He Time-of-Flight Spectrum for Liquid Helium Cooled Nozzle. Stagnation Pressure is 36 Torr. Horizontal Time Scale is 0.5 m sec/div. The Upper Trace shows the Time Reference Light Pulse.

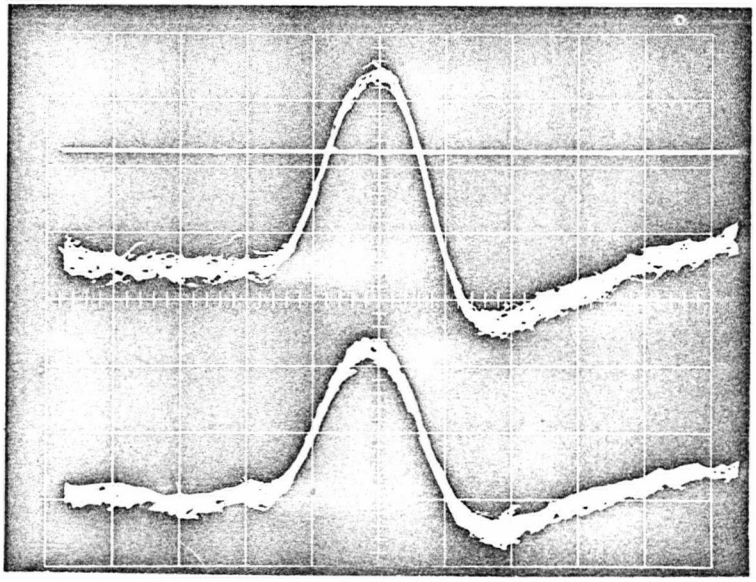

Fig. 46 Typical Ionizer Signals from Chopped Atomic Beam with Hexapole Magnet Turned On and Off.
Horizontal Scale 0.5 ms/div.
Vertical Scale 0.5 mv/div.

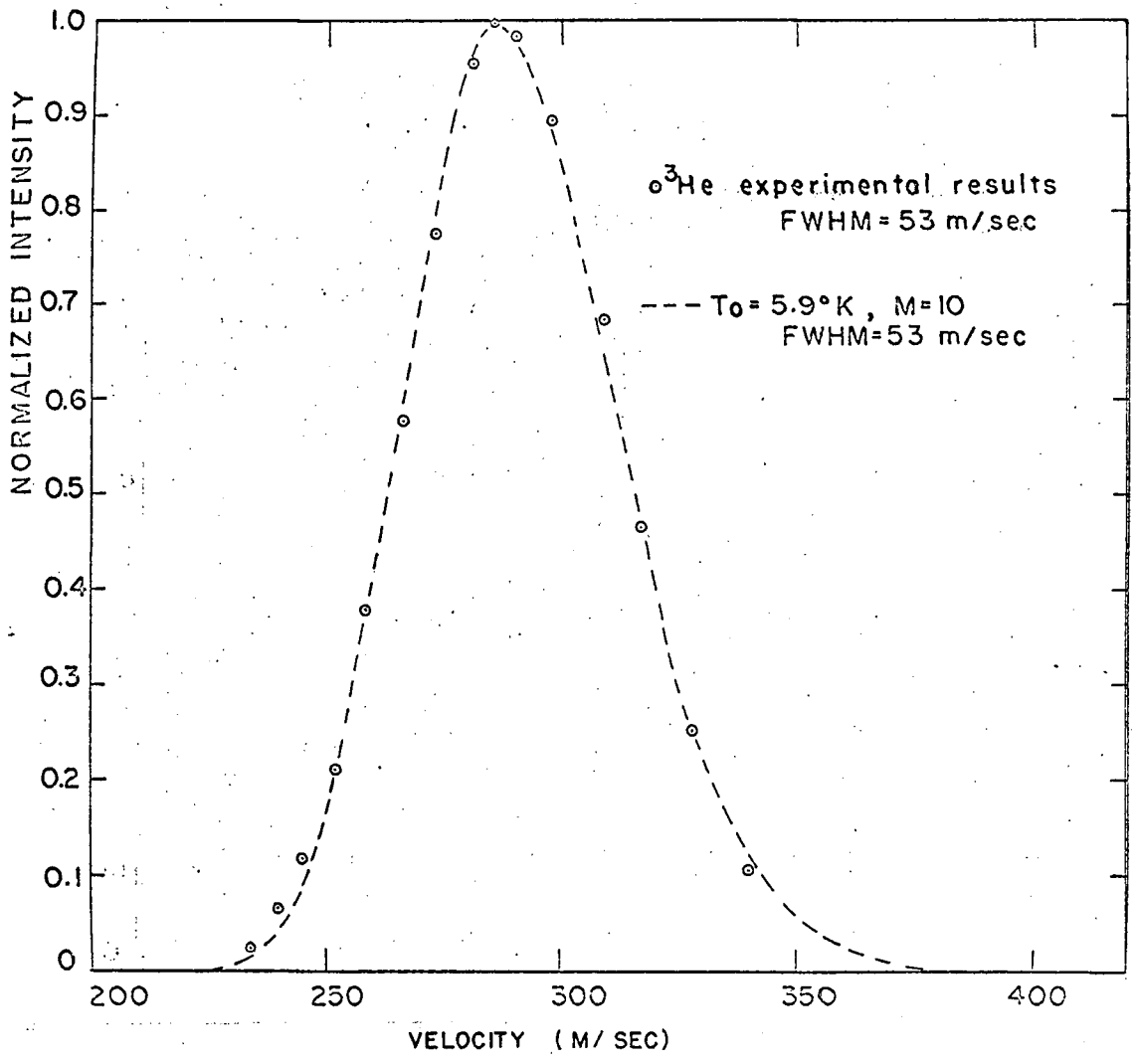

Fig. 40 Results of Fig. 39 Converted into a Velocity Spectrum. The curve shown is a fit of Eq. 17 to the experimental spectrum.

approximations made here should not significantly increase this value of 4%. Because of the small size of the resulting correction it will be neglected.

The experimental results shown in Fig. 40 were obtained with a nozzle stagnation pressure of 36 Torr. For this pressure and a stagnation temperature of 5.9°K the corresponding nozzle stagnation Knudsen number is 1.8×10^{-3}. Using Eq. 13 the terminal Mach number is calculated to be 15 while the experimental data shown in Fig. 8 indicates that for ^{4}He at this Knudsen number the terminal Mach number would be 12. This is in good agreement with the experimental determination of M = 10 considering that the real width of the measured distribution is actually slightly narrower and as a result the Mach number will be slightly higher.

It should be noted that no indication of a condensed fraction of the beam was observed in the velocity measurements. That is, no second peak at a lower velocity corresponding to a condensed fraction of the beam appeared in the time-of-flight spectrum. The appearance of a second peak has been described by Becker, Bier and Henkes (Be56) as being typical of condensed beam formation. The good agreement between the measured and expected polarization of the ^{3}He beam (as will be mentioned later) is confirmation that at most a very small fraction of the beam was condensed.

CHAPTER VII

POLARIZATION AND IONIZATION OF THE ^{3}He BEAM

A. The Trajectories of Atoms through the Hexapole Magnet.

The development of the equations describing the trajectories of particles through the hexapole magnet has been described by Axen (Ax65) and is summarized in Appendix C. The position and slope of a focussed particle in the tapered section of the magnet is given by Eqs. C32 and C34 as a function of the radial position of the particle at the magnet entrance. The radial position and divergence of the defocussed particle is given by Eqs. C36 and C37. The position and slope of the particles in the parallel section of the magnet were calculated using Eqs. C25 and C26 in the case of the focussed particle and Eq. C27 in the case of the defocussed particle. The initial position and slope of the particle as it enters the parallel section is determined from the solution of the trajectories at the end of the tapered sections.

The hexapole magnet was designed for a beam with a most probable velocity of 175 meters/sec. As has been discussed in the preceeding section the beam produced had a considerably higher velocity. The calculations of the position and slopes of particles at certain locations in the magnet for varying radial deflections at the magnet entrance and varying separation of the magnet from the nozzle source are summarized in Table 2. In these calculations the field H_o at the pole tips of the magnet was 9000 gauss. Typical trajectories of the

Table 2

Selected Trajectories of Focussed and Defocussed ^3He Atoms Passing Through the Tapered Hexapole Magnet

FOCUSSED TRAJECTORIES
R = radial deflection
S = slope

Particle Velocity (m/sec)	Radial Deflection at entrance to magnet (cm)	SOURCE-MAGNET SEPARATION 5 cm At End of Taper	5 cm At End of Magnet	15 cm At End of Taper	15 cm At End of Magnet	16 cm At End of Taper	16 cm At End of Magnet
245	0.025	R=0.0914	0.1717	R=0.044	0.055	0.0425	0.0523
		S=0.0039	0.0003	S=0.00095	-0.0004	0.0009	-0.0004
	0.05	0.1828	0.3433	0.087	0.109	0.0847	0.1016
		0.0078	0.0007	0.0019	-0.0007	0.0017	-0.0008
	0.075			0.13	0.1644	0.1274	0.1539
				0.0029.	-0.0011	0.0026	-0.0012
	0.1			0.17	0.215	0.1698	0.2061
				0.0038	-0.0014	0.0035	-0.0016
	0.125			0.22		0.212	0.255
				0.0047			
310	0.025	0.0946	0.2070	0.046	0.072	0.0447	0.0681
		0.0043	0.0018	0.0012	0.0002	0.0011	0.0002
	0.05	0.1892	0.4141	0.092	0.1445	0.0893	0.1316
		0.0086	0.0037	0.0024	0.0005	0.0022	0.0004
	0.075			0.138	0.2168	0.1340	0.2074
				0.0036	0.0007	0.0034	0.0006
	0.1			0.185	0.29	0.1787	0.2756
				0.00486	0.001	0.0045	0.0008
DEFOCUSSED TRAJECTORIES							
245	0.025		R=0.91		R=0.18		0.16
	0.05				0.36		0.33
	0.075				0.54		0.50
310	0.025		0.79		0.15		0.14
	0.05				0.30		0.28
	0.075				0.45		0.42

focussed and defocussed atoms for the case of a nozzle-magnet separation of 16 cm are shown in Fig. 41. As can be seen, the magnet proves incapable of bringing particles to a focus on the magnet axis if they have a velocity of 310 m/sec irrespective of the radial distance from the axis at which they enter the magnet except for a small number of particles very close to the magnet axis. The magnet does succeed however in keeping the trajectories of particles which enter the magnet less than 1 mm from the axis within the pole tips although the trajectories are still diverging when they leave the magnet. These trajectories should be a good approximation to the paths the ^{3}He atoms produced from the nozzle source will take through the actual magnet.

B. The Calculated Polarization of the Atomic Beam.

The relative numbers of focussed and defocussed particles passing through the hexapole magnet which subsequently pass through some specified ionization volume downstream of the magnet exit is needed in order to calculate the expected polarization of the beam. This information could in principle be obtained from the atomic trajectories presented in the previous section. This would involve calculating the trajectories for particles with many different velocities and initial conditions then deciding whether or not a given trajectory passes through the magnet and into the ionizer. Then the result would have to be appropriately weighted for the effect of the velocity distribution of the particles in the beam and the solid angle of particles of a given velocity

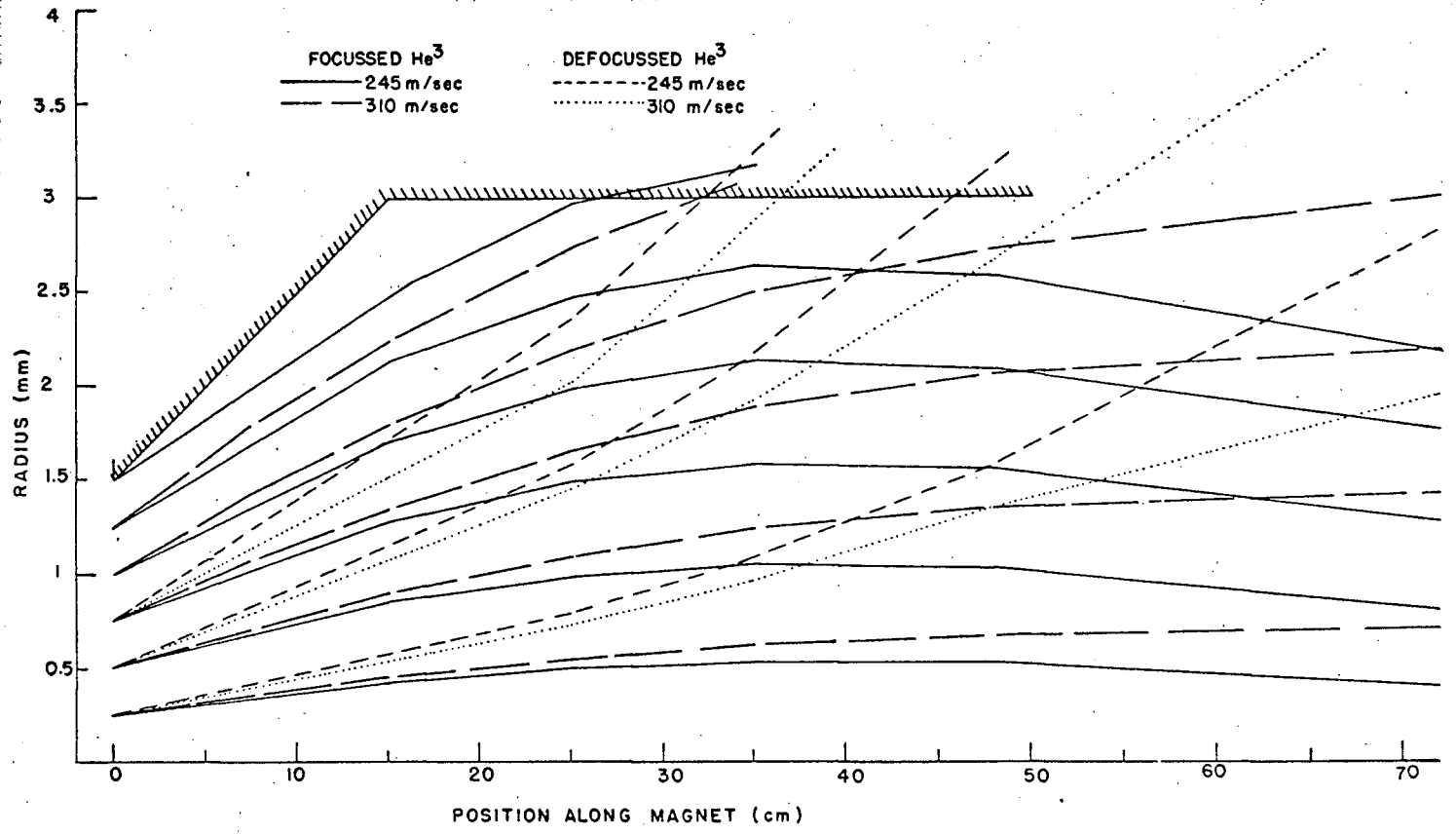

Fig. 41 Typical Trajectories of Focussed and Defocussed ^{3}He Atoms passing through the Hexapole Magnet. The Source-Magnet Separation is 15 cm and the Field at the Magnet Pole Tips is taken as 9000 Gauss.

which would contribute to the final intensity.

Glavish (G167, G168) has written a computer program which does this. His program takes into account all the possible trajectories the atoms can take and the velocity distribution of atoms in the beam. This program was initially used for calculations involving the focussed proton states for a beam with a Maxwellian velocity distribution. These calculations were used for optimizing the various system parameters for a polarized proton ion source developed at the University of Auckland. The program was modified at U.B.C. to calculate the trajectories of both the focussed and defocussed states of an atomic ^{3}He beam with the velocity distribution characteristic of a nozzle beam.

The relative intensity and polarization obtained inside an ionizer aperture 1.0 cm in diameter are shown in Figs. 42 and 43 as a function of the distance of the magnet entrance from the nozzle source and the temperature of the nozzle. Calculations were done for magnet-ionizer separations of 0, 10, and 20 cm. No change in the intensity and polarization inside the 0.5 cm radius ionization volume is predicted for these three separations. More will be said of these results in Chapter VIII.

For the conditions under which the magnet was operated namely, nozzle temperature = 7°K, Mach number of beam = 10 and a magnet-source separation = 15 cm, Glavish's program has been used to calculate the ratio of the total flux of atoms into the ionizer aperture with the magnetic field on to the

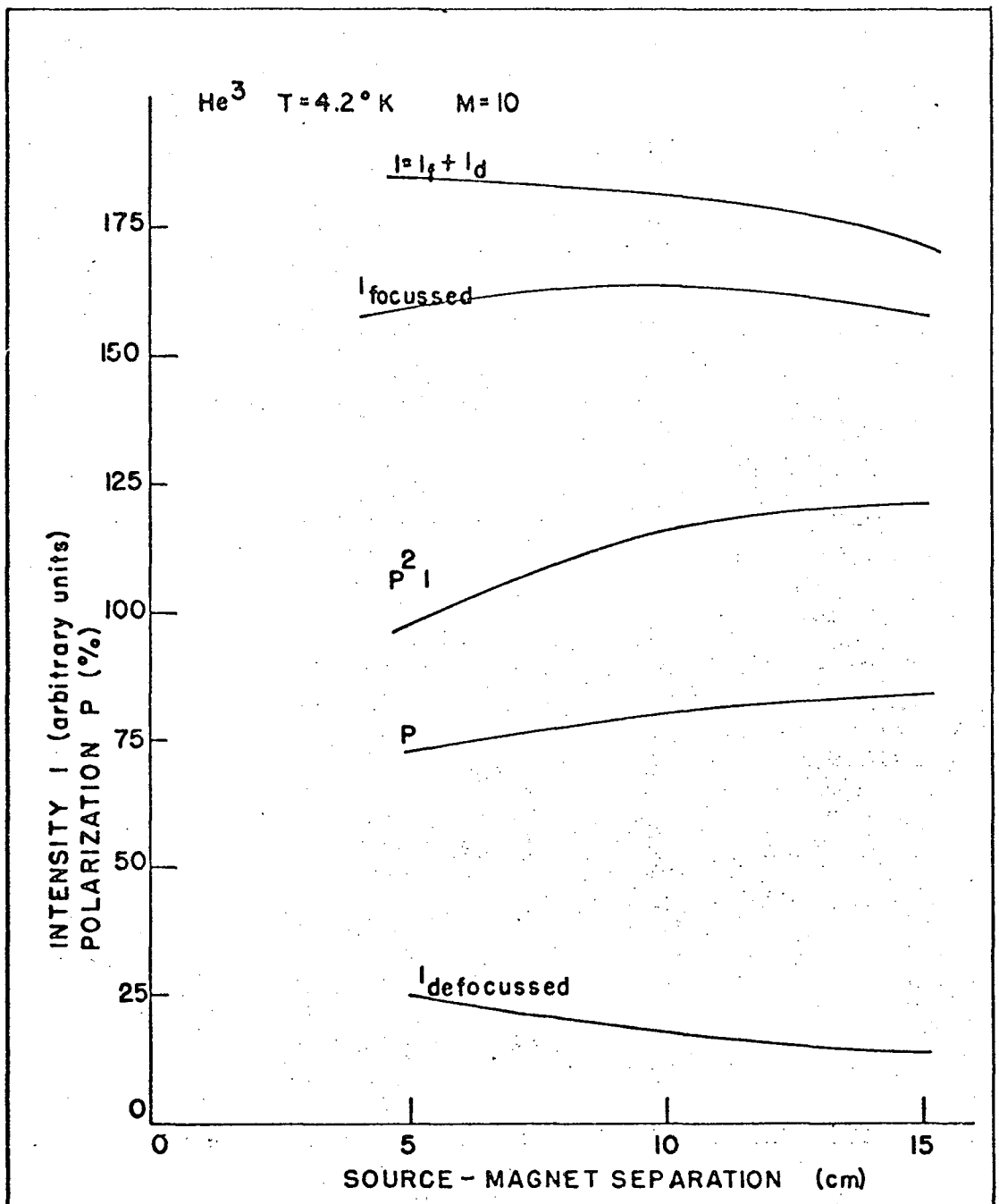

Fig. 42 Effect of Source-Magnet Separation on Intensity and Polarization of Atomic Beam. Nozzle at 4.2°K.

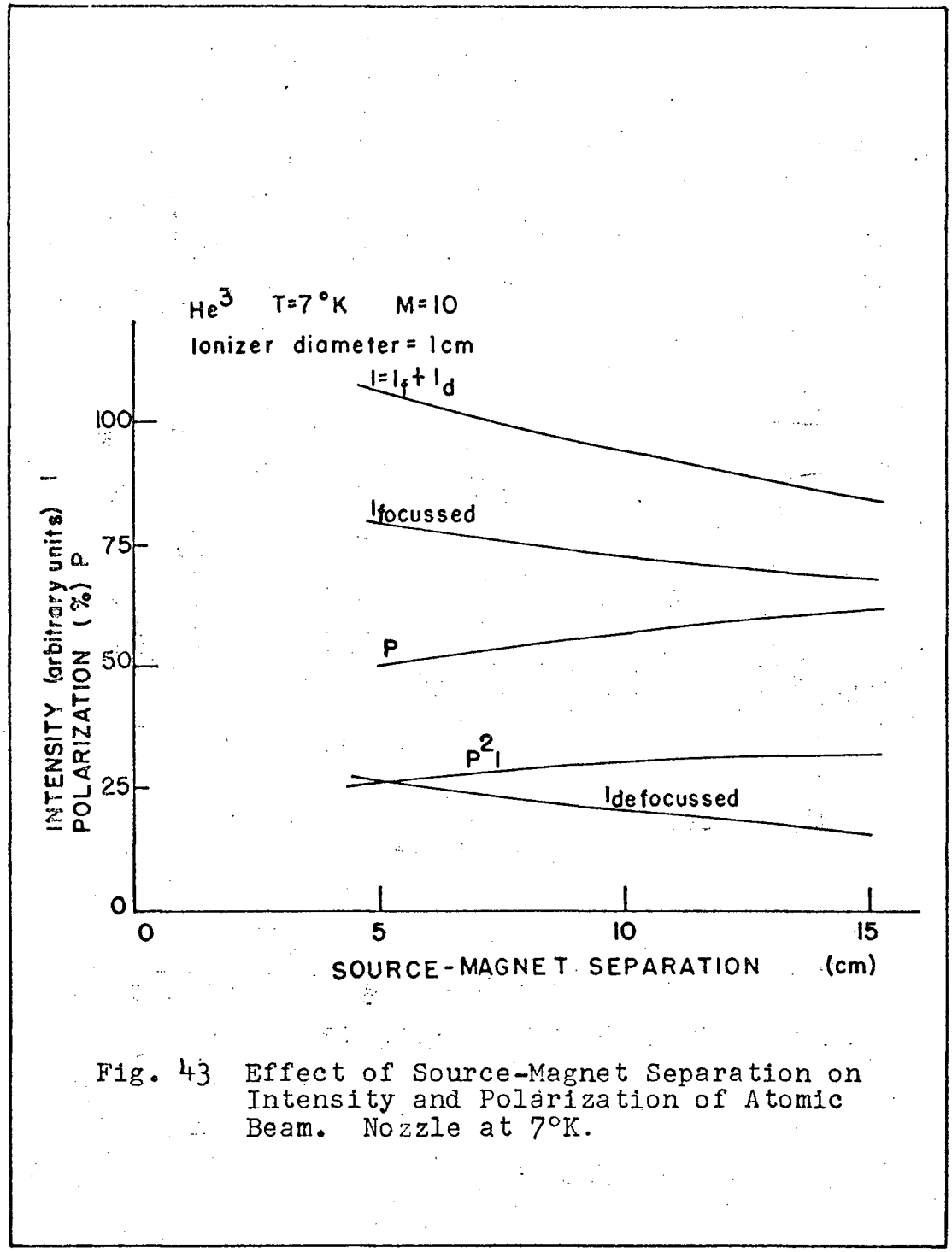

Fig. 43 Effect of Source-Magnet Separation on Intensity and Polarization of Atomic Beam. Nozzle at 7°K.

total flux of atoms into the ionizer aperture with the magnetic field off. This ratio (R) is equal to 1.33. The polarization predicted for the conditions mentioned above is 62%.

C. The Polarization Measurement and Ion Beam Yield.

Two detection methods were used in determining the polarization of the ^3He nuclei after passing through the hexapole magnet. The first method, using the differential Pirani gauge detector, measured the change in neutral beam intensity with the magnet turned on and off, while the second method measured the change in ionized beam under similar circumstances with the magnetic field on and off.

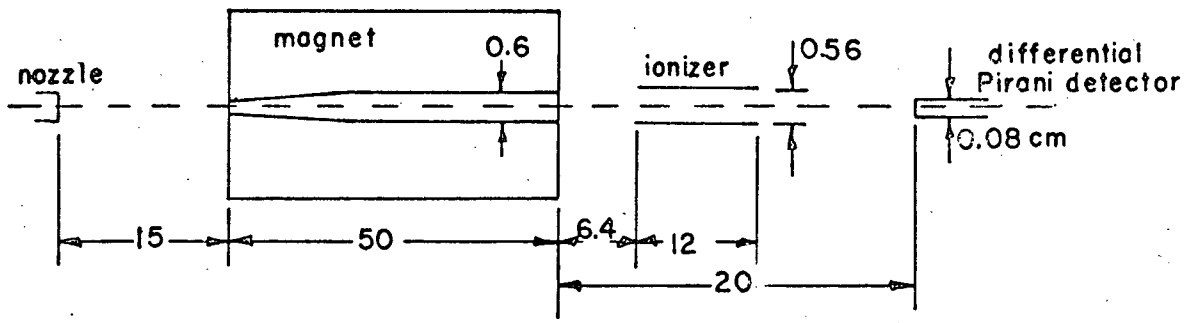

Fig. 44 Schematic Diagram Indicating Relative Location of Components Used in Atomic Beam Polarization Measurement. Dimensions in cm.

The location of the differential Pirani detector and the ionizer relative to the magnet while these measurements were made is shown in Fig. 44.

Typical results of the first method are shown in Fig. 45 where the effect of the magnetic field being on and off is shown. The increase of approximately 50% in neutral beam intensity is interpreted to indicate an effective

polarization of the ^3He nuclei passing through the magnet although it is difficult to quote any degree of accuracy to the absolute value of the increase.

Typical results obtained using the ionizer to measure the change in beam intensity with the magnetic field on and off are shown in Fig. 46. In this experimental measurement an increase in beam intensity of 30% was observed. Because of the small number of ions produced from the atomic beam as compared to the large number produced from the background gas (1:1000) the incoming atomic beam was modulated. The chopping system and associated detection electronics were described in Section 4B. The results from 18 measurements, similar to the one shown in Fig. 46, yielded a ratio R of the ion current with the magnet on to the ion current with the magnet off of $R = 1.32 \pm 0.1$. The increase of ionized beam obtained as a function of the magnet excitation current is shown in Fig. 47. The ratio R increased slowly as the magnet current was increased. This data is not inconsistent with the value of R reaching a plateau at a magnet current of 70 amps. This value of current corresponds to the value shown in Fig. 18 at which the magnetic field begins to saturate.

The measured ion current was 12 nA with the magnet on, the ionizer emission current at 750 mA and a plate voltage of 350 V. The conditions under which this measurement was made were such that the estimated ^3He atomic beam at the entrance to the magnet was 0.45×10^{18} atoms $(sr - sec)^{-1}$ and the most probable velocity of the beam was 310 m/sec. Assuming 50% of

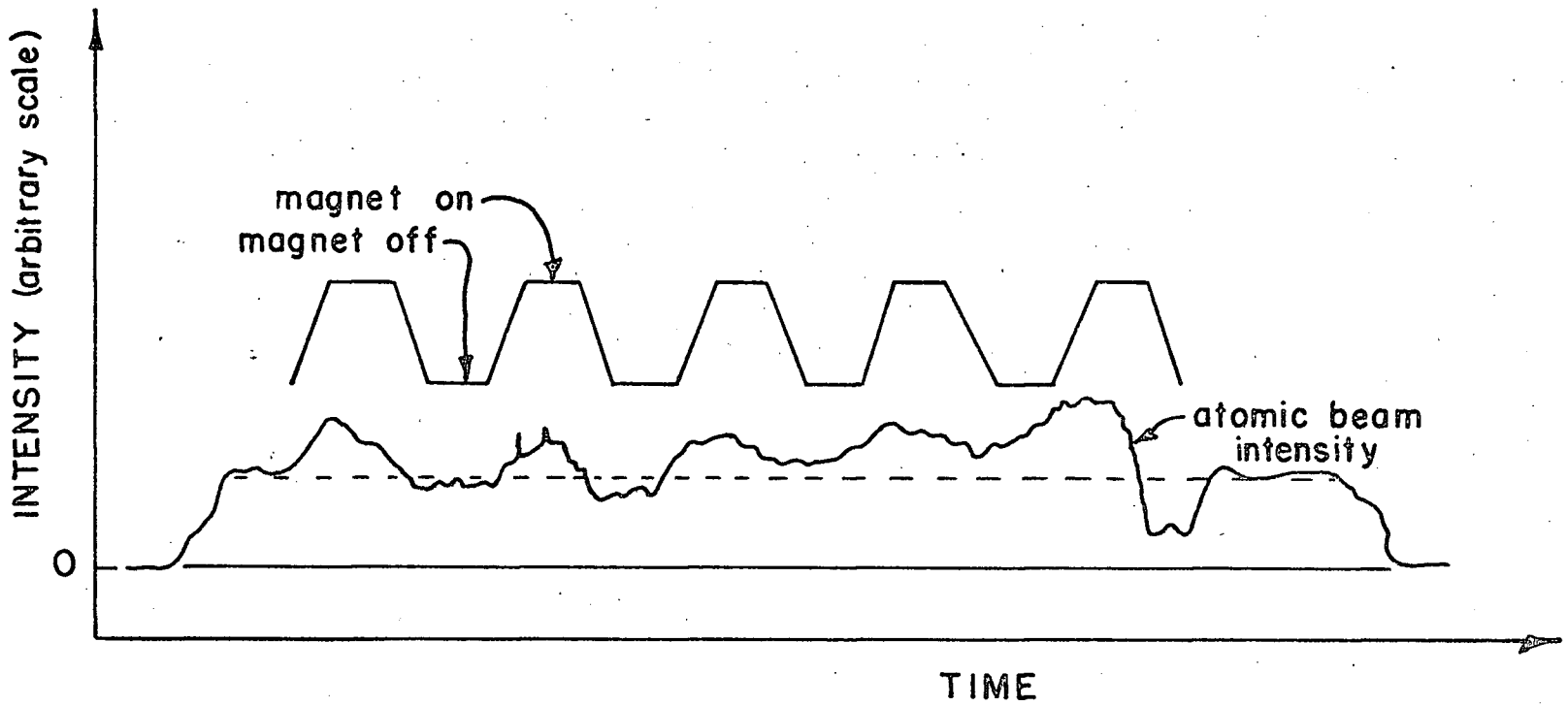

Fig. 45 Change in Differential Pirani Detector Signal when Hexapole Magnet is Turned On and Off.

the atoms entering the magnet pass through the ionizer then the 12 nA ion current corresponds to an ionization efficiency of 0.15%.

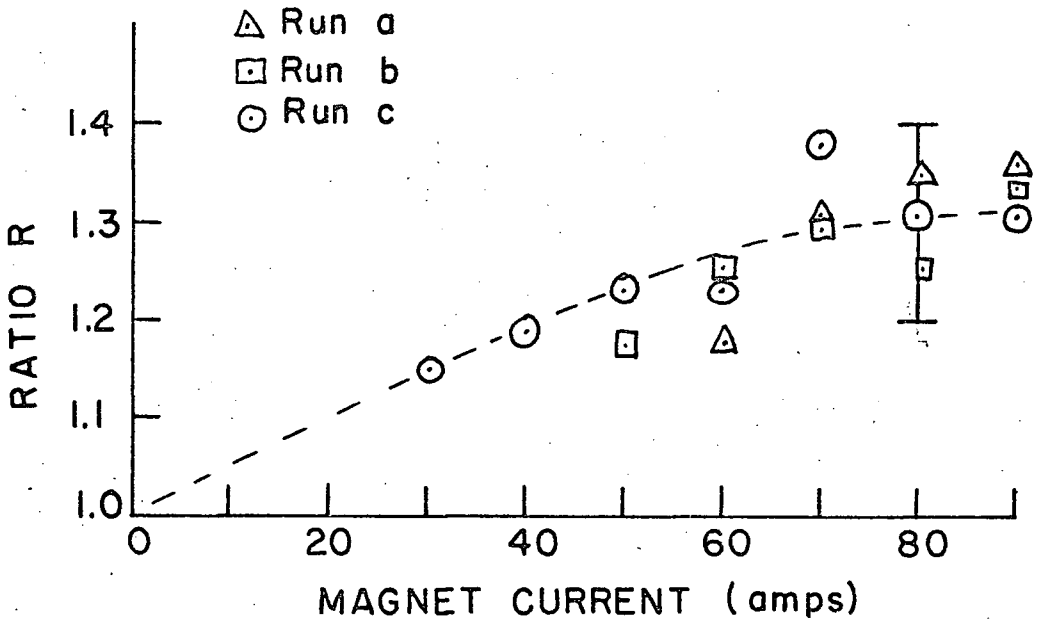

Fig. 47 Enhancement Ratio of Ionized Beam as a Function of Magnet Excitation Current.

The experimental ratio R = 1.32 ± 0.1 obtained by measuring the ion yield from the ionizer is in good agreement with the theoretically expected ratio R = 1.33 calculated using Glavish's program. This ratio is equivalent to a calculated polarization of the atomic beam of 62%. The actual polarization of the singly ionized ^{3}He will depend on the magnetic field strength in the ionizer. The expected polarization of the ionized beam as a function of field strength assuming the polarization of the atomic beam is 100% is shown in Fig. 3.

CHAPTER VIII

CONCLUSIONS

A. Comparison with other Sources of Polarized $^3He^+$ Ions.

Three methods are presently used for the production of polarized $^3He^+$ ions. The production of a polarized secondary beam following a nuclear reaction has been discussed through the example of elastic scattering of unpolarized ^3He by ^4He in Chapter I. The Rice University polarized ion beam obtained by optical pumping techniques has been discussed in Section 2A. The U.B.C. polarized beam obtained by atomic beam techniques is the subject of this thesis where the results of available polarization and ion current measurements are discussed in Section 7C. A comparitive summary of the polarization and ion current available from these three techniques is presented in Table 3. The time required in an experimental measurement to obtain a desired fractional error in the measurement is inversely proportional to P^2I. This figure of merit P^2I given in Table 3 demonstrates the advantage of the ion source technique over the secondary beam technique in producing a useful beam of polarized ^3He. The figure of merit is at least 3 orders of magnitude higher for the ion source techniques. Both the Rice University and U.B.C. ion sources have similar P^2I values but are characterized by low polarization and high ion current in the case of the Rice University source and high polarization and low current in the case of the U.B.C. source. Both the beam polarization and

Table 3

Comparison of different Methods of Producing Polarized $^3He^+$ Ions.

Method of Production	% Polarization P	Beam Current I	Figure of Merit P^2I
Secondary Beam eg. $^4He(^3He,^3He)^4He$	100%	.001 – .01 nA	10^{-6}
Optical Pumping Rice University Ion Source	5%	3 μA	.007
Atomic Beam U.B.C. Ion Source	65% Potentially 100%	12 nA	.005

extracted ion yield can be potentially increased in both the Rice and U.B.C. sources. The polarization of the Rice source might be increased as high as 60% and the U.B.C. source polarization to 100%. Improved atomic beam formation and ionization efficiency may result in an order of magnitude increase in the U.B.C. ion current.

B. Measurement of the $^3He^+$ Beam Polarization by the $D(^3He,P)^4He$ Reaction.

The measurement of the atomic beam polarization is discussed in Chapter VII and the theoretical relationship between the atomic beam polarization and the ionized beam polarization as a function of the magnetic field strength in the ionizer and target regions is illustrated in Fig. 3. In spite of this theoretical relationship an experimental determination of the ionized beam polarization would be desirable.

Although in principle the polarization of the ^3He beam could be determined by measuring the asymmetry in the $^4He(^3He, ^3He)^4He$ reaction; the energy required for a significant amount of P wave scattering in order to have a non-vanishing L·S spin-orbit force is inconvenient for preliminary ion source development work. A more suitable method is to use an exoergic nuclear reaction to produce polarized spin $\frac{1}{2}$ particles of sufficient energy to make polarization analysis by elastic scattering possible. An appropriate reaction is $D(^3He,P)^4He$ ($Q = 18.36$ MeV). If this reaction is initiated by S waves and assumed to proceed through the $J = 3/2 +$

resonance in Li^5 then a simple relationship exists between the polarization of the incoming ^3He beam $P(^3He)$ and the polarization $P_{(p)}$ of the protons which are emitted at an angle of 90° with respect to the direction of the axis of polarization of the incoming ^3He particles (Fi67)

$$P_{(p)} = -(2/3)\, P_{(^3He)} \qquad (23)$$

To measure the polarization of the Rice University polarized $^3He^+$ ion source the polarization of the protons was measured through the left-right asymmetry A of their elastic scattering in a high-pressure (35 atmospheres) helium filled polarimeter. Details of the experimental apparatus used are discussed by Findley (Fi67). The asymmetry A is defined as

$$A = \frac{N_L - N_R}{N_L + N_R}$$

where N_L is the number of protons scattered to the left side of the beam in the polarimeter and N_R the number scattered to the right and $N_L + N_R = N$, the total number of events. The polarimeter had an analyzing power of -0.6. Thus the measured experimental asymmetry A of the protons is related to the polarization of the ^3He beam $P(^3He)$ by

$$A = (-0.6)(-2/3)\, P_{(^3He)} = 0.4\, P_{(^3He)} \qquad (24)$$

The fractional error $\left(\frac{\Delta A}{A}\right)$ in the measured asymmetry is equal to

$$\frac{\Delta A}{A} = \frac{1}{\sqrt{N}} \sqrt{\frac{1}{A^2} - 1} \qquad (25)$$

where N is the total number of observed events.

The asymmetry in the case of the Rice polarization measurement was determined to be 0.0227 ± 0.0033 (Ba68). This

value is an averaged asymmetry obtained by reversing the sign of the beam polarization every 5 minutes to cancel errors due to detector solid angle and efficiency asymmetries in the polarimeter. To obtain this accuracy according to Eq. 25 required a total of 90,000 counts. For a ^3He beam current of 3-4 μA on a deuterium ice target at 300 KeV Findley reports a counting rate in the polarimeter of 2 events per second. Thus their measurement should take approximately 13 hours; however, they report approximately 18-24 hours of active data taking was required to obtain adequate statistics. The difference in the two times may be the result of background runs.

The time required to determine the polarization of the U.B.C. ion source can easily be estimated from Eq. 25 and the Rice group's experimental count rate. For a ^3He beam polarization of 0.65, A = 0.26 (This assumes strong field ionization). If a $\pm 20\%$ measurement of the beam polarization is desired $\frac{\Delta A}{A} = 0.2$ and Eq. 25 shows 350 counts are required. For weak field ionization the polarization is reduced by one-half and the number of counts required increased to about 1500. If the ^3He were accelerated to 600 KeV where the $D(^3He,P)^4He$ cross section is a maximum instead of the 300 KeV in the Rice University case, the cross section for proton production increases by a factor of 4 and the experimental count rate in the polarimeter thus increases by a factor of 4. However, the U.B.C. ion current is approximately 10 nA as compared to the Rice source 3-4 μA. Combining the increase in count rate

because of the higher ^3He energy and the decrease due to lower beam current the expected count rate is 2/100 counts per second. The measurement of the beam polarization to $\pm 20\%$ accuracy using this count rate and strong field ionization would require approximately 5 hours or using the quoted time of 18-24 hours for the Rice measurement our measurement would require 7-9 hours. Weak field ionization would increase the time required for these measurements by a factor of 4.

C. Possible Improvements of the Polarized $^3He^+$ Beam.

(1) Improvements Increasing the Atomic Beam Intensity.

One of the most effective ways of increasing the ultimate ion yield of the beam apparatus is to increase the neutral atomic beam intensity. From the data shown in Fig. 37 it appears as if considerable increases in intensity can be achieved by reducing the scattering in the nozzle-skimmer region. Reduced scattering is achieved by increasing the pumping speed and hence reducing the background gas pressure in this region. The pumping speed at the nozzle is limited by the long pumping channel from the nozzle to the Leybold pump and the restrictive geometry in the nozzle-skimmer region. A possible solution to these combined problems is to remove the present nozzle-skimmer pumping system and to pump the nozzle-skimmer region with the 10" diffusion pump presently pumping the skimmer-collimator region. The present skimmer-collimator region might be pumped either by the 10" pump also or by the pumps which presently pump the region downstream of the existing collimator. The discussion of the properties of

the nozzle operation given in Section 3C shows that the collimator might best be eliminated.

The ultimate improvement achieved by increased pumping speed may be limited by the small size of the nozzle and skimmer apertures. However, it does not appear unreasonable to expect an increase in beam intensity of a factor 2 with relatively simple modifications to the existing apparatus, perhaps even more with extensive modifications.

(2) Improvements to Reduce the Atomic Beam Velocity.

The reduction of the velocity to that corresponding to a stagnation temperature of 4.2°K, the temperature of the liquid helium in the cryostat, is expected with a better thermal attachment of the nozzle to the cryostat. The present nozzle is not in direct contact with the liquid but is attached by a brass bar to the bottom of the cryostat. This has proved to provide inadequate thermal contact as evidenced by velocity measurements of the beam and carbon resistance thermometer measurements of the nozzle. It is proposed that a new cryostat would be designed with the nozzle actually surrounded by the coolant. This should reduce the nozzle temperature to 4.2°K. In fact recent work, subsequent to the measurements mentioned in this thesis, with a modified cryostat has produced an atomic beam with a velocity corresponding to 4.2°K. This confirms that the high velocity measured previously was caused by poor thermal attachment of the nozzle to the cryostat. In the modified cryostat the nozzle is now almost completely surrounded by liquid helium

thus ensuring adequate thermal contact. Lowering the temperature of the nozzle from 7°K to nearer 4.2°K will improve the polarization. The improvement expected in the calculated trajectories of the lower temperature particles can be seen in Fig. 41 where the trajectories for both 310 m/sec (7°K) and 245 m/sec (4.2°K) particles are shown. As shown in this figure the 245 m/sec particles can be focussed to a point on the beam axis whereas the 310 m/sec particles are still diverging at the magnet exit. The results shown in Figs. 42 and 43 indicate that the polarization will increase from 62% with the 7°K beam to 84% with the 4.2°K beam.

The desirability of cooling the beam further to 2.2°K as was originally proposed (Wa63) is very evident from the point of view of increased separation of the spin states and increased ionization efficiency both of which depend on the velocity of the atoms.

(3) Improvements in Ionization Efficiency and Ion Extraction.

The difficulties in extracting a useful ion beam from the side of the ionizer, as must be done with the present ionizer, have not yet been fully considered. It will be most sensible to reconsider an axial ionizer because of the considerably increased ease with which the ions may be focussed into a useful beam after they leave the ionizer. In constructing a new ionizer care must be taken to insure minimum outgasing from the constituent components of the ionizer when the high electron emissin current bombards the plate and causes general

heating of the apparatus. The present ionization efficiency of 0.15% could be improved both by reduced atomic velocity and improved ionizer design. Reducing the atomic velocity increases the time the atoms stay in the ionization region thus increasing the ionization efficiency. Improved ionizer design would allow higher electron bombardment currents hence higher ionization efficiency. A new ionizer should be of the strong field type in order to take advantage of the significant enhancement of the ultimate nuclear polarization of the ionized beam as shown in Fig. 3.

(4) Overall System Improvement Possibilities by Changing the Geometry.

Some increase in beam intensity should, at first glance, be obtained by moving the source of atoms closer to the magnet entrance as the intensity of particles entering the magnet is proportional to $1/r^2$. This would also produce a real increase in ion current if the magnet were in fact able to focus the increased number of particles entering the magnet aperture. The difficulty is that the particles can be considered as coming from a point source; thus the additional particles enter the magnet with an initial divergence and radial location such that the present magnet is incapable of focussing the extra atoms into a useful beam. This effect is evident in Table 2 where the trajectories of atoms with varying radial displacements at the magnet entrance are tabulated for nozzle-magnet separations of 5 and 15 cm. For the increment size (0.025 cm) of the radial displacement used in these calculations,

particles with a radial displacement up to 0.075 cm at the entrance to the magnet pass through the magnet when the source-magnet separation is 15 cm. However, when the source-magnet separation is reduced to 5 cm only atoms which enter the magnet with a radial displacement from the axis of less the 0.025 cm pass through the magnet without hitting the pole pieces. Hence moving the magnet closer to the source will not result in all the additional particles being focussed into a useful beam. The comparison between varying source-magnet separation is shown more quantitatively in Fig. 42. The intensity I of focussed atoms passing through the ionizer annulus varies less than 3% when the source-magnet separation is varied from 5 to 15 cm. Also shown on this figure is the polarization P or relative amounts of focussed and defocussed atoms as defined earlier which enter the ionizer annulus. The polarization increases from a value of 73% for a source-magnet separation of 5 cm to 84% for a source-magnet separation of 15 cm. The parameter P^2I is of greater interest to the experimentalist as this figure is inversely related to the length of time needed to obtain the same statistics for a particular experiment with beams of varying intensity and polarization. The value of this parameter is 20% larger for source-magnet separations of 15 cm than for the 5 cm separation. As a result of the above there appears to be no advantage in moving the magnet closer to the source as any slight gain in intensity through the ionizer annulus is lost because of a larger reduction in the polarization of the atoms.

(5) Improvements in Vacuum System Reducing Background Ion Yield.

The maximum acceptable pressure in a given section of the atomic beam apparatus is determined by the criterion that the beam should not suffer a significant loss of intensity by scattering as it passes through the region of interest. At room temperature it is not too difficult to keep beam losses to 10%. This means that the mean free path of the gas must be 10 times the scattering length through which the beam must pass. Thus if the chamber were 100 cm long a pressure of 10^{-5} Torr would be adequate to keep beam losses to less than 10%. At lower temperatures, in particular at liquid helium temperatures, the situation is considerably more difficult as the mean free path at a given pressure is approximately 100 times smaller than at room temperature.

The pressure requirement in the ionizing chamber is set by the ratio of the number of polarized $^3He^+$ ions produced from the atomic beam to the number of ions formed from the background gas in the ionizing region. Naturally this ratio should be as large as possible; the exact size depends on the composition of the background gas ions as it may be possible to separate the useful polarized $^3He^+$ ions from the background gas ions by means of momentum analysis. The present situation of about 15 nA of polarized $^3He^+$ ions and 10 μA of background gas ions is naturally intolerable. Momentum analysis is required to reduce contaminants in the beam to a minimum so undesired ions would be eliminated. The atomic beam density

in the ionizer region corresponds to a pressure of approximately 10^{-7} Torr; the background gas pressure should be brought well below this as the volume of background gas available for ionization is larger than the volume of beam particles.

To improve the pressure in the ionization region a bulkhead should be installed between the magnet and the ionizer chamber. This dividing bulkhead would have only a small hole, the size of the magnet exit, located on the beam axis to allow the beam to pass through to the ionizer. Such a system would reduce the flow of unpolarized ^{3}He atoms from the magnet region and would allow efforts to improve the vacuum to be concentrated in one specific area. Reduction of outgassing of the ionizer can be achieved by rebuilding the ionizer with stainless steel parts and by a reduction in the number of wires and other materials which are subject to excessive outgassing upon electron bombardment.

Although the vacuum requirements in the magnet region are less severe than in the ionization region, 10^{-5} Torr would be satisfactory, a pump should be provided on the magnet chamber to ensure low background gas pressures around the pole tips of the magnet.

APPENDIX A

INTENSITY FROM A FREELY EXPANDING JET

The angular dependence of the intensity from a freely expanding nozzle jet is given by Eq. 11 as

$$I(\theta) = K \cos^2\left(\frac{\theta\pi}{2\phi}\right) \tag{A1}$$

where θ is the angle between the radius vector to any point and the normal to the aperture and ϕ is a constant,

$$\phi = 1.365 \qquad \text{for} \qquad \gamma = 1.67$$

The total integrated intensity over all angles must equal the total molecular gas flow N through the nozzle given by Eq. 5 ie.

$$\text{Total flux} = N = \int_{\theta=0}^{\theta=\pi/2} I(\theta)\, d\Omega(\theta) \tag{A2}$$

where

$$d\Omega(\theta) = 2\pi \sin\theta\, d\theta$$

Thus

$$N = \int_{\theta=0}^{\theta=\pi/2} K \cos^2\left(\frac{\pi\theta}{2\phi}\right) \pi \sin\theta\, d\theta \tag{A3}$$

Performing the integration results in $N = 2K\pi(0.265)$

or $K = N / [2\pi(0.265)] = 0.6\,N$

$$I(\theta) = 0.6\,N \cos^2\left(\frac{\theta\pi}{2\phi}\right) \tag{A4}$$

Therefore the centerline intensity ($\theta = 0$) can be written

$$I_{is} = I_{centerline} = 0.6\ N \text{ atoms (steradian - sec)}^{-1} \qquad \text{(A5)}$$

APPENDIX B

INTENSITY AND VELOCITY DISTRIBUTION OF PARTICLES IN JET AFTER PASSING THROUGH SKIMMING ORIFICE

The intensity and velocity distribution of atoms arriving at a location on the beam axis downstream from the skimmer can be calculated with reference to Fig. 48. Assuming radial flow originating at the nozzle with the velocity of mass motion w in the radial direction and a uniform atomic density over that region cut out by the skimmer, the number of particles passing through some small rectangular area $(da)^2$ located a distance $\ell \gg X_S$ along the axis can be found by summing the contributions to the flux from all elemental areas $dA = 2\pi X_S^2 \sin\alpha \, d\alpha$ on the spherical surface which characterizes the transition from continuum to free molecular flow. The flux of particles passing through this area is given by:

$$\dot{n}_d = \sum_A \int_{u_1} \int_{u_2} \int_{u_3} n \, dA \, u \, f(u_1) \, f(u_2) \, f(u_3) \, du_1 \, du_2 \, du_3 \qquad \text{(B1)}$$

where n is the number density of particles on the spherical surface and u is their velocity. The orientation of u_1, u_2 and u_3 is shown in Fig. 48 and

$$f(u_1) = \left(\frac{m}{2\pi k T_1}\right)^{1/2} e^{-\frac{m}{2kT_1}(u_1 - w)^2}$$

$$f(u_2) = \left(\frac{m}{2\pi k T_1}\right)^{1/2} e^{-\frac{m}{2kT_1}(u_2)^2} \qquad \text{(B2)}$$

$$f(u_3) = \left(\frac{m}{2\pi k T_1}\right)^{1/2} e^{-\frac{m}{2kT_1}(u_3)^2}$$

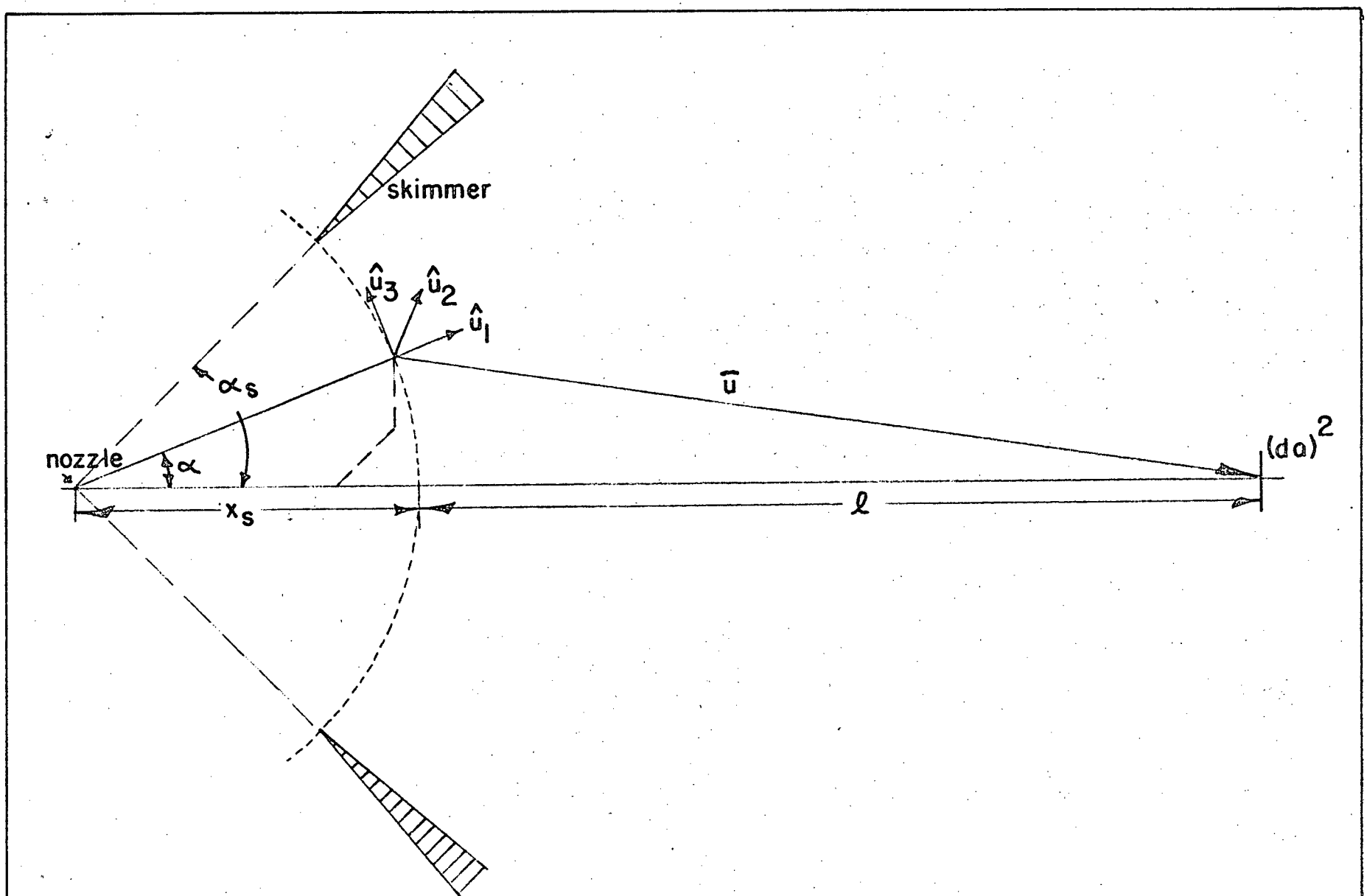

Fig. 48 Defining Diagram for Calculation of Flow through Nozzle-Skimmer System.

As the area $(da)^2$ is very small, only atoms with velocity very close to $\overline{u}$ where $\overline{u}$ is the velocity vector from the point in question to the center of the area $(da)^2$ as shown in Fig. 49 will contribute to the flux.

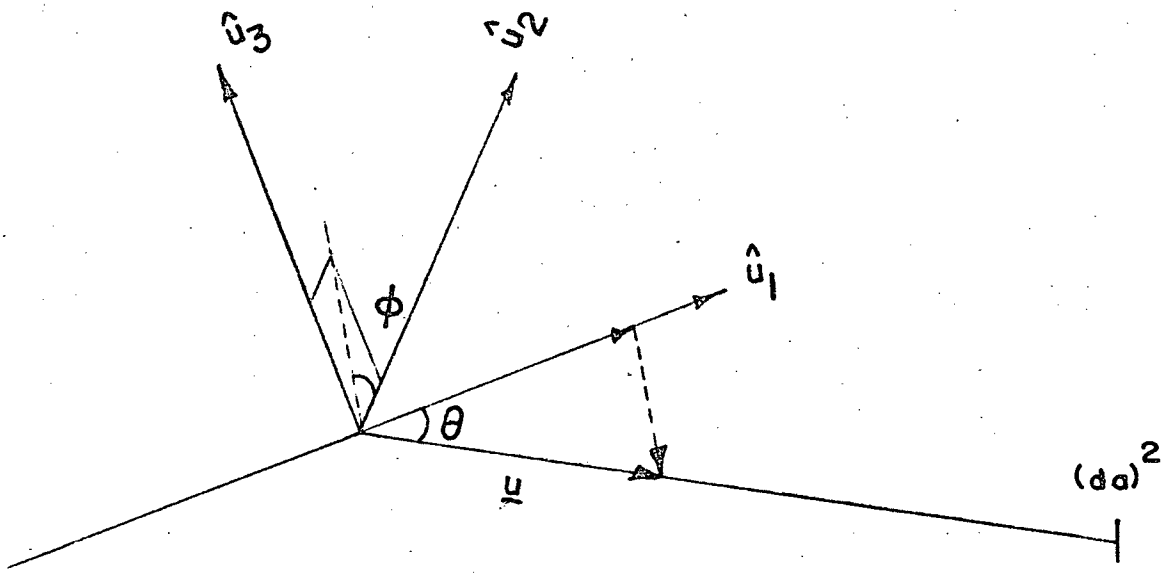

Fig. 49 Definition of Certain Variables used in Calculation of Flow through Nozzle-Skimmer System.

Thus the values of u_1, u_2, and u_3 may be written, defining θ and ϕ as in Fig. 49,

$$\begin{aligned} u_1 &= u\cos\theta \\ u_2 &= u\sin\theta\cos\phi \\ u_3 &= u\sin\theta\sin\phi \end{aligned} \tag{B3}$$

Since $\ell >> x_s$, $\alpha \approx \theta$ and the small increment in u_1, u_2 and u_3 may be written as

$$du_1 du_2 du_3 = u^2 du \left(\frac{da}{\ell}\right)^2$$

where u is allowed to take on all values from 0 to ∞ Eq. B1 can be written as:

$$\dot{n}_d = \int_A \int_u n\, dA \left(\frac{m}{2\pi kT_1}\right)^{3/2} u^3 e^{-\frac{m}{2kT}(u\cos\theta - w)^2} e^{-\frac{m}{2kT}(u\sin\theta)^2} \frac{(da)^2\, du}{\ell^2} \quad (B4)$$

now

$$\frac{\dot{n}_d}{\frac{(da)^2}{\ell^2}} = I \qquad \text{atoms / steradian - sec}$$

and

$$dA = 2\pi X_s^2 \sin\alpha\, d\alpha$$

also $$n X_s^2 = I_{is}/W \quad (B5)$$

Thus Eq. B4 becomes

$$I = \int_\alpha \int_u \frac{I_{is}}{W} 2\pi \sin\alpha\, d\alpha \left(\frac{m}{2\pi kT_1}\right)^{3/2} u^3 e^{-\frac{m}{2kT}(u\cos\theta - w)^2} e^{-\frac{m}{2kT}(u\sin\theta)^2} du$$

$$\alpha = 0 \to \alpha_s$$
$$u = 0 \to \infty \quad (B6)$$

Integrating over angles α

$$I = \int_u \frac{I_{is}}{W} 2\pi \left(\frac{m}{2\pi kT_1}\right)^{3/2} u^3 \left(\frac{-2kT_1}{2uwm}\right)\left\{e^{\frac{2uwm}{2kT_1}\cos\alpha_s} - e^{\frac{2uwm}{2kT_1}}\right\} e^{-\frac{m}{2kT_1}(u^2+w^2)} du \quad (B7)$$

thus

$$\frac{dI}{du} = I_{is}\left(\frac{m}{2\pi kT_1}\right)^{1/2} \frac{u^2}{W^2} e^{-\frac{m}{2kT_1}(u^2+w^2)}\left\{e^{\frac{2uwm}{2kT}} - e^{\frac{2uwm\cos\alpha_s}{2kT}}\right\} \quad (B8)$$

now integrating over velocities u and recalling

$$\left(\frac{m}{2kT_1}\right)^{1/2} W = M\sqrt{\frac{\gamma}{2}} \quad (B9)$$

$$\frac{I}{I_{is}} = \frac{1}{2}\left[1+\frac{1}{2\mu w^2}\right]\left[1-\operatorname{erf}(-\sqrt{\mu}\,w)\right] + \frac{(1-\cos\alpha_s)}{2w\sqrt{\pi\mu}}\,e^{-\mu w^2}$$

$$-\frac{1}{2}\left[\cos^2\alpha_s + \frac{1}{2\mu w^2}\right] e^{-\mu w^2 \sin^2\alpha_s}\left[1-\operatorname{erf}(-\sqrt{\mu}\,w\cos\alpha_s)\right] \qquad \text{(B10)}$$

where $\mu = \frac{m}{2kT_1}$

for Mach numbers $M > 3$, $e^{-\mu w^2}$ may be replaced by its assymptotic limit 0 and $\operatorname{erf}(-\sqrt{\mu}\,w)$ and $\operatorname{erf}(-\sqrt{\mu}\,w\cos\alpha_s)$ may be replaced by their assymptotic limit -1. Eq. B10 thus simplifies to

$$I = I_{is}\left[\left(\frac{1}{M^2\gamma}+1\right) - e^{-\frac{M^2\gamma}{2}\sin^2\alpha_s}\left(\frac{1}{M^2\gamma}+\cos^2\alpha_s\right)\right] \qquad \text{(B11)}$$

for $M > 3$ $\qquad \frac{1}{M^2\gamma} \ll 1$

and Eq. B11 becomes

$$I = I_{is}\left(1-\cos^2\alpha_s\, e^{-\frac{\gamma M^2}{2}\sin^2\alpha_s}\right) \qquad \text{(B12)}$$

However, if in Eq. B4 the radial divergence of the flow at the skimmer had been neglected (ie. the flow is assumed parallel at the skimmer entrance) then $\Theta = 0$ $\qquad \int dA = A_{SKIMMER}$ and Eq. B4 becomes

$$\dot{n}_d = \int_u n A_s \left(\frac{m}{2\pi kT_1}\right)^{3/2} u^3\, e^{-\frac{m}{2kT_1}(u-w)^2}\,\frac{(da)^2\,du}{l^2} \qquad \text{(B13)}$$

as before

$$I = \frac{\dot{n}_d}{\frac{(da)^2}{l^2}}$$

and $$n A_s w = I_{is} \pi \sin^2 \alpha_s$$

Thus

$$I = \int_{u=0 \to \infty} \frac{I_{is} \pi \sin^2 \alpha_s}{w} \left(\frac{m}{2\pi k T_1}\right)^{3/2} u^3 e^{-\frac{m}{2kT_1}(u-w)^2} du \qquad \text{(B14)}$$

$$\frac{dI}{du} = \frac{I_{is} \pi \sin^2 \alpha_s}{w} \left(\frac{m}{2\pi k T_1}\right)^{3/2} u^3 e^{-\frac{m}{2kT_1}(u-w)^2} \qquad \text{(B15)}$$

Performing the integration over u in Eq. B14 results in

$$I = I_{is} \sin^2 \alpha_s \left\{ \left(\frac{3}{2} + \frac{\gamma M^2}{2}\right) \left(\frac{1 + \operatorname{erf} \sqrt{\frac{\gamma M^2}{2}}}{2}\right) + \frac{1 + \frac{\gamma M^2}{2}}{\sqrt{2\pi \gamma M^2}} e^{-\frac{\gamma M^2}{2}} \right\} \qquad \text{(B16)}$$

for $M > 3$

$$e^{-\frac{\gamma M^2}{2}} \approx 0$$

$$1 + \operatorname{erf} \sqrt{\frac{\gamma M^2}{2}} \approx 2$$

Thus reducing Eq. B16 to

$$I = I_{is} \sin^2 \alpha_s \left(\frac{3}{2} + \frac{\gamma M^2}{2}\right) \qquad \text{(B17)}$$

Eq. B15 can be written

$$\frac{dI}{du} = \frac{I_{is} \pi \sin^2 \alpha_s}{w} \left(\frac{m}{2\pi k T_1}\right)^{3/2} \cdot g(u) \qquad \text{(B18)}$$

where

$$g(u) = u^3 e^{-\frac{m}{2kT_1}(u-w)^2} \qquad \text{(B19)}$$

Eq. B8 can be cast into a similar form

$$\frac{dI}{du} = \frac{I_{is}}{W^2}\left(\frac{m}{2\pi kT_i}\right)^{1/2} q(u)\ G(u) \tag{B20}$$

where

$$G(u) = \frac{1}{u}\left\{1 - e^{-\frac{2uwm}{2kT_i}(1-\cos\alpha_s)}\right\} \tag{B21}$$

and $q(u)$ is as given by Eq. B19.

APPENDIX C

TRAJECTORIES OF PARTICLES PASSING THROUGH A HEXAPOLE MAGNET

1. Equation of Motion of a Magnetic Dipole in a Axially Symmetric Multipole Field.

The energy of interaction $\mathcal{H}$ between a magnetic field $\underline{H}$ and a magnetic dipole $\underline{M}$ is $\mathcal{H} = -\underline{M}\cdot\underline{H}$. The classical energy W follows from this

$$W = -|\mu||\underline{H}|\cos\theta \qquad (C1)$$

where $\underline{M}$ has been replaced by the magnetic moment μ which is at an angle θ with respect to the magnetic field $\underline{H}$. Letting the component of the magnetic moment in the direction of the applied field be equal to μ_{eff} we can write Eq. C1

$$W = -\mu_{eff}|\underline{H}| \qquad (C2)$$

The force on a dipole of constant strength is given by

$$\begin{aligned}\underline{F} &= -\text{grad } W \\ &= \mu_{eff}\,\text{grad}|\underline{H}|\end{aligned} \qquad (C3)$$

Two poles of a radially symmetric multipole field are shown in Fig. 50. The z axis is taken as the axis of symmetry and the field is assumed to be constant in this direction, ie. $\frac{\partial H}{\partial z} = 0$. The determination of the magnetic field strength in the plane perpendicular to this axis is then a two dimensional problem.

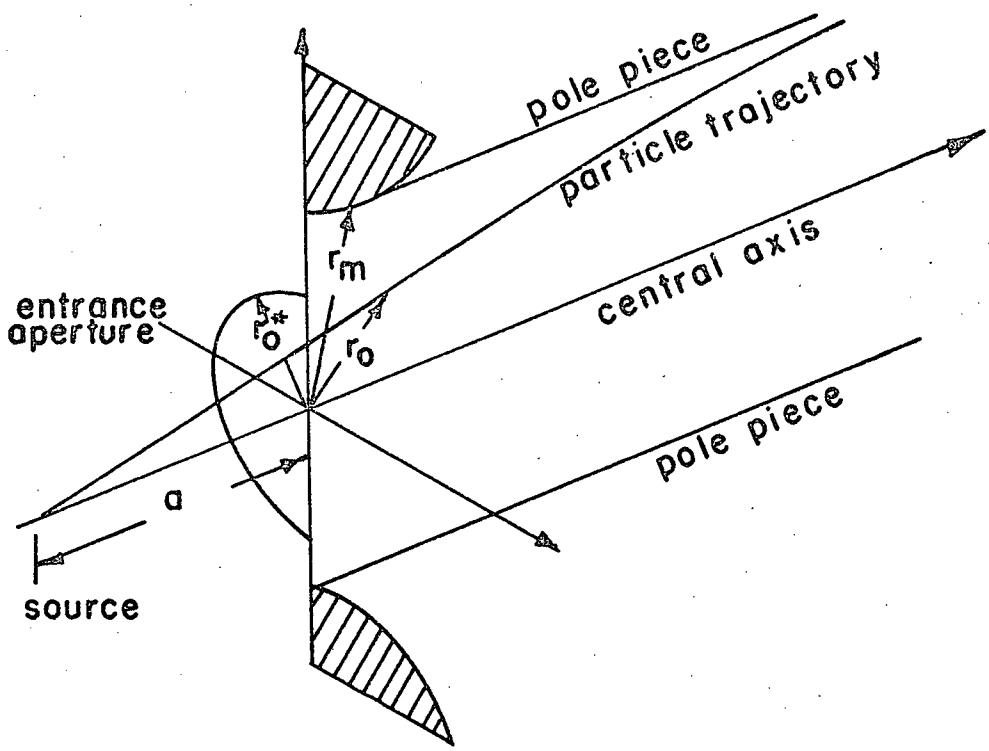

Fig. 50 Schematic Diagram Showing Two Poles of a Radially Symmetric Magnet.

The pertinent Maxwell Equations are:

$$\nabla \cdot B = 0$$

$$\nabla \times B = j + \frac{\partial D}{\partial t}$$

$$B = \mu_o H + M$$

in free space $j = D = M = 0$ and the first two equations become:

$$\nabla \cdot H = 0 \qquad (C4)$$

$$\nabla \times H = 0 \qquad (C5)$$

Hence H can be described as the gradient of a scalar magnetic potential ϕ as

$$H = -\text{grad}\ \phi \qquad (C6)$$

using Eq. C4

$$\nabla^2 \phi = 0 \qquad (C7)$$

which is Laplace's equation. A general solution of Laplace's equation suitable for two dimensional geometry is

$$F(V) = \phi + i\psi \tag{C8}$$

where

$$V = x + iy \tag{C9}$$

A general property of this solution is that lines of constant ϕ are perpendicular to lines of constant ψ. As ϕ represents the lines of constant magnetic potential, the lines of constant ψ represent the lines of force.

Writing Eq. C6 in vector form as

$$\underline{H} = -\frac{\partial \phi}{\partial x}\,\underline{i} - \frac{\partial \phi}{\partial y}\,\underline{j}$$

where $\underline{i}$ and $\underline{j}$ are unit vectors in the x and y direction, the square of the magnitude of $\underline{H}$ is

$$|H|^2 = \left|\frac{\partial \phi}{\partial x}\right|^2 + \left|\frac{\partial \phi}{\partial y}\right|^2$$

using the Cauchy-Riemann equations

$$\frac{\partial \psi}{\partial x} = -\frac{\partial \phi}{\partial y}$$

the above expression becomes

$$|H|^2 = \left|\frac{\partial \phi}{\partial x}\right|^2 + \left|\frac{\partial \psi}{\partial x}\right|^2$$

which using Eq. C8 can be written as

$$|H|^2 = \left|\frac{\partial F(V)}{\partial x}\right|^2 \tag{C10}$$

and

$$|H| = \left|\frac{\partial F(V)}{\partial x}\right| \tag{C11}$$

Any polynomial in V is a solution of Laplace's equation. Thus the general solution given by Eq. C8 can be expressed as

$$F(V) = \sum_{n=0}^{\infty} d_n V^n \qquad (C12)$$

Each possible multipole field configuration can be expressed by one term of this polynomial as

$$F_n(V) = d_n V^n \qquad (C13)$$

In cylindrical coordinates, $\underline{r}$ and $\underline{\theta}$, the vector $\underline{V} = x + iy$ can be written as

$$\overline{V} = r(\cos\theta + i\sin\theta)$$

and Eq. C12 may be written

$$F(V) = \sum_{0}^{\infty} |d_n|\, e^{i\delta_n} r^n e^{in\theta}$$

thus

$$\phi + i\psi = \sum |d_n|\, r^n e^{i(n\theta+\delta_n)}$$

$$\therefore \phi = \sum_{0}^{\infty} |d_n|\, r^n \cos(n\theta+\delta_n)$$

now $H = -\text{grad}\ \phi$ from Eq. C6

and in cylindrical coordinates the expression for the gradient is

$$\text{grad} = \underline{r}\frac{\partial}{\partial r} + \underline{\theta}\frac{1}{r}\frac{\partial}{\partial\theta}$$

where $\underline{r}$ and $\underline{\theta}$ are unit vectors.

Thus

$$H = -\sum_{n} n|d_n| r^{n-1}\left[\underline{r}\cos(n\theta+\delta_n) - \underline{\theta}\sin(n\theta+\delta_n)\right] \qquad (C14)$$

For a single multipole field we may drop the summation and the relative azimuthal term δ_n.

H_n is radial where $n\theta + \delta_n = 0, \pi, 2\pi, 3\pi, \ldots$

In any case $\left|\underline{r}\cos(n\theta+\delta_n) - \underline{\theta}\sin(n\theta+\delta_n)\right| = 1$

and

$$H = n|d_n| r^{n-1} \qquad (C15)$$

In terms of Eq. C3 and Eq. C15 the force on the dipole is

$$\underline{F} = \mu_{eff}\ n(n-1)\ d_n\ r^{n-2} \tag{C16}$$

and is always in the direction of $\underline{r}$. The equation of motion of the dipole is then

$$F = m\ \frac{\partial^2 r}{\partial t^2}$$

or $$\frac{\partial^2 r}{\partial t^2} = \frac{\mu_{eff}}{m}\ n(n-1)\ d_n\ r^{n-2} \tag{C17}$$

where m is the mass of the dipole and t is time.

Those dipoles which have a negative component of the magnetic moment in the direction of the applied field H are accelerated towards the central axis of the radial field, while those with a positive component in this direction are deflected away from the central axis.

2. Trajectories of a Magnetic Dipole in a Parallel Hexapole Magnet.

The hexapole field is represented by the general term of Eq. C12

$$F(V) = d_3 V^3 \tag{C18}$$

using Eqs. C8 and C9 and changing to cylindrical coordinates

$$F(V) = \phi + i\psi = d_3\ r^3 (\cos 3\theta + i \sin 3\theta)$$

thus the lines of constant magnetic potential ϕ and the lines of force ψ are given by

$$\phi = d_3\ r^3 \cos 3\theta \tag{C19}$$

and

$$\psi = d_3\ r^3 \sin 3\theta \tag{C20}$$

The parameters used to describe the hexapole magnet are shown in Fig. 50, where a is the distance from the source to the magnet entrance, r_o is the radial position of the particle at the magnet entrance, r_m is the radial distance to the pole tips, Ho is the strength of the magnetic field at the pole tips, and r and z denote the position of the particle in the magnet. In terms of these parameters, the magnitude of the magnetic field strength at any radial position, as given by Eq. C15 is

$$|H| = \left(\frac{r}{r_m}\right)^2 H_o \tag{C21}$$

The equation of motion of the dipole in the hexapole field as given by Eq. C17 is

$$\frac{\partial^2 r}{\partial t^2} = \pm \frac{2\mu_{eff} H_o r}{m r_m^2}$$

letting

$$b_1 = \sqrt{\frac{2\mu_{eff} H_o}{m r_m^2}} \tag{C22}$$

the trajectory of the focussed particles (those with a negative component of μeff in the direction of H) is

$$r = A \sin b_1 t + B \cos b_1 t$$

using $z = ut$ this equation becomes

$$r = A \sin\left(\frac{b_1 z}{u}\right) + B \cos\left(\frac{b_1 z}{u}\right) \tag{C23}$$

and the slope of the trajectory is

$$\frac{\partial r}{\partial z} = \frac{b_1}{u}\left\{A \cos\left(\frac{b_1 z}{u}\right) - B \sin\left(\frac{b_1 z}{u}\right)\right\} \tag{C24}$$

If the particles enter the parallel magnet with divergence S and radius r_s then the arbitrary constants are $B = r_s$ and $A = \frac{Su}{b_1}$. In terms of these constants Eqs. C23 and C24 become

$$r = \frac{Su}{b_1} \sin\left(\frac{b_1 z}{u}\right) + r_s \cos\left(\frac{b_1 z}{u}\right) \tag{C25}$$

$$\frac{\partial r}{\partial z} = S \cos\left(\frac{b_1 z}{u}\right) - \frac{r_s b_1}{u} \sin\left(\frac{b_1 z}{u}\right) \tag{C26}$$

The solution of the differential equation

$$\frac{\partial^2 r}{\partial t^2} = b_1^2 r$$

describing the trajectories of the defocussed particles is

$$r = A_1 e^{b_1 t} + B_1 e^{-b_1 t}$$

which using $z = ut$ can be written as

$$r = A_1 e^{\frac{b_1 z}{u}} + B_1 e^{-\frac{b_1 z}{u}}$$

If the particles have slope S_d and position r_d at $z = 0$ then

$$r = \frac{1}{2}\left(r_d + \frac{u S_d}{b_1}\right) e^{\frac{b_1 z}{u}} + \frac{1}{2}\left(r_d - \frac{u S_d}{b_1}\right) e^{-\frac{b_1 z}{u}} \tag{C27}$$

3. Trajectories of a Magnetic Dipole in a Tapered Hexapole Magnet.

The geometrical parameters describing the tapered hexapole magnet are shown in Fig. 51. The magnetic field strength, Ho, at the pole tips is assumed to be constant along the length of the magnet as should be approximately true if the magnet iron is saturated in this region. This turns out to be a good approximation in practice.

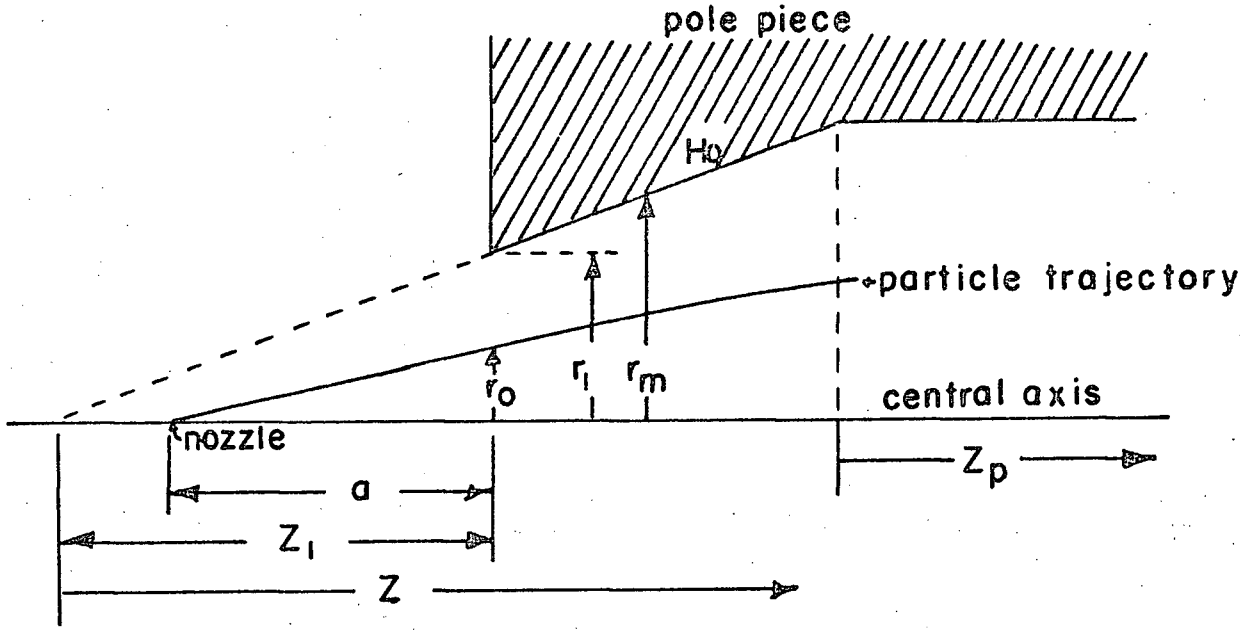

Fig. 51 Schematic Diagram Showing the Parameters used to describe the Tapered Hexapole Magnet.

By similar triangles in Fig. 51, the pole tip radius r_m as a function of z is given by

$$r_m = \frac{r_1}{z_1} z \qquad (C28)$$

At any position z, the field strength in a plane perpendicular to the direction z is given by Eqs. C. 21 and C. 28.

$$|\underline{H}| = \frac{r^2 z_1^2}{r_1^2 z^2} H_0$$

The calculation of the trajectories is limited to those cases for which the variation of the magnetic field strength in the z direction is sufficiently small so that the component of grad $|\underline{H}|$ in this direction can be neglected. Thus for the case of the tapered hexapole field, the general equation of motion of the dipole as given by Eq. C17 becomes

$$\frac{\partial^2 r}{\partial z^2} = \pm \left(\frac{2 \mu_{eff} H_o z_1^2}{m r_1^2 u^2} \right) \frac{r}{z^2}$$

where the change of variable $z = ut$ has been made.

Letting

$$b_2^2 = \frac{2 \mu_{eff} H_o z_1^2}{m r_1^2 u^2} \qquad (C29)$$

the above expression becomes

$$\frac{\partial^2 r}{\partial z^2} = \pm b_2^2 \frac{r}{z^2} \qquad (C30)$$

where the positive and negative signs refer to the defocussed and focussed portions of the beam respectively.

Within the above stated limitations, the solution of this equation should not differ significantly from the solution for the case of the parallel magnet. The solution of the negative part of Eq. C30 can be shown (Ax65) to be

$$r = D z^{1/2} \cos \left\{ \sqrt{b_2^2 - \tfrac{1}{4}} \ln z + \varepsilon \right\} \qquad (C31)$$

The two arbitrary constants D and ε, determined by the boundary conditions that $r = r_o$ and $\frac{\partial r}{\partial z} = \frac{r_o}{a}$ at $z = z_1$, are

$$D = \frac{r_o}{\sqrt{z_1}} \sqrt{\frac{b_2^2 + \frac{z_1}{a}\left(\frac{z_1}{a} - 1\right)}{b_2^2 - 1/4}}$$

and

$$\varepsilon = -\tan^{-1} \left\{ \frac{-\frac{1}{2} + \frac{z_1}{a}}{\sqrt{b_2^2 - 1/4}} \right\} - \sqrt{b_2^2 - \tfrac{1}{4}} \ln z_1$$

using these two constants the radial positions of the dipole in the tapered hexapole magnet at a position z, as given by Eq. C31 as

$$r = 2r_0 \sqrt{\frac{b_2^2 + \frac{z_1}{a}\left(\frac{z_1}{a} - 1\right)}{4b_2^2 - 1}} \sqrt{\frac{z}{z_1}} \cos \eta \tag{C32}$$

$$\eta = \sqrt{4b_2^2 - 1} \ln \sqrt{\frac{z}{z_1}} - \tan^{-1} \left\{ \frac{\frac{2z_1}{a} - 1}{\sqrt{4b_2^2 - 1}} \right\} \tag{C33}$$

By differentiating Eq. C32 with respect to z, the slope of the trajectory is

$$\frac{\partial r}{\partial z} = S = \frac{r_0}{\sqrt{z z_1}} \sqrt{\frac{b_2^2 + \frac{z_1}{a}\left(\frac{z_1}{a} - 1\right)}{4b_2^2 - 1}} \left\{ \cos \eta - \sqrt{4b_2^2 - 1} \sin \eta \right\} \tag{C34}$$

The solution of the positive part of Eq. C30, corresponding to the trajectory of the defocussed particles is

$$r = C_3 z^{\frac{1+\sqrt{4b_2^2+1}}{2}} + C_4 z^{\frac{1-\sqrt{4b_2^2+1}}{2}} \tag{C35}$$

The arbitrary constants, C_3 and C_4, as determined by the boundary conditions are

$$C_3 = r_0 \left\{ \frac{2z_1 - a\left(1 - \sqrt{4b_2^2+1}\right)}{2a\sqrt{4b_2^2+1}} \right\} z_1^{-\left(\frac{1+\sqrt{4b_2^2+1}}{2}\right)}$$

$$C_4 = r_0 \left\{ \frac{a_0\left(1 + \sqrt{4b_2^2+1}\right) - 2z_1}{2a\sqrt{4b_2^2+1}} \right\} z_1^{-\left(\frac{1-\sqrt{4b_2^2+1}}{2}\right)}$$

Substituting these two equations in Eq. C35 the radial position r of the defocussed particles at position z in the hexapole magnet is

$$r = \frac{r_0}{2}\left[\left\{\frac{\frac{2z_1}{a} - \left(1-\sqrt{4b_2^2+1}\right)}{\sqrt{4b_2^2+1}}\right\}\left(\frac{z}{z_1}\right)^{\frac{1+\sqrt{4b_2^2+1}}{2}} + \left\{\frac{1+\sqrt{4b_2^2+1} - \frac{2z_1}{a}}{\sqrt{4b_2^2+1}}\right\}\left(\frac{z}{z_1}\right)^{\frac{1-\sqrt{4b_2^2+1}}{2}}\right] \tag{C36}$$

By differentiating this expression with respect to z the slope of the trajectory of the defocussed particles at position z in the hexapole magnet is

$$\frac{\partial r}{\partial z} = S_d = \frac{r_0}{4z_1}\left[\frac{\left\{1+\sqrt{4b_2^2+1}\right\}\left\{\frac{2z_1}{a} - \left(1-\sqrt{4b_2^2+1}\right)\right\}}{\sqrt{4b_2^2+1}}\left(\frac{z}{z_1}\right)^{\frac{-1+\sqrt{1+4b_2^2}}{2}}\right. \tag{C37}$$

$$\left. + \frac{\left\{1-\sqrt{4b_2^2+1}\right\}\left\{1+\sqrt{4b_2^2+1} - \frac{2z_1}{a}\right\}}{\sqrt{4b_2^2+1}}\left(\frac{z}{z_1}\right)^{\frac{-1-\sqrt{1+4b_2^2}}{2}}\right]$$

Thus the trajectories of the particles through a combined tapered and parallel hexapole magnet are obtained for the case of the focussed particles as follows. First the position and slope of the particles at the end of the tapered section are obtained using Eqs. C32 and C34. The position and slope of the particles in the parallel region are then calculated using Eqs. C25 and C26. A similar proceedure for the defocussed particles uses Eqs. C36 and C37 to calculate the position and slope at the end of the tapered section and uses

Eq. C27 to calculate the position in the parallel region.

APPENDIX D

CALCULATION OF SIGNAL SHAPE FROM TIME-OF-FLIGHT APPARATUS

If the chopper allows only an infinitely short burst of particles to start on the way to the detector and if the detector is infinitely short then the signal $S(t)$ observed at the detector can be directly related to the differential intensity distribution function $I(v) = \frac{dI}{dv}$ of the particles in the initial beam

$$S(t) = A'' \frac{I(v)}{v} \qquad \text{where} \quad v = \frac{L}{t} \qquad \text{and} \quad A'' = \text{constant} \qquad \text{(D1)}$$

since the detector signal is proportional to the density $D = \frac{I}{v}$ of the particles at the detector separated by a distance L from the source.

Unfortunately the chopper takes a finite length of time to pass across the atomic beam profile and as a result a group of particles with a finite time spread is allowed past the chopper. Also the detector has a finite length so that the signal received will be a sum of contributions from all sections of the detector.

Consider the case where the chopper allows a rectangular burst of particles such as shown in Fig. 52 to enter the system. This distribution will be called the shutter function. Also assume the detector has a length ℓ' and the response from all sections of it are equal, that is we have a rectangular detector response function shown in Fig. 53. The geometry of the system is now as shown in Fig. 54. Consider some point ℓ in

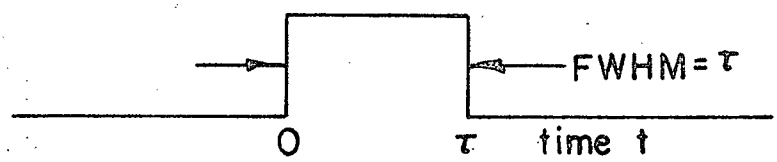

Fig. 52 Rectangular Chopper Shutter Function.

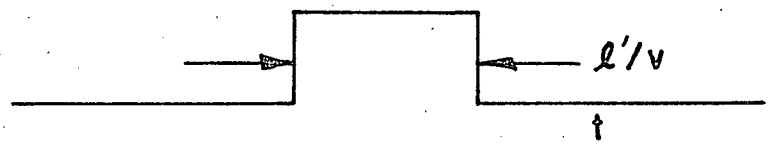

Fig. 53 Rectangular Detector Response Function.

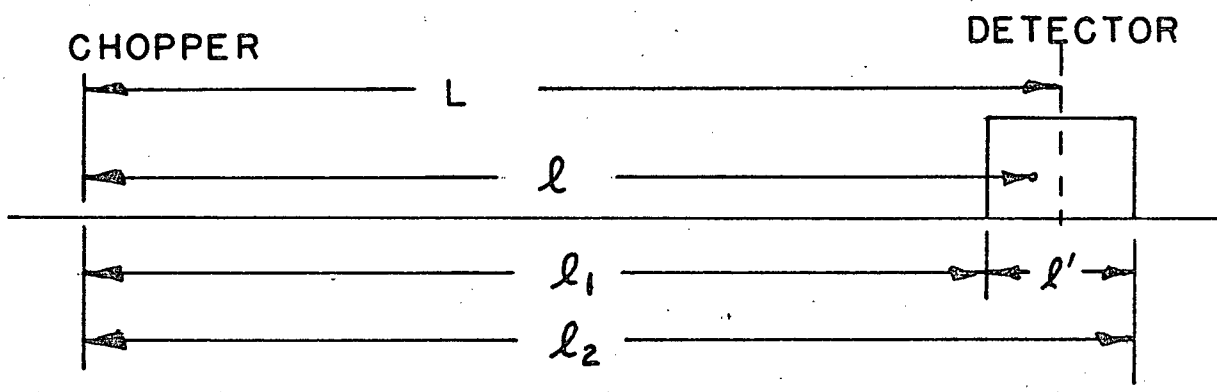

Fig. 54 Geometry of Time-of-Flight Apparatus.

the detector at some time t; the signal arising from particles at this position in space and time $S(t,\ell)$ is given by:

$$S(t,\ell) = \int_{V_1}^{V_2} A'' \frac{I(v)}{V} dV \qquad (D2)$$

since an increment in intensity is given by $dI = I(v)\,dv$

where

$$V_1 = \ell/t$$
$$V_2 = \ell/(t-\tau) \qquad \text{provided} \qquad t > \tau \qquad (D3)$$

Summing over contributions from all elements of the detector

$$S(t) = \int d\ell \; S(t,\ell)$$

$$S(t) = \int_{\ell_1}^{\ell_2} d\ell \int_{V_1(\ell,t)}^{V_2(\ell,t)} A'' \frac{I(v)}{V} dV \qquad (D4)$$

Taking the form of the differential intensity distribution function recommended by Hagena and Morton (Ha67)

$$I(v) = \frac{dI}{dv} = A' v^2 e^{-\beta(v-w)^2} \qquad (17)$$

where A' = constant

$$\beta = \frac{m}{2kT_1}$$

we have

$$S(t) = \int_{\ell_1}^{\ell_2} d\ell \int_{V_1}^{V_2} A v \, e^{-\beta(v-w)^2} dV \qquad (D5)$$

where A = constant

making a change of variable

$$X = \sqrt{\beta}\,(v-w)$$

$$dx = \sqrt{\beta}\,dV$$

we have

$$S(t) = \int_{\ell_1}^{\ell_2} d\ell\, A \int_{X_1}^{X_2} \left(\frac{X}{\sqrt{\beta}} + W \right) e^{-X^2} \frac{dX}{\sqrt{\beta}} \tag{D6}$$

where

$$X_1 = \sqrt{\beta} \left(\frac{\ell}{t} - W \right)$$

$$X_2 = \sqrt{\beta} \left(\frac{\ell}{t-\tau} - W \right)$$

recalling

$$\operatorname{erf} z = \frac{2}{\sqrt{\pi}} \int_0^z e^{-t^2} dt$$

and

$$\int_A^B -2x\, e^{-x^2} dx = e^{-x^2} \Big|_A^B$$

we have

$$S(t) = \int_{\ell_1}^{\ell_2} d\ell\, A \left[\frac{W}{2} \sqrt{\frac{\pi}{\beta}} \left\{ \operatorname{erf}\left(\sqrt{\beta} \left(\frac{\ell}{t-\tau} - W \right) \right) - \operatorname{erf}\left(\sqrt{\beta} \left(\frac{\ell}{t} - W \right) \right) \right\} - \frac{1}{2\beta} \left\{ e^{-\beta \left(\frac{\ell}{t-\tau} - W \right)^2} - e^{-\beta \left(\frac{\ell}{t} - W \right)^2} \right\} \right] \tag{D7}$$

now recalling

$$\int_{Z_2}^{Z_1} \operatorname{erf} t'\, dt' = i\left(\operatorname{erfc} Z_1 - \operatorname{erfc} Z_2 \right) - \int_{Z_1}^{Z_2} dt'$$

and making the change of variables

$$t_2' = \sqrt{\beta}\left(\frac{\ell_2}{t-\tau} - w\right) \qquad t_2'' = \sqrt{\beta}\left(\frac{\ell_2}{t} - w\right)$$

$$t_1' = \sqrt{\beta}\left(\frac{\ell_1}{t-\tau} - w\right) \qquad t_1'' = \sqrt{\beta}\left(\frac{\ell_1}{t} - w\right)$$

after some simplification

$$S(t) = \frac{A w}{2\sqrt{\beta}}\sqrt{\frac{\pi}{\beta}}\left[i(t-\tau)(\operatorname{erfc} t_2' - \operatorname{erfc} t_1') - it(\operatorname{erfc} t_2'' - \operatorname{erfc} t_1'')\right]$$

$$+ \frac{A\sqrt{\pi}}{2\beta\sqrt{\beta}2}\left[-(t-\tau)(\operatorname{erfc} t_2' - \operatorname{erfc} t_1') + t(\operatorname{erf} t_2'' - \operatorname{erf} t_1'')\right] \quad (D8)$$

now $\quad i\operatorname{erfc} z = -z(1-\operatorname{erf} z) + \frac{1}{\sqrt{\pi}} e^{-z^2}$

Thus S(t) reduces to

$$S(t) = \frac{A}{2}\sqrt{\frac{\pi}{2}}\left\{\left[w\ell_2 - (t-\tau)\left(w^2 + \frac{1}{2\beta}\right)\right]\operatorname{erf} t_2'\right.$$

$$\left. - \left[w\ell_1 - (t-\tau)\left(w^2 + \frac{1}{2\beta}\right)\right]\operatorname{erf} t_1' + \frac{w}{\sqrt{\beta}}\frac{t-\tau}{\sqrt{\pi}}\left[e^{-t_2'^2} - e^{-t_1'^2}\right]\right. \quad (D9)$$

$$- \left[w\ell_2 - t\left(w^2 + \frac{1}{2\beta}\right)\right]\operatorname{erf} t_2''$$

$$+ \left[w\ell_1 - t\left(w^2 + \frac{1}{2\beta}\right)\right]\operatorname{erf} t_1'' - \frac{w}{\sqrt{\beta}}\frac{t}{\sqrt{\pi}}\left[e^{-t_2''^2} - e^{-t_1''^2}\right]$$

A computer programme was written to calculate the above function for various values of τ, ℓ_2 and ℓ_1. For the fixed ℓ_1 and ℓ_2 used in this experiment the effect τ has on widening the FWHM of the observed signal Δt as compared to the theorectical signal Δt_o is summarized in Fig. 26 where $T \equiv \tau$.

APPENDIX E

REPRINTED FROM
6th INT'L. SYMPOSIUM ON RAREFIED GAS DYNAMICS, 2

ACADEMIC PRESS INC., NEW YORK

A LOW TEMPERATURE NOZZLE BEAM FOR A POLARIZED $^3He^+$ ION SOURCE

R. Vyse, J.C. Heggie and M.K. Craddock
Physics Department, University of British Columbia

Helium beam intensities obtained from nozzles cooled to 77°K and 4.2°K are studied for possible use as an atomic beam source in a polarized $^3He^+$ ion source.

Polarized ion sources require atomic beams of high intensity to counteract the very low ionization efficiencies obtainable by electron bombardment. Furthermore, ^3He atoms have only their small nuclear magnetic moment, so that Stern-Gerlach splitting of the two spin states requires an unreasonably long magnet unless the atomic velocities are sufficiently small. A nozzle of the style suggested by Kantrowitz and Grey[1], cooled to liquid helium temperatures, therefore appeared to be a possible solution to the requirements of high intensity and low velocity.

Many groups have studied the behaviour of atomic beams produced by small nozzles and have found substantial departures from the ideal behaviour originally postulated. These departures are attributed to the interaction[2] between the skimmer and the supersonic beam, and the background gas scattering[3] taking place in the region between the nozzle and the skimmer. Previous work using cryogenically cooled nozzles[4] and helium gas, however, has been aimed more at examining condensation than at maximizing the beam intensity.

The atomic beam source has been briefly described by Axen[5] and consists of a D = 0.2 mm diameter nozzle and 0.4 mm diameter skimmer attached to a cryostat capable of sustained operation at 4.2°K. The differential pumping system simultaneously provides the vacuum required for the operation of the atomic beam and the cryogenic system.

With this source we are examining the behaviour of an

atomic ^{4}He beam with the nozzle at room, liquid nitrogen and liquid helium temperatures. In each case the skimmer and collimator are cooled to the same temperature as the nozzle. Operation of the atomic beam source at room temperature using an 0.2 mm diameter converging nozzle shows the standard dependence[2] of intensity on nozzle-skimmer separation measured in nozzle diameters, L/D, (Fig. 1). At 77°K measurements have so far been made at four different separations, and indicate a similar dependence over a compressed distance scale. At 4.2°K measurements have been restricted to two separations with the tubing nozzle described below.

Figure 2 shows the effect of nozzle temperature (T_o) and pressure (P_o) on beam intensity for two fixed nozzle-skimmer separations. For these measurements the orifice consisted of a section of 0.0095" diameter tubing approximately 10 nozzle diameters in length. The behavour of the tubing nozzle is similar to that of a converging nozzle, as can be seen in the insert of intensity variation with nozzle-skimmer separation. The periodic scatter in experimental points in the insert is due to an alignment difficulty. Typical nozzle exhaust chamber pressures (P_{BG}-mTorr) are shown in brackets beside the relevant experimental points. A similar set of curves is shown in Fig. 3 for a 0.2 mm diameter nozzle made by piercing a hole in a piece of 0.001" brass shim shock. Again the typical background pressures in the nozzle exhaust chamber are shown.

There is evidence that the beam is being attenuated by scattering by background gas in both the nozzle exhaust chamber and in the region between the skimmer and collimator. Typical pressures in the skimmer-collimator region, P_{sc}, measured 2 cm from the beam axis and corrected for thermal transpiration, are tabulated in Table 1 along with the estimated resulting fraction of beam observed (I/I_o) for typical points chosen from Fig. 3. The I/I_o ratio was calculated assuming a simple exponential scattering relationship using a viscosity based mean free path. Uncertainties in the effective mean free path for scattering out of a beam at 4.2°K, and in the pressure measurements, give rise to larger uncertainties still in the attenuation because of its exponential dependence. The uncertainties quoted in Table 1 are based on $\pm$ 50% uncertainties in mean free path.

The ratio of observed to theoretical beam intensities,

uncorrected for attenuation, is plotted as a function of the Knudsen to Mach number ratio in Fig. 4 for the experimental points shown in the previous figure. The Knudsen number is based on calculated free stream conditions at the skimmer entrance and the Mach number is determined using the nozzle-skimmer separation and the method of characteristics solution of Owen and Thornhill[6]. Considering the extent of the attenuation of the higher P_o measurements at 4.2°K, the results of Fig. 4 show a considerable increase in beam intensity over what we might expect based on the results of Fenn and Deckers as indicated by the straight line.

REFERENCES

1. A.Kantrowitz, J.Grey, Rev. Sci. Instr. 22, 328 (1951).
2. J.B.Fenn, J.Deckers, 3rd Int. Symp. on Rarefied Gas Dynamics, 1, 497, Academic Press (1966).
3. J.B.Fenn, J.B.Anderson, 4th Int. Symp. on Rarefied Gas Dynamics, 2, 311, Academic Press (1966).
4. E.W.Becker, R.Klingelhofer, P.Lohse, Z.Naturforschung, 17a, 432 (1962)
5. D.Axen, M.K.Craddock, K.L.Erdman, W.Klinger, J.B.Warren, Proc. 2nd Int. Symp. on Polarization Phenomena of Nucleons, 94, Birkhauser, Basel (1966).
6. P.L.Owen, C.K.Thornhill, ARC R and M #2616 (1952).

TABLE 1

Attenuation of Beam Between Skimmer and Collimator

T_o (°K)	P_o (Torr)	P_{sc} (Torr)	I/I_o
77	7	10^{-4}	0.92 ± .05
77	15	1.5×10^{-4}	0.88 ± .08
77	36	3.2×10^{-4}	0.72 ± .1
77	134	1.6×10^{-3}	0.25 ± .15
4.2	2	3×10^{-5}	0.45 ± .15
4.2	7½	7×10^{-5}	0.15 ± .1
4.2	20	2×10^{-4}	0.0045 ± .07
4.2	32	3.5×10^{-4}	0.00007 ± .01

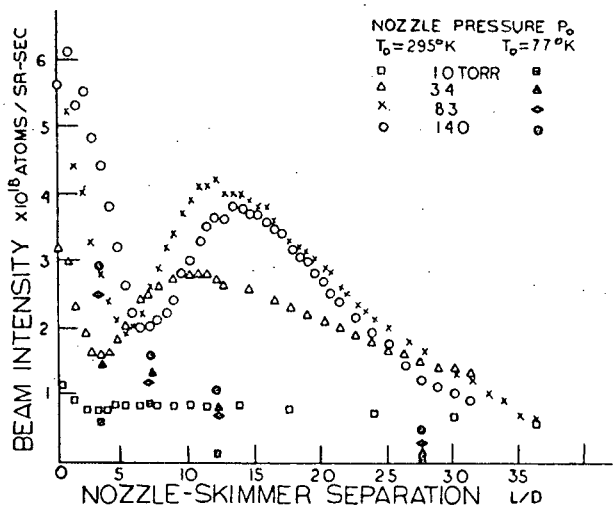

Fig. 1. Typical Results from Atomic Beam Source

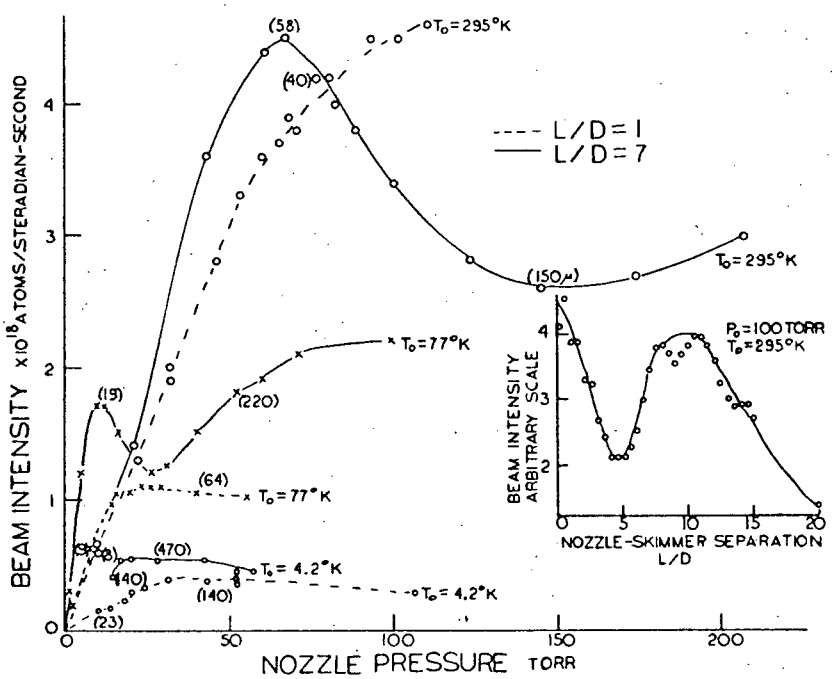

Fig. 2. Beam Intensity as a Function of Pressure (Tubular Nozzle)

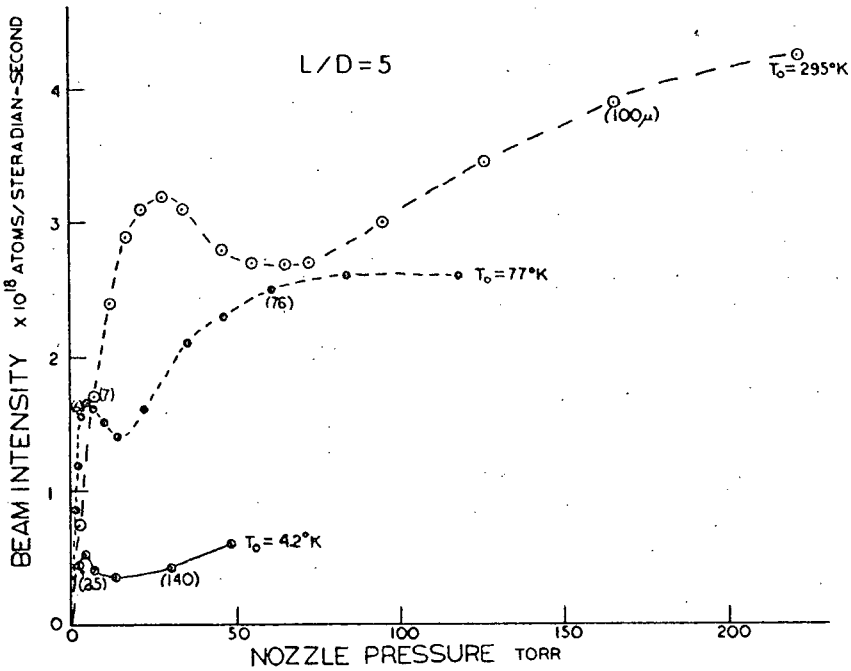

Fig. 3. Beam Intensity as a Function of Pressure

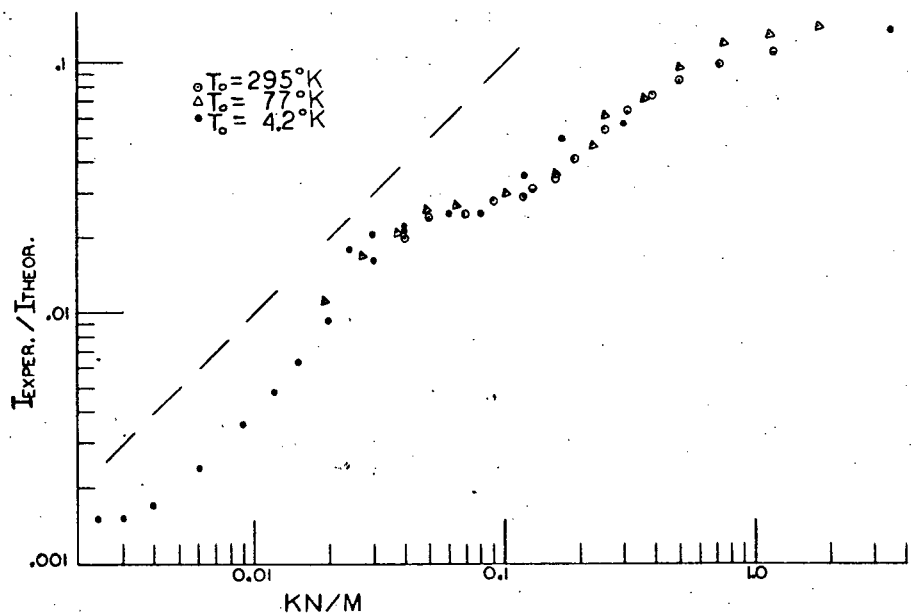

Fig. 4. The Ratio of Experimental to Theoretical Beam Intensity as a Function of Knudesen to Mach Number Ratio.

APPENDIX F

LOW TEMPERATURE ATOMIC ^3He BEAM FOR USE IN A POLARIZED $^3He^+$ ION SOURCE

R. Vyse, D. Axen and M.K. Craddock
Rev. Sci. Instr. In press

BIBLIOGRAPHY

Ab 66 N. Abuaf, J.B. Anderson, R.P. Andres, J.B. Fenn, D.R. Miller, 5th Int. Sym. on Rarefield Gas Dynamics, Academic Press, N.Y. (1966).

An 65a J.B. Anderson, J.B. Fenn, Physics of Fluids 8, 780 (1965).

An 65b J.B. Anderson, J.B. Fenn, 4th Int. Sym. on Rarefied Gas Dynamics, Academic Press, N.Y. (1965).

An 66 J.B. Anderson, R.P. Fenn, J.B. Fenn, Molecular Beams, Advances in Chemical Physics Vol. X Interscience (1966).

As 66 H. Ashkenas, F.S. Sherman, 4th Int. Sym, on Rarefied Gas Dynamics, 85, Academic Press, N.Y. (1966).

Au 69 P. Audit, M. Rouault, 6th Int. Conf. on Rarefied Gas Dynamics, Academic Press, N.Y. (1969).

Ax 65 D. Axen, Phd. Thesis, Univ. of British Columbia, 1965, unpublished.

Ba 65 S.D. Baker, G. Ray, G. C. Phillips and G.K. Walters, Phys. Rev. Letters, 15, 115 (1965).

Ba 67 S.D. Baker, D.H. McSherry, D.O. Findley and G.C. Phillips, Bull. Am. Phys. Soc. (N.Y. Meeting, January, 1967).

Ba 68 S.D. Baker, E.B. Carter, D.O. Findley, L.L. Hatfield, G.C. Phillips, N.D. Stockwell, G.K. Walters, Phys. Rev. Letts., 20, 738 (1968).

Be 54 E.W. Becker, K. Bier, Zeit. Fur Naturforschg, 9a, 975 (1954).

Be 56a E.W. Becker, K. Bier, W. Henkes, Zeit. Fur Physik, 146, 333 (1956).

Be 56b E.W. Becker, W. Henkes, Zeit. Fur Physik, 146, 320 (1956).

Be 61 E.W. Becker, R. Klingelhofer, P. Lohse, Z. Naturforschg, 16a, 1259 (1961).

Be 62 E.W. Becker, R. Klingelhofer, P. Lohse, Z. Naturforschg, 17a, 432 (1962).

Bo 51 J. de Boer, E.G. Cohen, Physica 17, 993 (1951).

Br 60 D.A. Bromley and E. Almqvist, Reports on Progress in Physics, Volume XXIII, A.S. Strickland, Ed. (The Physical Society, London, 1960) p. 544. Also D.A. Bromley and E. Almqvist, Chalk River Report, CRP-881, (AECL, Chalk River, Ontario, 1959).

Br. 66 R.F. Brown, J.H. Heald, 5th Int. Sym. on Rarefied Gas Dynamics, Academic Press, N.Y. (1966).

Ca 66 R. Campargue, 4th Int. Symp. on Rarefied Gas Dynamics, 279, Academic Press, N.Y. (1966).

Cl 52 J.R. Clement, E.H. Quinnell, Rev. Sci. Inst. 23, 213 (1952).

Em 58 H.W. Emmons, Fundamentals of Gas Dynamics, Princeton University, Press (1958).

Fe 63 J.B. Fenn, J. Deckers, 3rd Int. Sym. on Rarefied Gas Dynamics, Academic Press, N.Y. (1963).

Fi 67 D.O. Findley, MSc. Thesis, Rice University, 1967 unpublished.

Fi 67 S.S. Fisher, U.C.L.A., Dept. of Engr., Report No. 67-5 (1967).

Fi 69 D.O. Findley, S.D. Baker, E.B. Carter, N.D. Stockwell, Nucl. Inst. and Methods, 71, 125 (1969).

Ga 65 R.L. Gamblin, T.R. Carver, Phys. Rev., 138, 946 (1965).

Gl 67 H.F. Glavish, On the Design of Sextupole Magnets for Polarized Ion Sources, University of Auckland (1967) unpublished report.

Gl 68 H.F. Glavish, Phd. Thesis, University of Auckland (1968) unpublished.

Gl 68 H.F. Glavish, Nucl. Inst. & Methods, 65, 1 (1968).

Go 69 T.R. Govers, R.L. Le Roy, J.M. Deckers, 6th Int. Sym. on Rarefied Gas Dynamics, Academic Press, N.Y. (1969).

Ha 67 O. Hagena, H.S. Morton, 5th Int. Sym. on Rarefied Gas Dynamics, 1369, Academic Press, N.Y. (1967).

Ha 67b O.F. Hagena, J.E. Scott, A.K. Varma, School of Engineering and Applied Science, Univ. of Virginia, Report # AST-4038-103-67u (1967).

Ja 64 D. Jassby, MSc. Thesis, Univ. of British Columbia (1964) unpublished.

Ka 51 A. Kantrowitz, J. Grey, Rev. Sci. Inst., 22, 328, (1951).

Kn 64 E.L. Knuth, U.C.L.A., Dept. of Engr., Report No. 64-53 (1964).

Kn 68 E.L. Knuth, S.S. Fisher, J. Chem. Phys., 48, 1674 (1968).

McM 66 G.E. McMichael, J.B. French, Physics of Fluids, 9, 1419 (1966).

Mi 67 T.A. Milne, F.T. Greene, J. Chem. Phys., 47, 4095 (1967).

Mo 66 M.J. Moravcsik, Proceedings of the 2nd International Symposium on Polarization Phenomena of Nucleons, ed. P. Huber and H. Schopper, Birkhauser, 1966, p. 159.

Ow 52 P.L. Owen, C.K. Thornhill, Aeronautical Research Council Report and Memoranda #2616 (1952).

Ph 59 G.C. Phillips, P.D. Miller, Physical Review, 115, 1268 (1959).

Ph 66 G.C. Phillips, Polarized Targets and Ion Sources, Proceedings of the International Conference on Polarized Targets and Ion Sources, Saclay, France, Dec. 5-9, 1966, p. 215.

Ra 56 N.F. Ramsey, Molecular Beams, Oxford Univ., Press (1956).

Ro 56 T.R. Roberts, S.G. Sydoriak, Phys. Rev. 102, 304 (1956)

Sh 53 A.H. Shapiro, The Dynamics and Thermodynamics of Compressible Fluid Flow, Vol. 1, Ronald Press, New York (1953).

Sh 63 F.S. Sherman, 3rd Int. Sym. on Rarefied Gas Dynamics, Academic Press, N.Y. (1963).

Sm 55 K.F. Smith, Molecular Beams, Methuen and Co. Ltd., London (1955).

Th 69 L.B. Thomas, C.L. Krueger, R.E. Harris, 6th Int. Sym. on Rarefied Gas Dynamics 1015, Academic Press, N.Y. (1969).

Ve 64 C. Vermette, MA.Sc. Thesis, Univ. of British Columbia, (1964) unpublished.

Wa 63 J.B. Warren, W. Klinger, D. Axen, Prog. in Fast Neutron Physics ed. G.C. Phillips, J.B. Marion, J.R. Risser, Rice University Semicentennial Publications, 335 (1963).

We 61 R. Weiss, Rev. Sci. Inst. 32, 397 (1961).

Za 69 R.N. Zapata, R. Ballard, N. Cabrera, 6th Int. Sym. on Rarefied Gas Dynamics, Academic Press, N.Y. 997.